Eindhoven University of Technology
Department of Applied Physics
University Centre in Svalbard
Arctic Geophysics

On solar proton cutoff latitudes measured by GPS satellites

Master thesis

Charlotte Maartje van Hazendonk

Longyearbyen, May 19, 2021

Supervisors University Centre in Svalbard:	dr. E.P. Heino
	dr. N. Partamies
Supervisor Eindhoven University of Technology:	dr.ir. H.C.J. Mulders
Advisers European Space Agency:	dr. P.T.A. Jiggens
	dr. M.G.G.T. Taylor
Committee members:	prof.dr.ir. G.M.W. Kroesen
	dr.ir. S. Nijdam
	dr. M. Duran Matute

Abstract

Solar energetic particle events (SEPE)s are large outbursts of energy from the Sun's surface in which particles are accelerated to relativistic speeds. The solar energetic particles (SEPs) represent one of the main sources of particle radiation in the near-Earth environment. SEPs can have a large impact when entering the Earth's magnetosphere, since they can disrupt radio communication by absorption, increase radiation doses, alter the chemical composition of the atmosphere or lead to spacecraft malfunction.

To better understand the impact of the SEPEs, it is important to know how deep SEPs penetrate into the Earth's atmosphere by determining their cutoff latitude (CL). The behavior of CLs depends on geomagnetic parameters such as the Kp and Dst index and the dynamic pressure of the solar wind.

In this thesis, the access of protons with energies ranging from 18 – 115 MeV is investigated using energetic particle data from the Combined X-ray and Dosimeter (CXD) instrument on board satellites of the Global Positioning System (GPS). The proton data of these CXD instruments has been normalized with proton data from the Energetic Particle Sensor (EPS) on board the Geostationary Operational Environmental Satellites (GOES). For the time period 2001 – 2015, the CLs of energetic protons have been determined. The normalization method has first been validated and a CL-database containing 5976 CLs has been created. A statistical study provides more insights into the driving characteristics of CLs and ultimately results in optimal parameterizations for the different energies based on selected solar wind and geomagnetic parameters. Based on this study, the CL determination method using data from the CXD and EPS particle detectors provides reliable observations of proton CLs with limitations related to the orbits of the satellites and the energy ranges of the instruments. In addition, a comparison between GPS and POES (Polar Orbiting Environmental Satellites) based CL models is presented.

Acknowledgements

The past nine months have been an incredible journey into the world of Space Physics. Now, the time has come to thank everyone who contributed to this thesis and the journey towards it. First and foremost, I would like to thank my daily supervisor, dr. Erkka Heino (UNIS). Thank you for introducing me to the world of cutoff latitudes and guiding me through my thesis with countless explanations, encouragements and advice. Thank you for your patience and the incredible speed with which you read all my drafts.

This thesis would never have been possible without the perseverance of my TU/e supervisor dr.ir. Hjalmar Mulders. You moved Heaven and Earth to enable me to return to Svalbard for my Master thesis during Covid-19 times. To get permission from the TU/e you went as far as to involve the legal department of the TU/e (to ensure they would treat Svalbard as a part of the EEA) and you managed to contact the Dutch Ministry of Foreign Affairs to ensure a Dutch travel advice for Svalbard would be created (which did not exist before). I want to give a special thanks to the Dean of the TU/e Applied Physics department, prof.dr.ir. Gerrit Kroesen, thank you for granting me the final permission to travel. I am honored to have you on my committee. Another reason why I would like to thank Hjalmar is because you managed to find the best advisers for my thesis I could have wished for, dr. Piers Jiggens and dr. Matt Taylor (European Space Agency).

I felt truly privileged to have such knowledgeable advisers. Matt, I do not think the worth "impossible" exists in your vocabulary. If something did not immediately work out, you were always the first one to be supportive, give a pep talk and keep confidence that it would work out (which always miraculously turned out to be true). Your enthusiasm for Space Physics is definitely contagious! Piers, you always managed to have spot on feedback and comments during our monthly meetings. Although you made my life much more difficult at times, exactly those comments took my thesis to a higher level. Thank you for always being able to provide additional background in the world of solar energetic particles. In the rare event that you felt additional expertise was required, you and Matt would immediately set me up with the right person. I was truly honored to be put into contact with dr. Steven K. Morley (Los Alamos National Laboratory) and dr. Janet C. Green (Space Hazards Applications).

Thank you Steve for all the work you have done on the GPS energetic particle data. Without your efforts, I would not have had a topic for this thesis. Your papers (Morley et al. (2016) and Morley et al. (2017)) introduced me to the space weather data revolution called GPS energetic particle data and showed its potential to the entire scientific community. I felt privileged to be put into contact with you to ask all my questions about your specialty. Thank you for looking into my questions and providing me with all the necessary answers. Thank you Janet for immediately responding to my cry for help and scheduling a meeting with me. I am very much looking forward to talk to you and discuss the offset observed with POES data.

I would like to thank dr. Noora Partamies. You took a place more in the background due to my overload of super-/advisers. I am grateful that you stayed on and I really appreciated all your comments and insights. You always took the time for me and made me feel welcome. Furthermore, I would like to thank dr.ir. Sander Nijdam and dr. Matias Duran Matute for their time investment in the evaluation of this thesis.

This research would not have been possible without the data providers. I would like to thank the CXD team at Los Alamos National Laboratory, which designed and built the CXD instruments. I would like to thank NOAA's National Centers for Environmental Information as the authoritative provider for original GOES data and ESA's SEPEM team for removing all spikes and caveats of the original data files. I acknowledge use of NASA/GSFC's Space Physics Data Facility's OMNIweb service and OMNI data for the solar wind and IMF parameters and the Dst index. In addition, I would like to thank the World Data Center for Geomagnetism, Kyoto for providing the Kp index.

I am very grateful to the wonderful guest master students at UNIS with whom I shared all the ups and downs of thesis life. Amandine, Anna, Anton, Astrid, Cecilie, Dani, Lukas, Magnus, Marjolein, Max, Sebastian, Tomi, Vendela and all others that I could not fit in here, it was a pleasure to have you as friends and I will always keep the memories of our amazing hiking/(lunch break) skiing/snowmobile trips. A special thanks to Marjolein, it was a pleasure to share an office with you. You were my most faithful companion (together with your binoculars!) for keeping an eye on everything that happened outside of

our office window such as wildlife (polar bears, seals or belugas), loud snowmobiles, beautiful weather (especially on the other side of Isfjorden) or boats with fellow students. In addition, you always made sure to provide snacks and moral support to keep us going. Keep up the good work for your last month of thesis work, I am sure you will deliver a great thesis!

I especially want to thank my family for all the hours of Skype after letting me leave for Svalbard again to follow my passion. Thank you for all the packages sent over mail and I truly hope I will be able to show you the beauty of Svalbard once the Covid travel restrictions have lifted. Last but not least, I want to thank Peter for his love and support. Thank you for making me countless dinners during the last stages of my thesis, always having a spot for me on your couch and taking me on many cabin trips.

Contents

List of abbreviations

ACE	Advanced Composition's Explorer's
AE	Auroral Electrojet
AU	Astronomical Unit
BER	Bit Error Rate
CXD	Combined X-ray and Dosimeter
CGM	Corrected Geomagnetic Coordinates
CL	Cutoff Latitude
CME	Coronal Mass Ejection
DSCOVR	Deep Space Climate Observatory
Dst	Disturbance storm time
EPP	Energetic Particle Precipitation
EPS	Energetic Particle Sensor
ESA	European Space Agency
ESP	Energetic Storm Particles
FAC	Field-Aligned Current
GCR	Galactic Cosmic Rays
GNSS	Global Navigation Satellite System
GOES	Geostationary Operational Environmental Satellites
GPS	Global Positioning System
GSE	Geocentric Solar Ecliptic
GSM	Geocentric Solar Magnetic
HXP sensor	High-energy X-ray and Particles sensor
IAGA	International Association of Geomagnetism and Aeronomy
ICME	Interplanetary Coronal Mass Ejection
IGRF	International Geomagnetic Reference Field
IMF	Interplanetary Magnetic Field
ISS	International Space Station
LEP	Low-Energy Particle
MEPED	Medium Energy Proton and Electron Detector
MLAT	Magnetic Latitude
MLT	Magnetic Local Time
MLR	Multiple Linear Regression
NASA	National Aeronautics and Space Administration
NOAA	National Oceanic and Atmospheric Administration
PCA	Polar Cap Absorption
POES	Polar Orbiting Environmental Satellites
R_E	Earth radii
RPS	Relativistic Proton Spectrometer
RSGA	Report of Solar Geophysical Activity
SAMPEX	Solar, Anomalous, and Magnetospheric Particle Explorer
SEE	Single Event Effects
SEP	Solar Energetic Particles
SEPE	Solar Energetic Particle Event
SEPEM	Solar Energetic Particle Environment Modelling
SM	Solar Magnetic
SOHO	Solar and Heliospheric Observatory
SSD	Solid State Detector
SSR	Solid State Recorder
UT	Universal Time
UV	Ultra Violet

1 Introduction

Though distant and poorly understood, events such as the solar energetic particle event (SEPE) of Halloween 2003 can have serious impacts on the life of people on Earth. In 2003, this storm gave it the qualification of scariest Halloween in history by NASA (2008). Next to the usual Halloween frights, radio blackouts were caused on Earth, airplanes had to be re-routed and satellites and spacecraft faced malfunction and irreversible damage. On top of that, 50,000 people in Malmö, Sweden, experienced a power outage due to a 10°C temperature rise in transformer oil; the crew of the International Space Station (ISS) had to retreat to a shielded location and the northern lights were visible as far south as Florida (Gopalswamy et al., 2005).

All of this was caused by extreme space weather conditions due to solar activity. In the period from late October to early November 2003, multiple solar flares erupted at the Sun's surface due to several sunspots leading to large coronal mass ejections (CMEs). Thus several SEPEs took place simultaneously. On October 28, one of the largest flares ever recorded was observed followed by a CME with a speed of 2500 km s^{-1}, reaching the Earth within 19 hours and containing a kinetic energy of $4.2 - -6.4 \times 10^{25}$ J (Plunkett, 2005). Subsequently, on October 29, another major flare led to the release of a second powerful CME.

Both events caused radio blackouts on Earth, affecting 59% of reporting spacecraft (Gopalswamy et al., 2005). Additionally, ozone depletion occurred and the electron concentration in the ionosphere increased tenfold (Gopalswamy et al., 2005). Thus the 2003 Halloween events contributed to a serious risk for modern life on Earth.

The occurrence of SEPEs is infrequent, varying from around once a month on average during solar maxima to none during solar minima. During SEPEs bursts of highly energetic particles of solar origin, mostly electrons and protons, are accelerated at or near the Sun's surface and subsequently travel through space guided by the Sun's magnetic field. Additionally, SEPEs can also (partly) consist of energetic storm particles (ESP) which are accelerated closer to Earth at the CME shock passage. The Earth's magnetosphere controls the access of particles into the atmosphere (Störmer, 1955; Smart and Shea, 2001) and (Chu and Qin, 2016). Due to the dipole nature of the Earth's magnetic field, assumed by Störmer (1955), the particles can more easily enter the atmosphere at the poles and move down in latitude afterwards. The cutoff latitude (CL) is the lowest latitude to which a particle of a certain rigidity (momentum per unit charge) can penetrate (Kress et al., 2010) and is determined by the energy of the particle, the geomagnetic conditions, the solar wind and the orientation and angle of incidence of the detector (Heino, 2019; O'Brien et al., 2018). Particles with higher energies have lower CLs. Since the Earth's magnetic field is more complicated than the static dipole field described by Störmer (1955), the CL is constantly varying and changing the near-Earth particle radiation environment and the amount of ionization in the Earth's ionosphere and atmosphere.

Increased radiation levels and increases in ionospheric currents, partly originating from SEPEs, pose a threat to manned spacecraft and airplanes by disrupting high-frequency (HF) and very high-frequency (VHF) communication due to ionospheric absorption, increased radiation doses for humans and possible electronic failure on board when single energetic charged particles interact with materials in a device creating an additional charge inside an instrument, also known as a single event effect (SEE) (Hapgood, 2018). This electronic failure can also upset satellites and other space electronics. Another effect of increased radiation levels in the atmosphere is the enhancement of the production of highly reactive species in the middle atmosphere. These species, odd nitrogen and odd hydrogen, will reduce the ozone concentration (Nesse Tyssøy and Stadsnes, 2015). As ozone is the main absorber of ultra violet (UV) radiation in the middle atmosphere, the radiative balance and the heating and cooling rates of the middle atmosphere are altered (Heino, 2019). Variations in CL influence satellites, aviation and the space weather conditions on Earth and should be studied in more detail.

To gain insight in the behavior of the CLs for varying conditions, two main approaches or a combination of both have been used in literature:

1. calculating the theoretical CLs by tracing particle trajectories using model magnetospheres;
2. determining the CLs experimentally using proton fluxes measured by satellites.

In both cases, the CLs can be compared with the geomagnetic and/or solar wind conditions at the particular times.

Smart and Shea performed multiple studies computing CLs numerically by solving the equation of motion of a charged particle in a magnetic field to calculate charged particle trajectories (Smart et al., 1969; Smart, 1999; Smart et al., 2000; Shea and Smart, 2001; Smart and Shea, 2001, 2003, 2005). CLs in this approach are found to be between the last allowed and first forbidden trajectory of a particle with a certain rigidity. Due to the computationally expensive nature of the particle tracing method, approximations have to be used in these studies (Smart and Shea, 2005). Most of this numerical research by Smart and Shea uses external magnetic field models developed by Tsyganenko (such as the Tsyganenko (1989) (T89) model) combined with the International Geomagnetic Reference Field (IGRF) internal field (Smart, 1999; Smart and Shea, 2001, 2003).

A more recent numerical study investigating the relation between solar wind, geomagnetic conditions and CLs was conducted by Chu and Qin (2016), using the Tsyganenko (1996) (T96) and IGRF internal field models. The behavior of computed CLs is studied for several geomagnetic parameters such as the z component of the interplanetary magnetic field (IMF), B_z, the dynamic pressure of the solar wind, P_{dyn}, the ring current index Dst and the auroral electrojet (AE) index, finding a relation between the CL and B_z, P_{dyn} and the AE index. For the Dst index a correlation was only found during strong magnetic storms (see Section 2.3.2 for more information on magnetic storms).

The experimental cutoff determination and its dependence on geomagnetic conditions have been investigated by Leske et al. (1997, 2001). Using data from the polar-orbitting SAMPEX (Solar, Anomalous, and Magnetospheric Particle Explorer) satellite, the CL has been determined experimentally as the location where the count rate of the proton flux is half of its mean value at geomagnetic latitudes above 70° (Leske et al., 2001). Subsequently the correlation between the variation in CL and geomagnetic activity index, Kp, and the Dst index for several solar energetic particle events between 1992 to 1998 has been studied. Despite finding a clear correlation, the relationship proved worse during critical periods such as the onset of geomagnetic storms. Therefore, the use of only Dst and Kp to predict particle precipitation was found to be insufficient.

The experimental method of Leske et al. (2001) to determine CLs has been applied by Birch et al. (2005), Dmitriev et al. (2010), Nesse Tyssøy et al. (2013) and Neal et al. (2013), among others, using satellites from the Polar Orbiting Environmental Satellites (POES) program equipped with Medium Energy Proton and Electron Detectors (MEPED). Nesse Tyssøy et al. (2013) investigated the effect of different magnetic local time (MLT) sectors and the Dst index on the CL for lower proton energies (focus on 1 – 32 MeV). An asymmetry in CL for day- and nightside especially for lower energies is reported, which is in agreement with previous experimental work by Fanselow and Stone (1972). The correlation between CL and Dst index is comparable to the findings of Leske et al. (2001) for the dayside, but smaller for the nightside. Contrarily, Birch et al. (2005) reported a better correlation between the CL and the Dst index than both studies mentioned above.

Furthermore, some studies have used their experimentally determined CLs to develop new models to calculate CLs such as Nesse Tyssøy and Stadsnes (2015), Dmitriev et al. (2010) and Neal et al. (2013). The model by Nesse Tyssøy and Stadsnes (2015) determines the CLs separately for the dayside (as a function of Dst and B_z) and nightside (as a function of Dst and P_{dyn}). Dmitriev et al. (2010) obtained their model by fitting ellipses to the determined CLs, resulting in a model of CLs dependent on rigidity, MLT, geomagnetic indices Dst, Kp and AE and the dipole tilt angle PS. Neal et al. (2013) studied SEPEs from October 2003 – April 2012 and obtained 16850 CL estimates, which were linked to the Kp and Dst indices, finding high correlation coefficients. This data has been used to empirically fit the Kp and Dst dependence not taking effects from interplanetary coronal mass ejections (ICME) into account. Testing the empirical model gave reasonable results for other SEPEs.

The accuracy of CL models has been investigated experimentally using ground-based measurements from riometers and their cosmic noise absorption. Rodger et al. (2006) and Clilverd et al. (2007) used the Halley riometer in Antarctica to validate the Kp dependent model developed by Smart and Shea (2001, 2003) respectively. It was found that the model shows good agreement for low to moderate geomagnetic activity ($Kp < 5$), but overestimates the CL equatorwards for higher Kp values. More recently, Heino and Partamies (2020) tested the performance of the models developed by Dmitriev et al. (2010) and

Nesse Tyssøy and Stadsnes (2015) with riometer measurements during 73 SEPEs. The models showed comparable performance with slightly better results for the Dmitriev et al. (2010) model.

Other studies compared the numerically and experimentally obtained CLs (e.g. Fanselow and Stone (1972), Smart and Shea (2001) and Birch et al. (2005)), concluding that the numerical CL tend to be further poleward than the measured values especially during magnetically active times. Equally, Neal et al. (2013) reports a systematic offset of solar protons penetrating further equatorward in their empirical study compared to the model of Smart and Shea (2003) when $Kp < 7$. When Kp is above 7, the Smart and Shea (2003) model overestimates the CL equatorwards as reported by Rodger et al. (2006) and Clilverd et al. (2007) as well.

As many of the previous studies determining CLs have focused on a few SEPEs within a limited time range, the goal of this thesis is to perform a statistical study involving many SEPEs over a longer time period. Since 2000 the Los Alamos National Laboratory (LANL) equipped satellites of the Global Positioning System (GPS) with a Combined X-ray Dosimeter (CXD) and the first measurements began in 2001. Nowadays, 24 out of 31 GPS satellites carry a CXD, enabling the measurement of electrons and protons over a wide energy range. In 2016 this data set was made publicly available providing a huge data source for the scientific community (Morley et al., 2017). The proton data of these CXD instruments has been cross-calibrated with the proton data of the Energetic Particle Sensor (EPS) on board the Geostationary Operational Environmental Satellites (GOES) by Carver et al. (2018), concluding that the average CXD fluxes above $>$ 30 MeV are within 20% of the EPS values. As the sensitivity of the CXD decreases below 20 MeV, the agreement with the EPS worsens. Chen et al. (2020) demonstrated that the GPS proton data can be used for quantitative scientific research by comparing the GPS observations to measurements taken by the Relativistic Proton Spectrometer (RPS) on board the Van Allen Probes mission and by determining cutoff L-shells using the GPS data. It should be noted that the CLs were only determined for time periods in which multiple CXD instruments were available simultaneously to make sure that at least one satellite was located in the open field line region during all times for normalization of the proton fluxes. However, the requirement of multiple CXD instruments limits the use of GPS data set severely for the first years after the introduction of the CXD instruments.

In this thesis, GPS CXD proton data $>$ 18 MeV will be used for CL determination in combination with proton data from the GOES satellites for normalization. In this way, a time span of 2001 – 2015 will be covered. The CLs will be linked to their geomagnetic and solar wind conditions of interest, which are the B_x, B_y and B_z components of the IMF, the dynamic pressure of the solar wind, p_{dyn}, and the geomagnetic indices Kp and Dst, to create a database of CLs. Considering that, to my knowledge, GOES proton fluxes have not previously been used to normalize GPS proton data, this novel method will first be validated with results previously published by Carver et al. (2020) and Chen et al. (2020) and quantitatively compared to CLs calculated using their normalization method. Along with paving the way for this new normalization method, this thesis aims to use this CL-database to statistically study the effect of individual geomagnetic parameters on the behavior of CLs and thus identify the driving characteristics of CL variations. As the Earth's magnetosphere is asymmetrical, these driving parameters will be assessed for different MLT sectors to study the day - night and the dawn - dusk asymmetry.

The database of CLs created in this thesis and the insights in behavior of CLs can be applied to future studies into proton precipitation. The amount of proton precipitation at a given point in time and location, such as a radar site, can be determined much more accurately than theoretical CL models could. Additionally, it could be used to distinguish ionization caused by electrons and protons or additional insights in CL behavior could contribute to studies into the causes of CL variation.

In this thesis, Chapter 2 covers the most essential theory, which includes a basic background in space physics related to the Sun, IMF, solar wind, Earth's magnetosphere, magnetic coordinate systems and its geomagnetic indices as well as more specifics on SEPEs, their access in the magnetosphere and the subsequent effects on Earth. The data and processing methods are described in Chapter 3. In addition to the verification of the used method, both normalization and calculation of CLs, Chapter 4 provides the characteristics of the CL variations and their main driving parameters. General trends observed in the GPS based CLs, caveats and the accuracy of the CL-database will be discussed in Chapter 5. In the end, conclusions are drawn in Chapter 6 after which a brief outlook is given in Chapter 7.

2 Background Theory

To describe phenomena dependent on the Earth's magnetic field, basic theory concerning charged particle motion in magnetic fields (Section 2.1) is necessary as well as knowledge about some magnetic coordinate systems (Section 2.2). To understand the behavior of CLs, basic knowledge of the Sun, SEPEs, their propagation through interplanetary space and the subsequent interaction with the Earth's magnetosphere is described in Sections 2.3 and 2.4. Subsequently, the access of energetic particles into the magnetosphere will be discussed in Section 2.5, followed by an explanation of the effects of solar energetic particle precipitation on the Earth in Section 2.6.

2.1 Charged particle motion in a magnetic field

The Earth's intrinsic magnetic field can be modeled as a dipole whose magnetic axis are tilted with approximately 11° compared to the spin axis of the Earth. In the Earth's inner atmosphere, charged particles can undergo three quasi-periodic motions: a gyro-motion around its gyro-center, a bounce motion circling around its magnetic field line between mirror points and a drift motion (Soni et al., 2020). Each of those motions is associated with an adiabatic invariant.

Adiabatic invariants change very slowly compared to typical timescales of particle motion. The first invariant is a function of the magnetic moment, μ, and is associated with the gyro-motion about the magnetic field. The second invariant, the longitudinal invariant, J, is associated with the longitudinal motion along the magnetic field line (bounce motion) and the third invariant, Φ, with the perpendicular drift. In case the motions are periodic and changes in the system have a much smaller angular frequency than the oscillation frequency of the particle, the adiabatic invariant is assumed to be constant (Baumjohann and Treumann, 1996).

The particle motion of solar energetic particles can be understood with the single particle approach. No collisions and no interaction between particles is assumed.

2.1.1 Single particle motion

The Lorentz force, $\vec{F}$ [N], given by

$$\vec{F} = q(\vec{E} + \vec{v} \times \vec{B}), \tag{2.1}$$

in which q [C] is the charge of the particle, $\vec{E}$ [V m^{-1}] the electric field, $\vec{v}$ [m s^{-1}] the velocity of the particle and $\vec{B}$ [T] the magnetic field, describes the effect of electric and magnetic forces on a charged particle. The particle's motion can be found when inserting the Lorentz force into Newton's second law, resulting in

$$m\frac{d\vec{v}}{dt} = q(\vec{E} + \vec{v} \times \vec{B}), \tag{2.2}$$

where m [kg] is the mass of the particle.

When the assumption of no electric field and a homogeneous magnetic field are made, equation 2.2 describes a gyrating motion of a particle along the same magnetic field line with gyrofrequency Ω_c and Larmor radius (or gyro radius) r_c.

$$\Omega_c = \frac{|q|B}{m} \tag{2.3}$$

$$r_c = \frac{mv_\perp}{qB} \tag{2.4}$$

where $v_\perp = \sqrt{v_x^2 + v_y^2}$ represents the constant speed perpendicular to $\vec{B}$. Due to the difference in mass, the Larmor radius for a proton is much larger than for an electron. Additionally, the gyro-radius of protons and ions increases with energy and L-shell (Soni et al., 2020).

The introduction of an electric field results in the acceleration and deceleration of the particle, increasing and decreasing the Larmor radius and thus creating drift. The drift of the guiding center is called the $\vec{E} \times \vec{B}$ drift given by

$$\vec{v}_E = \frac{\vec{E} \times \vec{B}}{B^2}, \tag{2.5}$$

where $\vec{v}_E$ is the velocity as a result of the electric field. Since the sign of the $\vec{E} \times \vec{B}$ drift is independent of the charge, the ions and electrons will gyrate in the same direction. Drift can also have other causes than an electric field such as a gradient in magnetic field. The general form of drift is given by

$$\vec{v}_F = \frac{\vec{F} \times \vec{B}}{qB^2}, \tag{2.6}$$

where $\vec{F}$ represents any force acting on a charged particle in a magnetic field. Equation 2.6 shows that the sign of all sources of drift except the Coulomb drift in Equation 2.5 depend on the sign of the charge of the particle. Hence, these drifts create electron and proton currents in opposite directions inducing a current (Baumjohann and Treumann, 1996).

The bounce motion of a particle takes place between two mirror points. The location of the mirror points depends on the pitch angle α of the charged particle. This is the angle between the velocity of the particle and the local magnetic field. When the pitch angle reaches $\alpha = 90°$, the particle is reflected. This location is defined as its mirror point.

A schematic representation of the three types of motion inside of the inner Earth's magnetosphere are shown in Figure 2.1.

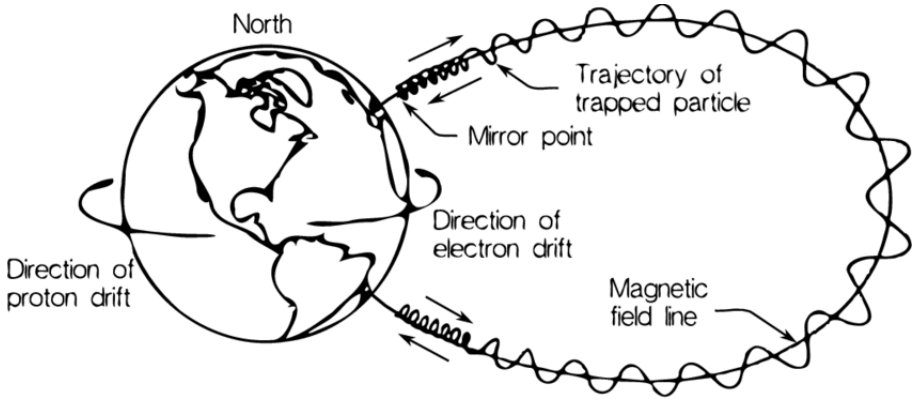

Figure 2.1: Schematic representation of the three motions of charged particles in a dipole field. The gyro-motion around the magnetic field line is shown as well as the bouncing at the mirror points. Additionally, the ions drift westward while the electrons drift eastward due to the gradient and curvature drift. Image retrieved from (Constantinescu, 2007).

2.2 Magnetic coordinate systems

In the near-Earth space environment, processes are strongly affected by the Earth's magnetic field and its disturbances. As the geographic poles of the Earth are displaced compared to the geomagnetic poles, magnetic coordinate systems are often favored over geographic coordinate systems when describing geomagnetic processes around the Earth. There are multiple magnetic coordinate systems based on the spherical harmonic expansion coefficients of the IGRF, such as the corrected geomagnetic coordinates (CGM) for which field lines of a higher order IGRF model are traced to a simple tilted dipole model. The IGRF will be discussed in more detail in Section 2.2.2. Some coordinate systems are based on the position of the Sun as well as having an Earth-Sun line along one of the coordinate axes, such as the geocentric solar ecliptic (GSE) and the geocentric solar magnetic (GSM) coordinate systems. At large distances from the Earth, the Earth-Sun line is convenient due to the radially out-flowing character of the solar wind, making it easier to describe the solar wind - magnetosphere interactions. Closer to the Earth, the Earth's magnetic field becomes the dominant force, making it more convenient to have a coordinate system that is aligned with the dipole axis of this field, such as the solar magnetic (SM) coordinate system (Laundal and Richmond, 2017).

For this thesis, a combination of the IGRF internal model and the Tsyganencho 1989 (T89) external field model (see Subsection 2.2.3 for more information) are used to calculate the different L-shell values of

the GPS satellite measurements. The L-shell value has been defined by the B, L coordinate system of McIlwain (McIlwain, 1961).

2.2.1 *B, L* coordinate system

The B, L coordinate system is defined by McIlwain (1961, 1966) and is much used when studying trapped particles inside the inner magnetosphere (Laundal and Richmond, 2017). B represents the magnetic field strength. L corresponds to the radial distance, in Earth radii (R_E), of a field line in the equatorial plane from the Earth. For a dipole field, this is shown in Figure 2.2. In the B, L coordinate system, L is calculated with a realistic field model instead of the dipole model, depending on B and the longitudinal adiabatic invariant, J. As J is an integral invariant, it stays constant under gradual change of the systems parameters, ensuring that a particle moving around Earth in the magnetosphere will return to the same line of force or L-shell.

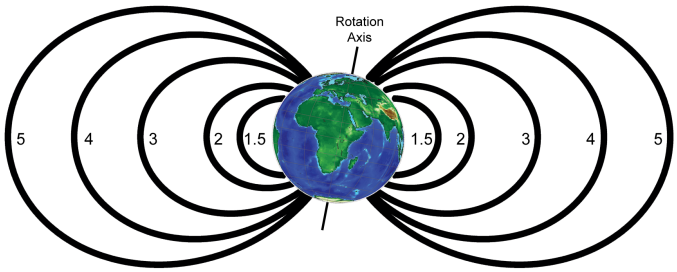

Figure 2.2: Schematic representation of the different L-shell values. Image retrieved from (Golden, 2007).

It is possible to convert the L-shell parameter into invariant latitude, Λ, by using the definition of O'Brien et al. (1962),

$$\Lambda = \cos^{-1}\left(\sqrt{\frac{1}{L}}\right) \tag{2.7}$$

where L is the L-shell value and which is valid for $L \geq 1$. The invariant latitude describes where a magnetic field line touches the Earth's surface.

When the L value is mentioned in this thesis, it will refer to the measured location of the particle, which is the spacecraft location L_{sc}, and not the gyrocenter location of the particle, L_{gc}.

2.2.2 International Geomagnetic Reference Field

The International Geomagnetic Reference Field (IGRF) is a mathematical model of the Earth's main magnetic field on and above the Earth's surface, in which only internal sources of magnetism are taken into account. The model uses a 13^{th} order spherical harmonics function to describe the field on a large scale. The first version was developed in 1965 by the International Association of Geomagnetism and Aeronomy (IAGA) and subsequently the coefficients of the model have been updated every five years to correct for fluctions in the outer core of the Earth's magnetic field. The current IGRF model, IGRF-13 was released in December 2019 by IAGA and will predict the secular variations between 2020 – 2025 (Alken, 2019).

2.2.3 Tsyganenko 1989 model

The Tsyganenko 1989 (T89) model (Tsyganenko, 1989) is an empirical approximation of the Earth's magnetosphere based on several levels of disturbance as given by the magnetic index Kp. Contrary to the IGRF model, T89 is an external field model, taking into account external sources for variations in the Earth's magnetic field. For this model, major magnetospheric current systems such as the ring current, the magnetotail current system and the Chapman-Ferraro currents have been included. However, the Birkeland current systems, the partial ring current and the interplanetary magnetic field penetration are not incorporated in the model. Please note that these current systems will be explained in more detail in Subsection 2.4.1.

Zhang et al. (2010) compared the T89 model among others with eight years of magnetic field data and found that the model underestimates the ring current. Furthermore, it works better during weaker geomagnetic activity.

2.2.4 Polar plots

A convenient way of visualizing effects happening at either poles of the Earth which are influenced by both the Earth's magnetic field and the Sun, is a coordinate system consisting of a top-down view of the Earth, a polar plot. The geomagnetic pole is located in the center, with magnetic latitude (MLAT) or invariant latitude, Λ, going radially outwards. On the surface of the Earth MLAT and Λ are equal. Both are analogous to latitude, but with respect to the geomagnetic poles instead of the geographic poles. To fix the coordinate system with respect to the Sun, MLT is used. The principle idea of MLT is that the Earth, centered at the magnetic poles, is divided into 24-hour bins, where 1-hour represents 15° of magnetic longitude. Another slightly different definition by Baker and Wing (1989) is

$$\text{MLT} = \text{UT} + \frac{\phi + \phi_N}{15}, \tag{2.8}$$

where UT is the universal time given in hours, ϕ the magnetic longitude and ϕ_N the geographic longitude of the North centered dipole pole.

A schematic representation of the MLT/MLAT coordinate system is shown in Figure 2.3. The Sun is always located at the same position compared to the MLT hours, at noon. It rises at the dawn side and sets at dusk. The magnetotail of the Earth's magnetic field is therefore always located at midnight. Thus an observer located at a fixed position on Earth (MLAT) will rotate through all MLT hours during a day.

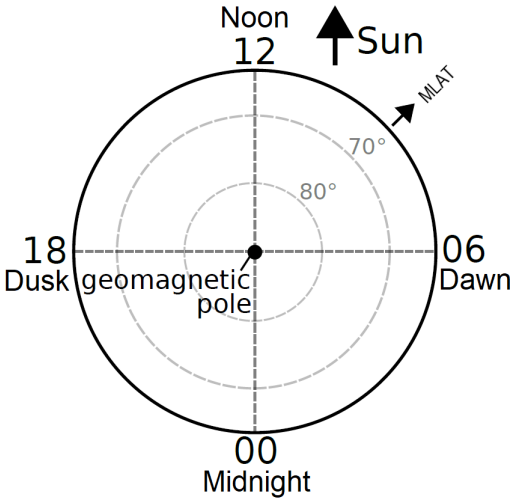

Figure 2.3: Schematic representation of the MLT/MLAT coordinate system. Figure adapted from Herlingshaw (2020).

2.3 The Sun

Although the Sun is an ordinary star, its distance to the Earth enables life on Earth and makes it the most accessible star to study. It is a magnetically driven "ball" of very hot plasma held together by gravity. Its mass is around 2×10^{30} kg, consisting mainly of hydrogen (92%), helium (7.8%) and different metals (0.2%). Although it is not possible to see magnetic field lines, they constantly interact with one another, causing massive eruptions on the Sun, which release plasma into interplanetary space. As the mean distance from Sun to Earth is around 1.5×10^{11} m or 1 astronomical unit (AU), a part of the particles radiated by the Sun will reach the Earth. The first sign of an eruption on the Sun arrives via sunlight, because it takes photons only 8 minutes to reach the Earth. Charged particles take minutes to hours longer (Kivelson and Russell, 1995).

The temperature of the Sun's surface is around 5700 K. However, darker spots at the Sun's surface, sunspots, are somewhat cooler. They appear darker, because the magnetic field of the Sun is concentrated in these areas. The tension of the magnetic field lines suppresses the convective flow, thus inhibiting heat transfer from within the Sun to its surface, leading to cooler temperatures than the surrounding photosphere (Choudhuri, 2011). Since the Sun radiates like a black body, cooler areas result in less radiation, appearing as darker spots.

Sunspots can be as large as 10 times the size of the Earth. Between 1825 and 1850, Heinrich Schwabe conducted a large number of sunspot measurements and found out that the variation in the number of sunspots is periodic. Furthermore, Edward Sabine discovered in 1851 that the variation in sunspot occurrence was correlated with the intensity of geomagnetic disturbances on Earth. Additionally, on the 1st of September 1859, Richard Carrington saw a flare erupting from the Sun's surface while sketching a group of sunspots. The next day, The Kew Observatory (London) measured disturbances in the Earth's magnetic field. Today we know that the eruption from the Sun's surface and the following coronal mass ejection (CME) enhanced electric currents in the Earth's ionosphere, resulting in magnetic disturbance on Earth. As sunspots are the center of active regions on the Sun, they play an important role in the amount of radiation released by the Sun (Kivelson and Russell, 1995).

Nowadays we know that one solar cycle lasts an average of approximately 10-11 years (or twice that period if the configuration of the magnetic field is taken into account) and is caused by the entanglement of the Sun's magnetic field. The dynamical solar magnetic field originates from the dynamo effect, featuring an oscillation between the toroidal (azimuthal) and poloidal (meridional) components of the Sun's magnetic field (Choudhuri, 2011; Sanchez et al., 2014). First the Ω-effect takes place in which an initial poloidal field generates toroidal fields due to differential rotation of the Sun. Subsequently, the toroidal field lines lead to a new poloidal field with different polarity than the initial field. One process that could lead to this new poloidal field is the α-effect during which cyclonic turbulence of the toroidal fields associated with the Coriolis force produce small scale secondary poloidal fields. Together, the small scale fields result in one large-scale poloidal field. Another option is the Babcock-Leighton mechanism, which involves the buoyancy of toroidal flux tubes (Sanchez et al., 2014). A schematic representation of the magnetic processes throughout a solar cycle is shown in Figure 2.4 where the Ω-effect is depicted in sub-figures (a) – (c), the α-effect in sub-figures (d) – (f) and the Babcock-Leighton mechanism in (h) – (j).

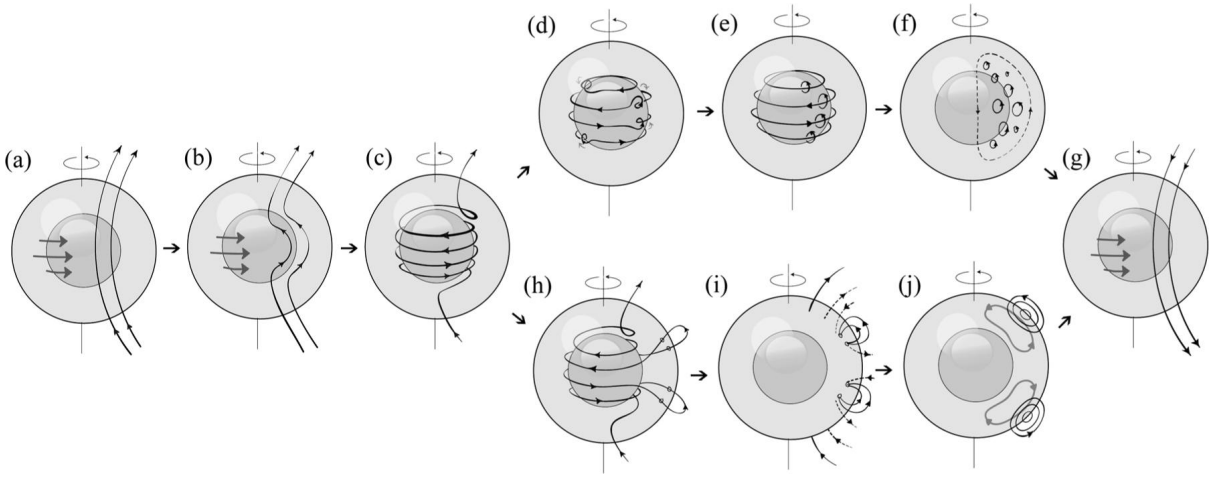

Figure 2.4: (a), (b) and (c) represent the Ω-effect in which the large-scale poloidal field of the Sun forms toroidal fields due to the differential rotation of the Sun. The α-effect is depicted in subfigures (d), (e) and (f), where turbulence of the toroidal field lines leads to small scale poloidal field, which can be added up to the large-scale poloidal field with different orientation in (g). (h), (i) and (j) show the buoyant loops arising from the toroidal field lines in the convective zone of the Sun resulting in sunspots and after reconnection in a new poloidal field in (g). Figure retrieved from Sanchez et al. (2014)

.

Babcock (1961) and Leighton (1969) proposed that sunspots arise when the toroidal field forms buoyant loops within the convection zone that rise to the surface and twist producing two sunspots with different

polarity as can be seen in Figure 2.4 (h) and (i). Thus the number of sunspots is maximum when the toroidal field is strongest and the poloidal field is near its minimum (when the magnetic poles of the Sun are about to flip). In Figure 2.5 the mean number of sunspots per month for the last two solar cycles are shown.

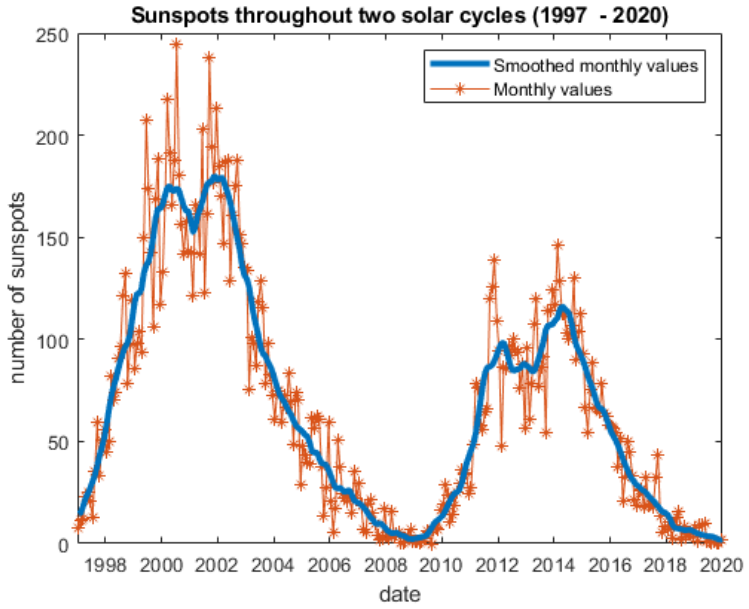

Figure 2.5: The number of sunspots on average per month from 1997 – 2020, showing two solar cycles (solar cycle 23 and 24). The data has been retrieved from SILSO World Data Center (2020).

2.3.1 Solar wind and interplanetary magnetic field

A continuous stream of charged particles, mostly consisting of electrons and protons, is ejected from the Sun due to the pressure difference between the Sun and interplanetary space. This stream of plasma is also known as the solar wind and originates when the plasma in the Sun expands from the outermost atmosphere of the Sun, the corona. Following the magnetic field lines of the Sun the plasma forms coronal loops until the Sun's gravity cannot hold it down anymore and the plasma travels radially outwards from the Sun with a speed of around 200 – 800 km s^{-1}. Since this speed is higher than the local speed of sound, the solar wind is supersonic. When traveling through interplanetary space, the pressure in the solar wind mostly consists of the dynamic pressure $P_{dyn} = \rho u^2$, in which ρ represents mass density and u solar wind velocity.

The escaping plasma has a very high conductivity, thus the Sun's magnetic field lines will remain "frozen-into" the solar wind plasma as discovered by Alfvén (1942). Therefore, the solar wind carries a magnetic field, the interplanetary magnetic field (IMF), with it while it moves through space. The orientation and strength of the IMF as well as the dynamic pressure of the solar wind determine the coupling between the solar wind and the Earth's magnetosphere (Adebesin et al., 2013).

The IMF was first measured by the Pioneer V probe in 1960 and found to be nearly constant in magnitude and nearly uniform in direction during undisturbed times (Coleman et al., 1960). Since 1996, near continuous in-situ measurements of the solar wind and IMF are performed at the first Lagrangian point, L_1, by spacecraft such as WIND, Advanced Composition's Explorer's (ACE) and Deep Space Climate Observatory (DSCOVR) (Ogilvie and Desch, 1997; Stone et al., 1998; Burt and Smith, 2012). L_1, located at a distance of 1.5 million km or 0.01 AU from the Earth, is the position at which the orbital period of any object becomes equal to the Earth's orbital period. Measured parameters at the L_1 position of the solar wind and IMF include plasma density, ρ [N cm^{-3}], He/H ratio, temperature, T [K], velocity, v [km s^{-1}], velocity components, v_x, v_y and v_z, magnetic field, B [nT], and magnetic field components, B_x, B_y and B_z.

2.3.2 Solar Energetic Particle Events

Together with the continuous plasma flow of the solar wind, there are also more energetic events taking place at the Sun in which particles are accelerated to relativistic speeds and become solar energetic particles (SEPs). When these events are Earth-directed, geostationary satellites such as those from the GOES mission monitor the enhanced proton fluxes. According to the definition of NOAA Space Environment Services Center, an event is categorized as a solar energetic particle event (SEPE), also known as a solar proton event, when the interplanetary > 10 MeV integral flux exceeds 10 pfu (particle flux unit = 1 $cm^{-2}s^{-1}sr^{-1}$) for at least three consecutive data points (15 minutes). Since 1976, detectors on board different GOES satellites have been used to measure the > 10 MeV integral fluxes (Oh et al., 2010).

In Figure 2.6 the radial movement of SEPs after a SEPE from the Sun is shown. As the Sun rotates, the SEPs are guided by the magnetic field lines of the Sun and spiraling into interplanetary space. During a SEPE, ions (of which > 90 % protons), electrons and light are released.

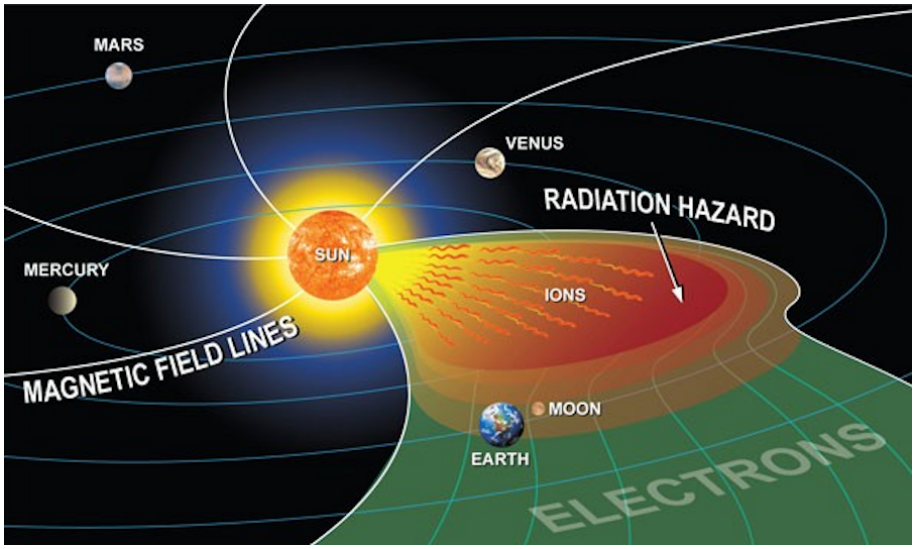

Figure 2.6: The propagation of SEPs from the Sun. Electrons propagate fastest after which the protons and heavier ions approach the Earth and pose radiation hazards. Image retrieved from Boubrahimi et al. (2017).

SEPEs are formed by two different acceleration mechanisms. "Impulsive" events are formed when a flare occurs at the Sun's surface and resonant stochastic acceleration related to the turbulence of plasma and the reconnection of open field lines takes place (Petrosian, 1998). They last less than one day, have relatively small peak fluxes (integrated fluxes) and a high electron to proton intensity ratio (Kouloumvakos et al., 2015). More "gradual" events are caused by acceleration in shock waves formed by CMEs (Reames, 2013). Compared to impulsive events, gradual events last longer (time scale of days) and have higher peak fluxes. Both mechanisms are not exclusive and can therefore take place simultaneously. For energies below 100 MeV the biggest events are dominated by CME-driven shock acceleration. In Figure 2.7 typical proton intensity profiles for both an impulsive (left) and a gradual (right) SEPE are shown.

A solar flare is a local, short-lived event inside a sunspot group lasting for anywhere between a few seconds to an hour. It is characterized by a sudden brightening of electromagnetic emission from the entire spectrum, specifically characterized by the H Ly_α emission line accompanied by an increase in X-ray emissions. Flares are classified as A (weakest), B, C, M and X (strongest) according to their X-ray (1 – 8 Å) peak flux [W m^{-1}]. The power released during a typical solar flare eruption is 10^{20} W, while major flares release up to 10^{25} W, making them the most powerful phenomena close to the Earth (NASA, 2021). As a result, increased ionization in the Earth's ionosphere causes absorption of radio waves leading to possible large-scale radio blackouts.

CMEs are giant clouds of plasma from the Sun's corona ejected into space. During solar maximum the Solar and Heliospheric Observatory (SOHO), located around L_1, detects ~ 1400 CMEs $year^{-1}$ (Giordano

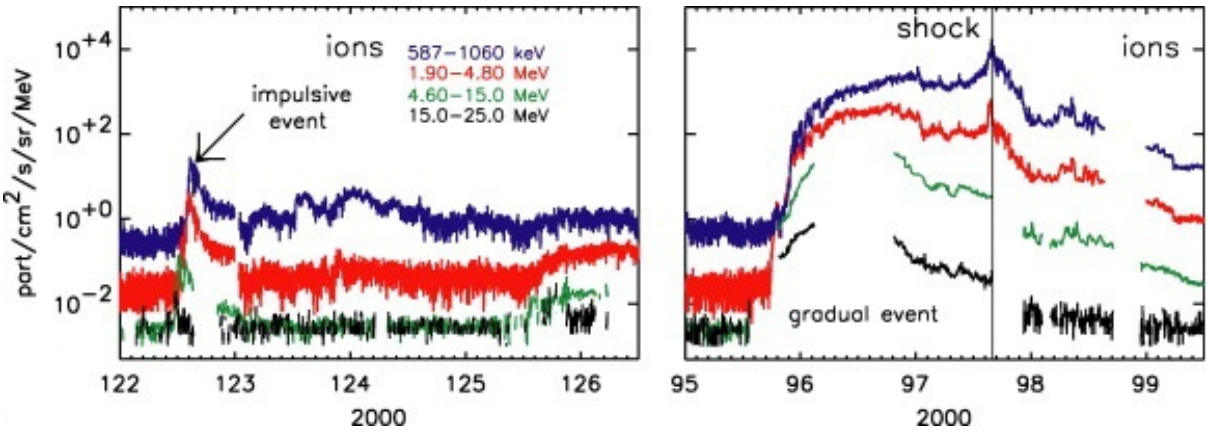

Figure 2.7: Intensity-time profiles of an impulsive (left) and gradual (right) SEPE*. The proton fluxes with different energies are plotted versus the day of the year 2000. Figure adapted from Lario (2005).*

et al., 2013). There is a huge variety in CMEs with speeds ranging from 200 km s^{-1} (usually slower than the solar wind) to > 2500 km s^{-1}. Thus it takes a CME approximately 18 hours to 3 days to reach the Earth. When a CME is detected near Earth, it is known as an interplanetary CME (ICME). The high density of plasma and strong magnetic field carried by a CME, severely change the Earth's magnetosphere. In case of an average CME, the magnetic field close to the Earth remains relatively unaltered and protects the Earth from SEPs. However, in case of a strong CME, the front of the magnetopause is pushed much closer to Earth. During the 21 January 2005 magnetic storm, the magnetopause was located at $L < 5R_E$ as reported by Dmitriev et al. (2014) and thus the magnetosphere at $L > 5R_E$ was eliminated, leaving latitudes above around 60° exposed to the SEPs. In Section 2.4, the Earth's magnetosphere and its magnetopause will be explained in more detail.

Gradual SEPEs are often accompanied by magnetospheric storms, which are an indicator of geomagnetic activity on Earth. They are caused by large-scale solar wind structures such as CMEs and are characterized by the disturbance storm time (Dst) index. The Dst index will be discussed in more detail in Subsection 2.4.2. During a magnetic storm, energy ($\sim 10^{13}$ W for a moderate storm) is transferred from the solar wind into the Earth's magnetosphere mainly by magnetic reconnection, which will be discussed in Section 2.5. A geomagnetic storm is characterized by its main phase and consists of three phases in total; the initial phase, main phase and recovery phase. During the initial phase, the Dst index is slightly positive, after which it decreases abruptly (such as $\frac{dDst}{dt} < -2$ nTh^{-1} (Partamies et al., 2013)) during the main phase. In this period, the horizontal component of the Earth's low latitude magnetic field is significantly compressed. This recovers during the recovery phase which may last for several days (Partamies et al., 2013; Lakhina et al., 2006). It should be noted that during these geomagnetic storms, energetic storm particles (ESP) can be accelerated in the shock region close to Earth. These particles behave differently than SEPs and are mostly pronounced for the lower energies ($E < 10$ MeV). The strength of geomagnetic storms can be classified by the minimum Dst index. Distinction between weak (≤ -30 nT), moderate (≤ -50 nT), strong (≤ -100 nT), severe (≤ -200 nT) and great (≤ -350 nT) storms is made (Loewe and Prölss, 1997).

2.4 Earth's magnetosphere

The supersonic solar wind is slowed down when it approaches Earth and encounters the Earth's magnetic field. The transition from supersonic to subsonic speeds results in compression and heating of the solar wind plasma and leads to a shock formation on the dayside of the Earth, called the Bow shock (at $\sim 14R_E$). Between the Bow shock and the Earth's magnetopause, a turbulent region called the magnetosheath is formed. Closer to the Earth, the magnetopause marks the boundary between the IMF controlled space plasma and the magnetosphere. The Earth's magnetic field behaves like an obstacle to the solar wind, because the frozen-in IMF and the Earth's magnetosphere cannot mix. So the solar wind gets deflected around the magnetopause, which consists of a current sheet. The location of the magnetopause is determined by the pressure balance between the dynamic solar wind pressure, P_{dyn}, and the pressure

inside the magnetopause $p_B = \frac{B^2}{2\mu_0}$, where B is the magnetic field strength and μ_0 the permeability of free space. Due to the constant kinetic pressure of the solar wind, the magnetosphere is compressed on the dayside to a distance of around 10 R_E and extended on the nightside in the magnetotail as far as 1000 R_E being shown in red in Figure 2.8. In case of strong SEPEs, the magnetopause is compressed further on the dayside. Open field lines are only connected to the Earth on one side and to the IMF on the other side, while closed field lines form a loop around the Earth (Ganushkina et al., 2018).

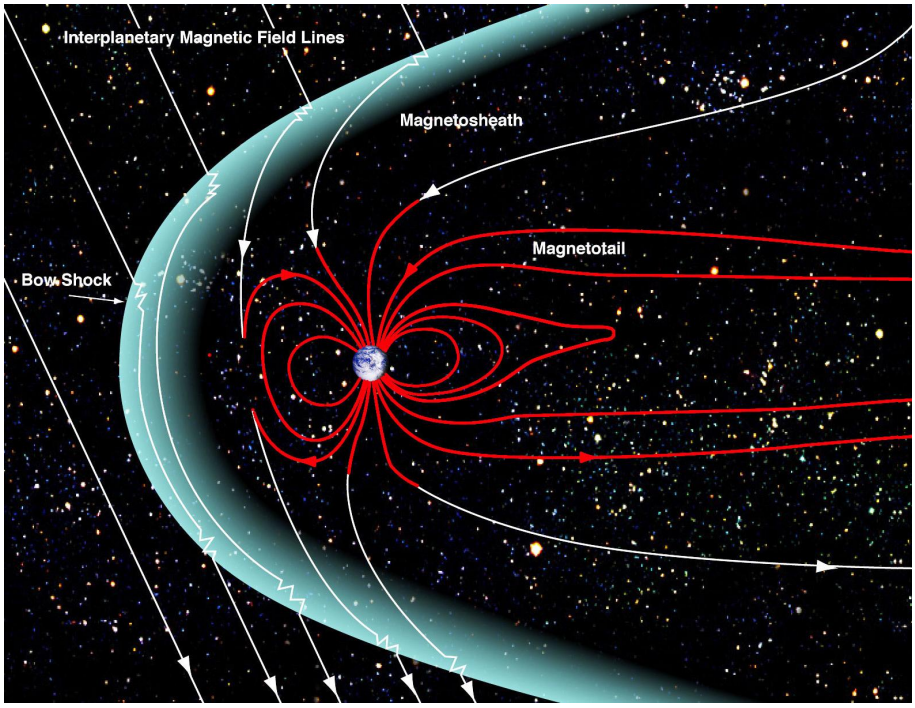

Figure 2.8: The Earth's magnetosphere with the Sun located on the left side. Figure retrieved from NASA et al. (2017).

Highly energetic cosmic particles arriving at the magnetosphere are deflected by the Lorentz force (equation 2.1). Since the Earth's magnetic field can be approximated as a dipole, the Lorentz force is stronger at the equator where the angle between the incident particles and the magnetic field can approach a maximum of 90°. As the field lines at both poles are almost vertical, the $\vec{v} \times \vec{B}$ term goes to zero and the deflection gets weak. Therefore, a small fraction of the highly energetic particles can enter the Earth's magnetic field at either poles (Kivelson and Russell, 1995).

2.4.1 Currents in the magnetosphere

Electric currents and current densities, $\vec{J}$ [A m^{-2}], are associated with magnetic fields, $\vec{B}$ [T], as described by Ampere's law:

$$\nabla \times \vec{B} = \mu_o \left(\vec{J} + \epsilon_0 \frac{\partial \vec{E}}{\partial t} \right), \tag{2.9}$$

where $\mu_0 = 4\pi \times 10^{-7}$ Hm^{-1} is the permeability of free space, ϵ_0 [F m^{-1}] the permittivity of free space and $\vec{E}$ [V m^{-1}] the electric field. Thus the Earth's magnetosphere has corresponding currents as source. The origin of the internally generated dipolar magnetic field is found within intrinsic currents flowing within the Earth. However, to determine the complete topology of the Earth's magnetosphere, other current systems within the Earth's magnetosphere should be considered as well. When the geomagnetic conditions around Earth change, both currents and magnetosphere will be influenced.

In Figure 2.9 a schematic representation of the major current types in the equatorial plane of the Earth is shown. The boundary currents flowing on the magnetopause are called the *Chapman-Ferraro* currents. Their origin can be understood examining the trajectories of charged particles in a magnetic

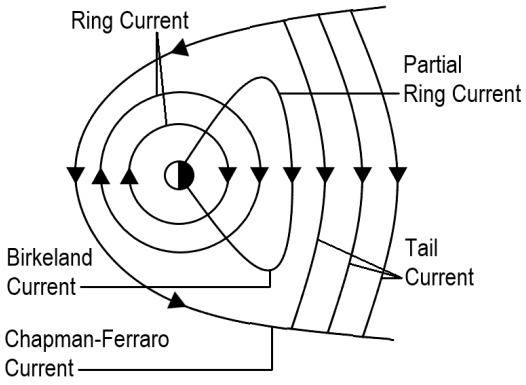

Figure 2.9: The equatorial plane with major currents flowing in the Earth's magnetosphere. Figure adapted from Kivelson and Russell (1995).

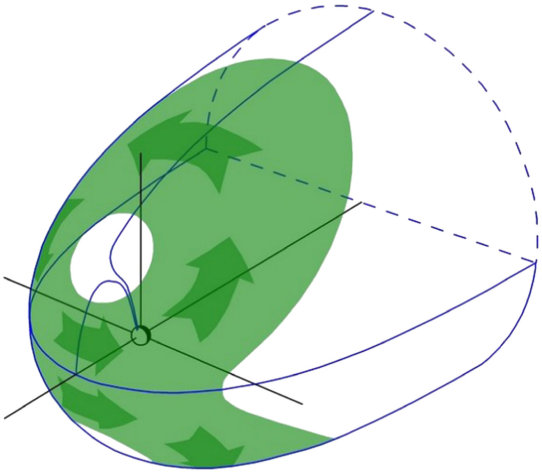

Figure 2.10: The Chapman-Ferraro currents on the dayside of the magnetopause. Figure retrieved from Ganushkina et al. (2018).

field. Electrons and protons gyrate in opposite direction. When a particle encounters a stronger magnetic field, it will be forced to return to its previous magnetic field, the magnetosheath in this case, after half a gyration. Due to the opposite gyration and thus opposite movement of electrons and protons, this will result in a net current flow (Ganushkina et al., 2018). As the Earth's magnetic field is predominantly northward oriented, the Chapman-Ferraro currents will flow from dawn to dusk in the equatorial plane. The currents form closed loops over the dayside of the magnetopause as can be seen in Figure 2.10. The current density in the magnetopause is about 10^{-6} Am^{-2} resulting in a total current in the magnetopause in the order of 10^7 A (Baumjohann and Treumann, 1996).

The *tail current* consists of a thin sheet of currents flowing in the area where the magnetic field changes direction. It acts as a division between two regions with almost uniform opposite directed magnetic fields in the tail. The field above the tail current sheet is earthward directed, while the one below is anti-earthward oriented, resulting in a southwards magnetic field at the location of the Earth. Due to the geometry of the highly stretched tail, the current flows in westward direction. After reaching the magnetopause, the current should form a closed loop. The tail current thus closes via the magnetopause above and below the magnetic field regions of the tail, forming an Θ shape, with so called *return current* (Ganushkina et al., 2018). Both the tail and return currents are shown in Figure 2.11.

The *ring current* flows in the equatorial plane around the Earth in both east- and westward direction as can be seen in Figure 2.12. An important origin is the injection of plasma from the magnetotail during for example geomagnetic storms. The injected protons will drift to the west, while electrons drift to the east, resulting in a net current around the Earth called the ring current. The current in westward direction (blue) will generate a magnetic field opposite to the Earth's magnetic field and thus reduce the measured field on Earth. Because of the direct link with geomagnetic storms, the ring current plays an important role in measurements of magnetic disturbances. Current densities in the eastward (brown) ring are in the order of 2 nAm^{-2}, while the westward (blue) current density fluctuates between 1–4 nAm^{-2} during quiet times and 7 nAm^{-2} during storms. However, it can also increase to 50 nAm^{-2} during geomagnetic storms, thus heavily affecting the Earth's magnetic field. It should be noted that although the ring current looks symmetrical, it is almost always asymmetrical in current density (Ganushkina et al., 2018; Lakhina et al., 2006).

Additionally, it has been suggested that the ring current splits into two branches on the dayside as depicted in yellow in Figure 2.12 (Ganushkina et al., 2018).

Next to the currents in the equatorial plane, there are also field-aligned currents (FACs), flowing parallel to the magnetic field. These FACs are also called *Birkeland currents*. They are divided into region 1 and region 2 FACs. Region 1 FACs are in the poleward half of the auroral oval, while region 2 currents are in the equatorward half. The region 1 FACs and possible closure paths are shown in Figure 2.13. It can be

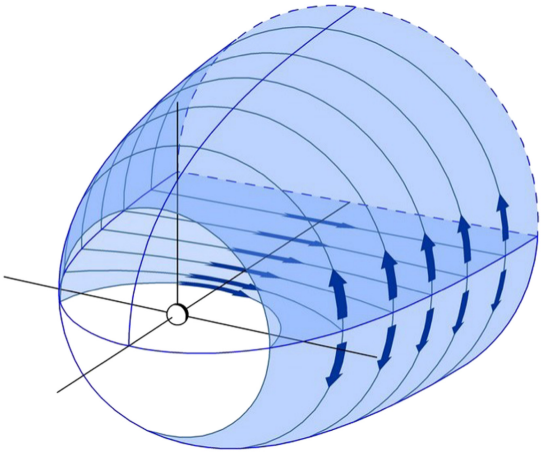

Figure 2.11: The tail current in the (near) equatorial plane. The oppositely directed return currents on both the top and bottom side of the magnetopause provide closure. Figure retrieved from Ganushkina et al. (2018).

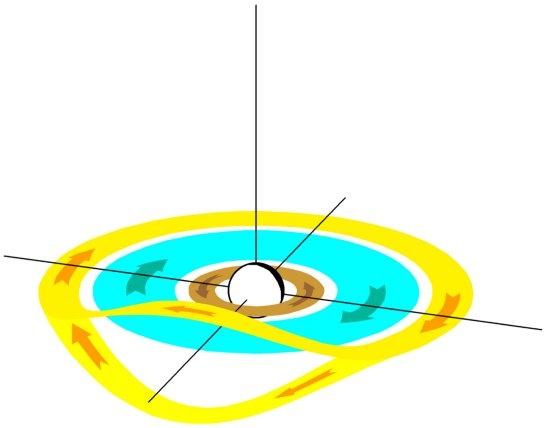

Figure 2.12: The eastward (brown), westward (blue) and cut ring currents (yellow) on the dayside. Figure retrieved from Ganushkina et al. (2018).

seen that the region 1 FACs are connected to the plasma sheet, boundary layer and the magnetopause on the nightside, while they are in the open field line region and connected to the dayside magnetopause on the dayside (Ganushkina et al., 2018).

Region 2 FACs connect the partial ring current to the ionosphere as shown in Figure 2.14. The *partial ring current* is part of the westward ring current and can dominate this current during magnetic storms (Ganushkina et al., 2018). It is formed because more plasma is injected into the inner magnetosphere from the nightside plasma sheet during magnetic disturbed times. This leads to a highly asymmetrical plasma pressure in the inner magnetosphere, creating a gradient in azimuthal direction. The ring current should be closed outside of the inner magnetosphere and thus flow along a field line. Thus the region 2 FACs are created, flowing equatorward compared to the region 1 currents. They are directed inwards into the ionosphere around dusk and outwards at dawn (Ganushkina et al., 2018). Region 2 FACs tend to be smaller than region 1 FACs.

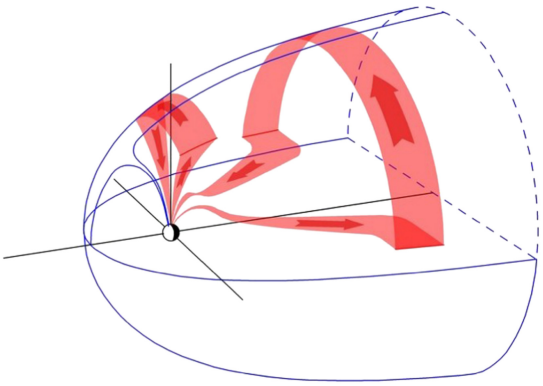

Figure 2.13: Birkeland or region 1 FACs with possible closure paths. Figure retrieved from Ganushkina et al. (2018).

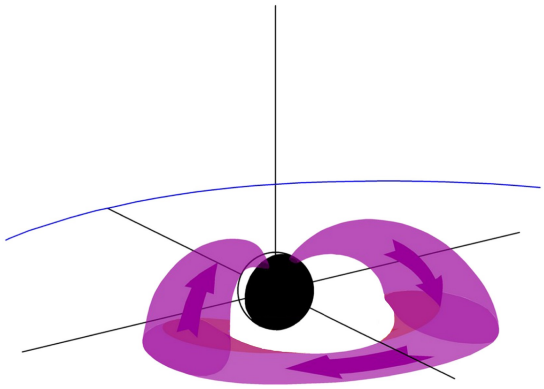

Figure 2.14: The partial ring current and the region 2 FACs. Figure adapted from Ganushkina et al. (2018).

2.4.2 Magnetic indices

The access of energetic protons in the atmosphere and thus their CL depend on many parameters such as the activity level of the Sun and the level of disturbance of the Earth's magnetic field. Magnetic activity

on the Earth's surface is caused by electric currents in the ionosphere and magnetosphere. Starting from the 1830s when Carl Friedrich Gauss invented the magnetometer (Kivelson and Russell, 1995), the disturbances in the Earth's magnetic field have been measured by a network of magnetometers all around the globe (Gjerloev, 2009). Based on these measurement, several geomagnetic indices have been introduced to simplify the task of interpreting geomagnetic conditions. These geomagnetic indices provide a measure of the geomagnetic activity on the Earth and could therefore provide useful information about CLs or play a role in predicting CLs based on their correlation with CLs as mentioned in Chapter 1.

Important indices are the geomagnetic activity (K or Kp) index and the disturbance storm time (Dst) index among others.

K and Kp indices

The K index, introduced in 1939 by Bartels et al. (1939), categorizes disturbances in the horizontal component of the Earth's magnetic field from 0 – 9 with a time resolution of 3 hours. A value of 1 describes calm conditions, while ≥ 5 corresponds to a geomagnetic storm. Since the K values should be about the same for all observatories, the level of geomagnetic disturbance needed for a certain K value is latitude dependent (lower latitudes require less disturbance than higher latitudes for the same K values). As all observatories measure their own K value, a global K value known as the planetary K, the Kp index has been introduced to have one value for the entire Earth.

To obtain the Kp index, first the K values of the different observatories are standardized into K_s, standardized K, indices. Subsequently, the Kp index is found to be the average of the K_s indices. Thus the Kp index is derived by taking a weighted average of 13 magnetometers in mid-latitude regions and also ranges from 0 – 9 with 3 hour intervals. Contrary to the K index, the Kp index is defined on scales of thirds: $0o, 0+, 1-, 1o, 1+, 2-, 2o, 2+, 3-, ..., 8+, 9-, 9o$, where $1o, 2o, 3o, 4o, 5o, 6o, 7o, 8o$ and $9o$ correspond to the integers $1, 2, 3, 4, 5, 6, 7, 8$ and 9. The minus sign resembles a subtraction of 0.33 of the corresponding integer, while the plus sign adds 0.33.

Dst index

The Dst index is a measure of the strength of the ring current, which lies in the equatorial plane. Therefore, four low-latitude observatories are used to measure the horizontal component of the Earth's magnetic field and express it in nano-Teslas. The values are corrected for long-term and diurnal variations in the Earth's magnetic field by defining a quiet baseline value. This baseline is measured during midnight (minimum diurnal variation) on quiet days which are not close to magnetic storm recovery phases. The Dst index is subsequently calculated from the average fields at the four observatories (Banerjee et al., 2012).

As the ring current creates a magnetic field opposite to the Earth's magnetic field, the Dst index is inversely proportional to the energy content of the ring current. A negative Dst index therefore, indicates a weakening of the Earth's magnetic field. Thus during a geomagnetic storm, the Dst index will be negative (Banerjee et al., 2012; Kivelson and Russell, 1995).

2.5 Access of charged particle into the magnetosphere

The ability of charged particles to enter the Earth's magnetosphere is dependent upon the particle's rigidity. Rigidity, measured in momentum per charge, describes the adiabatic charged particle motion in a magnetic field. All particles with the same rigidity, charge sign and initial conditions have identical trajectories when inserted into the same magnetic field (Heino, 2019; Filwett et al., 2020). Störmer (1955) defined the concept of cutoff rigidity as a minimum rigidity a particle must have in order to access a certain geomagnetic latitude. Below the cutoff rigidity, the particle fluxes have decreased to approximately zero due to geomagnetic shielding. For further penetration, a particle with a higher rigidity is needed.

The theoretical cutoff rigidity, R_c for a purely dipole field is given by

$$R_c = C_{st} \frac{1}{L^2(1 + \sqrt{1 + \cos\alpha \cos\lambda^3})} \tag{2.10}$$

where $C_{st} = 60$ is a constant containing the dipole moment and a conversion factor to obtain R_c in GV, L the dipole L value, α the angle between arrival direction of the particle and magnetic west and λ the geomagnetic latitude (Filwett et al., 2020). The dependence on α results in particles arriving from the west having easier access and a lower cutoff rigidity than particles arriving from other directions, leading to an east-west asymmetry. This could lead to a dawn-dusk asymmetry (Scholer, 1975).

As described in Section 2.4, the magnetopause acts as a boundary for the transfer of plasma, mass or momentum from the IMF to the Earth's magnetosphere. The easiest way for solar protons to access the magnetosphere is along the magnetic field lines in the open field line region close to the magnetic poles. In this case, the protons gyrate around the magnetic field line, entering the Earth's atmosphere as they travel closer towards the Earth.

However, energetic particles can access the magnetosphere through other processes as well. The Alfvén criterion only holds when the spatial scales are large compared to gyro radii of charged particles. Since the current sheet of the magnetopause is thin, this approximation can break down in regions where the field lines are highly curved and/or for more energetic particles. In fact, most particles entering the magnetosphere were found to be non-adiabatic (Richard et al., 2002). Due to the break down of Alfvén's theorem the solar wind and the plasma in the Earth's magnetosphere are no longer completely separated. This is referred to as reconnection. During reconnection the magnetic field lines of the IMF can diffuse through the magnetopause and reconnect with terrestial field lines allowing transfer of mass and momentum from the solar wind. Magnetic reconnection is most likely to take place when the angle between the IMF and magnetosphere is maximum, e.g. during anti-parallel configuration (negative B_z component of IMF) (Kalegaev et al., 2018; Herlingshaw, 2020).

Another method to transport energetic particles onto closed field lines becomes possible when the particles are no longer adiabatic and hence the adiabatic invariants can no longer be assumed constant. This is the case for highly curved field lines and/or for more energetic particles ($E > 5$ MeV protons (Richard et al., 2009) or $E > 10$ MeV (Filwett et al., 2020)), since the gyro radius increases with energy. These protons can enter trapped orbits at the dayside of the magnetosphere by jumping from the IMF field lines onto the magnetospheric field lines in one or two distorted gyrations (Richard et al., 2009; Kalegaev et al., 2018).

In addition, during severe geomagnetic storms, a sudden compression of the magnetopause due to an enhancement in the dynamic pressure of the solar wind allows for injection of SEPs into inner L shells. The particles enter on the dayside of the magnetopause at low latitudes and can get trapped inside low radiation belts (Kress et al., 2005).

2.6 Effects increased radiation in Earth's magnetosphere

There are three main sources of particle radiation of which SEPs are one. The other sources are galactic cosmic rays (GCR) and trapped particles in the Earth's radiation belts (Jiggens et al., 2014). GCR mostly consist of protons and heavy ions, while the Earth's radiation belts are largely populated with protons and electrons. During SEPEs, the solar wind intensity increases, shielding the low Earth environment better from GCRs, thus decreasing their effect. The effects described in this section are enhanced during SEPEs. However, the other above mentioned sources of particle radiation can contribute as well.

Main effects of increased radiation levels in the Earth's space radiation environment include malfunction of spacecraft, increased radiation doses, middle atmospheric effects and radio wave absorption among others.

First of all, solar protons provide a risk for spacecraft by causing SEEs, where a single proton or ion deposits enough energy within an electronic component to cause device malfunction. An example of a non-destructive SEE is a bit-flip, where a bit is switched to the opposite logical state. Destructive SEEs include too high operating currents or increases in gate leakage current (Malandraki and Crosby, 2018; Jiggens et al., 2014). SEPs mostly pose a threat to spacecraft in medium Earth orbit (MEO), highly elliptical orbit (HEO) or polar orbit. To show an example of the correlation between SEEs and SEPEs, the events of September 2017 have been used. Jiggens et al. (2019) investigated the effect of the September 2017 SEPEs on spacecraft. The first SEPE took place from 05-09-2017 00:40 – 08-09-2017 23:00 and the second SEPE from 10-09-2017 16:45 – 14-09-2017 17:20. The daily bit error rate (BER) on a solid state

recorder (SSR) on board the Cluster spacecraft over a 20 days period in September 2017 has been plotted in Figure 2.15. The Cluster mission is a collaborative between ESA and NASA and consists of 4 spacecraft in HEO (nominal apogee = 18.7 R_E and perigee = 3 R_E). In addition, the > 30 MeV integral flux as measured by the GOES mission is plotted in green. A clear correlation between the increased proton flux during the SEPEs and the BER is observed. Please note that the zero number of BERs for Cluster-2 and Cluster-3 on 11 September 2017 followed by a high peak on 12 September 2017 is probably a result of delay in correction of the bits or downlinking the BER to ground (Jiggens et al., 2019).

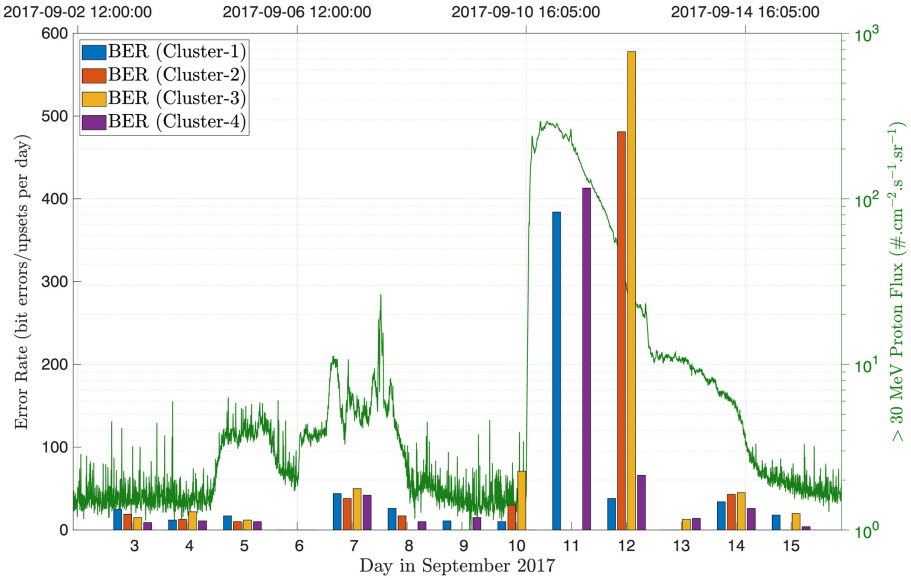

Figure 2.15: The daily bit error rate (BER) on a solid state recorder (SSR) on the Cluster spacecraft (left y-axis) as a function of time (20 day period in September 2017). In addition the > 30 MeV integral proton flux from the GOES mission has been plotted in green (right y-axis). Image retrieved from (Jiggens et al., 2019).

In addition, increased radiation doses pose a threat to humans in space, both in spacecraft and aircraft. Radiation effects can be divided into deterministic (tissue reactions) or stochastic. Tissue reactions are the direct consequence of absorbed radiation doses and have a threshold above which the effect can occur. Examples are acute radiation sickness, hair loss or cataracts. Stochastic effects, such as cancer, are caused by random radiation induced changes to the deoxyribonucleic acid (DNA) and have the probability to increase with every dose. Jiggens et al. (2014) assessed the risk of the August 1972 SEPE that occurred in between the NASA Apollo 16 and 17 lunar missions. If this event would have occurred during one of the missions, it could have resulted in severe health risks to the astronauts on an extravehicular activity. To avoid radiation doses for aircrew, high-latitude and polar-flights can be re-routed during SEPEs (Malandraki and Crosby, 2018). Furthermore, a sufficient shielding thickness, with a minimum of 10 cm Aluminium could help decrease the radiation dose and the probability of SEEs on board spacecraft (Jiggens et al., 2014).

Furthermore, the precipitation of SEP in the Earth's atmosphere results in ionization of neutral atmospheric molecules. Since the average energy to form an electron-ion pair is 35 eV, a 20 MeV proton can produce over half a million electron-ion pairs in the atmosphere. Protons lose most of their energy close to their CL, which is in the mesosphere ($\sim 55 - 85$ km) for 2 – 40 MeV protons and in the stratosphere ($\sim 10 - 55$ km) for > 40 MeV protons (Heino, 2019). In this process, odd nitrogen (NO_x) and odd hydrogen (HO_x) species are formed among others, resulting in amounts well above the background level in especially the stratosphere and mesosphere for large SEPEs. The loss rate of NO_x is dependent on solar illumination, resulting in a long lifetime (order of months) during the polar night. This long lifetime allows for downwards atmospheric transport of NO_x. Subsequently, these highly reactive species can react with ozone, leading to ozone depletion in the middle atmosphere especially in the polar cap. Due to the downward transport of NO_x, this depletion can take place well below its production altitude. In addition, SEPs can alter the radiative balance of the atmosphere in which exothermic chemical reactions could play an important role (Heino, 2019; Nesse Tyssøy and Stadsnes, 2015).

Another change in the atmosphere induced by energetic particle precipitation is the rapid increase in the production of radionuclides in case of extreme SEPEs. These radionuclides are stored in environmental materials, such as ice cores (^{10}Be and ^{36}Cl) and tree rings (^{14}C), which can subsequently be used to identify SEPEs that occurred before the instrumental period (O'Hare et al., 2019).

In addition, increased ionization levels in the *D*-region (60 – 90 km altitude) result in the absorption of radio waves, causing polar cap absorption (PCA). PCA leads to radio blackouts in the HF and VHF bands in the polar regions lasting for several days. As a result, long-distance radio communication used in for example aviation is disrupted and aircraft need to be re-routed to lower latitudes (Neal et al., 2013).

3 Methods

In this chapter, the satellite data relevant to this thesis will be introduced in Section 3.1. The method of obtaining the SEPE list is explained in Section 3.2. The data processing techniques to obtain the CLs are treated in Section 3.3. Lastly, the necessary tools for the statistical study are handled in Section 3.4.

3.1 Satellite data

The proton fluxes used to determine CLs have been empirically measured by GPS satellites from 2001 until 2015. Additionally, measurements from GOES provide the necessary normalization to compensate for changing geomagnetic conditions and proton fluxes during GPS measurements. All satellite data files used in this thesis are publicly available. Information on where to download the files is given in Appendix A.

3.1.1 GPS satellites

The Global Position System (GPS) is not only a vital part of everyday life as it is one of the global navigation satellite systems (GNSSs) widely used to determine positions all around the globe. Many of these satellites carry energetic particle instruments developed by the Los Alamos National Lab (LANL), providing important information about near Earth space. The GPS spacecraft are located in six different MEO planes at an altitude of approximately 20200 km in near-circular orbits. The MEO planes have a nominal inclination of 55°, covering L shells above 4 ($\Lambda > 60°$). Each point on Earth can be seen by ≥ 4 GPS satellites simultaneously. The particle detectors on board the GPS satellites have a nadir orientation, which corresponds to the vertical pointing direction of gravity at a location, meaning that they are looking towards Earth.

Currently there are more than 30 GPS satellites in operation of which 24 carry a Combined X-ray Dosimeter (CXD) instrument. The instrument has been designed to measure both X-rays as part of the U.S. Nuclear Detonation Detection System and energetic particles (Distel et al., 1999). The details of the satellites carrying the CXD instruments during the studied period, 2001 – 2015, can be found in Table 1. Here the space vehicle number (SVN), the North American Aerospace Defense (NORAD) Catalog Number, the international designation (ID) number, the orbit plane, the block and the date from which energetic particle information is available are shown. The block represents the different generations of the GPS satellites.

Combined X-ray Dosimeter

The part of the CXD instruments that measures the energetic particles consists of three different sub-systems containing 11 electron channels (from 0.14 – > 5.8 MeV) and 6 proton channels (from 6 MeV and up). As the goal of this thesis is to determine CLs for energetic protons, the focus will be on the proton channels. The first subsystem, the Low-Energy Particle (LEP) detector, is composed of a stack of 500 micron thick silicon sensors and contains two proton channels, 6 – 10 MeV (P1) and 10 – 50 MeV (P2). Additionally the other two sub-systems, the High-energy X-ray and Particles sensors, HXP1 and HXP2, contain the other three proton channels, 16 – 128 MeV (P3) in HXP1 and 57 – 75 MeV (P4) and > 75 MeV (P5) in HXP2. Those energy ranges are the nominal values of the channels. However, there is also a response outside these ranges as can be seen in the response functions shown in Figure 3.1 (Morley et al., 2016, 2017; Carver et al., 2018). The typical sampling time of the detectors is 240 seconds. More information on the LEP, HXP1 and HXP2 sensors can be found in the paper by Tuszewski et al. (2004) and the Technical Report of Distel et al. (1999) and Cayton (2004).

To enable the use of CXD proton data for scientific purposes, Carver et al. (2018) performed a cross-calibration of the CXD proton channels with the EPS on board the GOES mission. It was found that integral fluxes > 10 MeV are within 40% of the EPS fluxes, while > 30 MeV integral fluxes are within 20% of the EPS values.

Table 1: Details of the GPS satellites carrying CXD instruments. Data has been modified from Morley et al. (2017) and Carver et al. (2018).

SVN	NORAD #	ID	Orbit plane	Block	Data from (mm/yyyy)
ns71	40534	2015–013A	B	IIF	04/2015
ns69	40294	2014–068A	E	IIF	12/2014
ns68	40105	2014–045A	F	IIF	09/2014
ns67	39741	2014–026A	D	IIF	07/2014
ns64	39533	2014–008A	A	IIF	05/2014
ns66	39166	2013–023A	C	IIF	07/2013
ns65	38833	2012–053A	A	IIF	11/2012
ns63	37753	2011–036A	D	IFF	07/2011
ns62	36585	2010–022A	B	IFF	06/2010
ns57	32384	2008–062A	C	IIR-M	01/2008
ns55	32260	2007–047A	F	IIR-M	11/2007
ns58	29601	2006–052A	B	IIR-M	12/2006
ns53	28874	2005–038A	C	IIR-M	10/2005
ns61	28474	2004–045A	D	IIR	11/2004
ns60	28361	2004–023A	F	IIR	07/2004
ns59	28190	2004–009A	C	IIR	03/2004
ns56	27663	2003–005A	B	IIR	02/2003
ns54	26690	2001–004A	E	IIR	02/2001

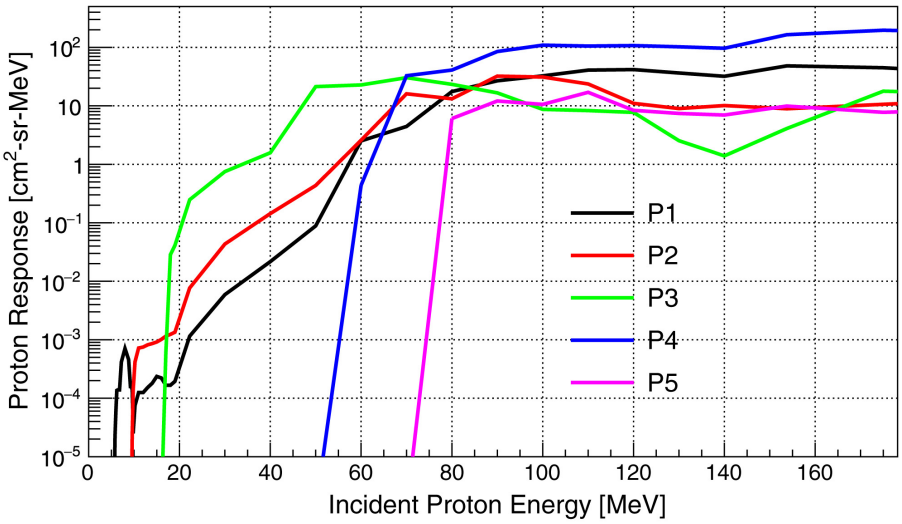

Figure 3.1: A representative set of response curves of the five proton channels of the CXD instrument on board of block IIR GPS satellites before the cross-calibration performed by Carver et al. (2018). Figure retrieved from Carver et al. (2018).

3.1.2 GOES satellites

The Geostationary Operational Environmental Satellites (GOES) mission, which started in 1974, is a joint effort of the National Aeronautics and Space Administration (NASA) and the National Oceanic and Atmospheric Administration (NOAA) to obtain continuous measurements of atmospheric and space weather conditions. The mission predicts and monitors local weather events, forecasts solar disturbances and is part of the Search and Rescue Satellite Aided Tracking (SARSAT) among others.

The GOES mission is currently operating as a two satellite system, with one satellite located at the East location (75° West) and another one at the West location (137.2° West). The satellites are in geostationary

orbit, meaning a circular orbit approximately 35790 km above the Earth ($L \approx 6.6$) in which the satellite stays in the same position with respect to the Earth. Next to the two operational satellites, there are currently two satellites in storage mode, which can take over tasks in case of failures.

As shown in Figure 3.2a, westward-looking detectors detect protons with gyrocenters outside the geostationary orbit of the satellite, while eastward-looking detectors measure protons from inside. Figure 3.2b displays the meridional plane in which it can be seen that values inside the geostationary orbit match with lower L-shell values. It was found that by Rodriguez et al. (2010) that gyrocenters "outside" correspond to $L > 7$, while gyrocenters "inside" correspond to $L = 4.0 - 4.5$ and thus potentially shielded areas. Therefore, only westward-looking detectors of GOES have been used to normalize the GPS fluxes.

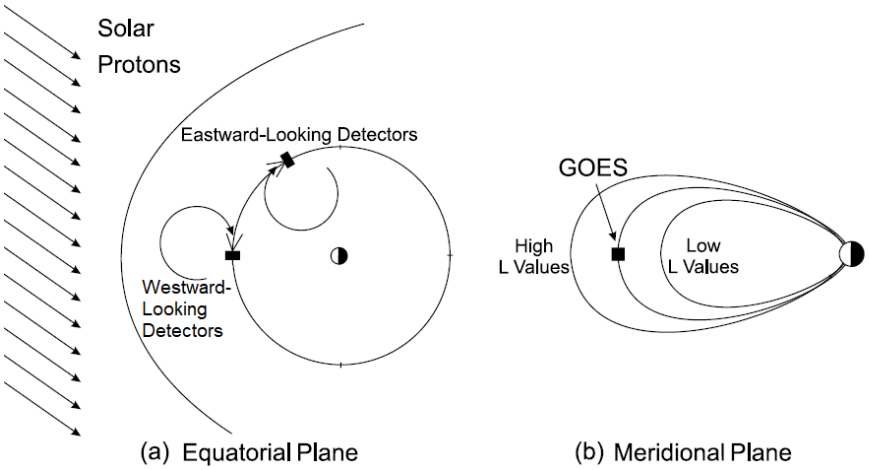

Figure 3.2: Schematic representation of the GOES orientation in (a) the equatorial plane and (b) the meridional plane. Westward- (Eastward)-looking detectors observe solar protons with gyrocenters outside (inside) the geostationary orbit, meaning the solar protons are located at higher (lower) L-shell values. Figure adapted from Rodriguez et al. (2010).

In case of GOES 8 – 12 an Energetic Particle Sensor (EPS) with a single westward field-of-view (FOV) is used, while for GOES 13 the EPS has been replaced by two Energetic Proton, Electron and Alpha Detectors (EPEADs), one with a westward and one with an eastward FOV. It should be noted that the EPS on board of GOES 10 has been used with an eastward FOV as the satellite had to fly inverted (Rodriguez et al., 2010, 2014). Both instruments consist of one telescope and three dome detectors, housing seven proton channels together. P1, P2 and P3 can be found in the telescope, P4 in dome D3, P5 in dome D4 and P6 and P7 in dome D5. More information on the telescope and domes as well as a schematic representation of both can be found in Appendix B.1. The original energy values of the channels and their effective energies as obtained after cross-calibration of the GOES solar proton detectors by Sandberg et al. (2014) can be found in Appendix B.2.

Table 2: The coverage of the different GOES satellites for the time span of this project as described at `http://www.sepem.eu/help/data_pref.html`

Spacecraft	**Timespan**
GOES 08	01-03-1995 – 31-05-2003
GOES 12	01-06-2003 – 20-06-2003
GOES 11	21-06-2003 – 28-02-2011
GOES 13	01-03-2011 – 31-12-2015

The GPS proton data have been normalized with the GOES data, using datafiles with 5-minute intervals from the European Space Agency's (ESA's) Solar Energetic Particle Environment Modelling (SEPEM) repository. Spikes and other corrupted data records have been removed or corrected, background fluxes are subtracted and the proton channels have been interpolated into 11 different energy bins (for data download, see Appendix A). Please note that at the time of writing these datafiles are only available

until 2015 and therefore events after 31-12-2015 have not been taken into account. Table 2 shows which GOES satellites have been used between 2001 – 2015 to construct the SEPEM datafiles.

3.2 Solar energetic particle events list

As mentioned in Subsection 2.3.2, the > 10 MeV proton fluxes measured by the GOES spacecraft are used to determine whether an enhancement in particle precipitation is considered an SEPE.

The list published by the NOAA Space Environment Services Center (`https://umbra.nascom.nasa.gov/SEP/`) only provides a starting and maximum time for each SEPE. Since it is convenient for data processing purposes to have both a start and end time, for this thesis a separate list has been created using the GOES spacecraft listed in Table 2. Additionally, it takes GPS satellites approximately 2.5 hours to pass from a maximum to a minimum L value (or the other way around). Therefore, a certain minimum duration for a SEPE is needed to determine possible CLs, which is longer than the 15 minutes used in the NOAA Space Environment Services Center definition of an SEPE.

In this thesis, the start of a SEPE is defined when at least 12 data points, corresponding to 60 minutes, of the > 10 MeV are at or above 10 pfu. The ending point of a SEPE occurs when at least 4 data points, corresponding to 20 minutes, are below the 10 pfu threshold. This results in a list of 130 events between 2001 – 2015, which can be found in Appendix C.

3.3 Data processing to obtain cutoff latitudes

The CLs of energetic protons are calculated for differential energies corresponding to 18.18, 26.30, 38.03, 54.99, 79.53 and 115 MeV. These energies are chosen based on the interpolated energy values in the de-spiked and background subtracted SEPEM files containing the GOES proton fluxes. All data processing has been performed using Matlab (version 2020b with the Statistics and Machine Learning Toolbox). The first step is to automatically download the GPS data files for each SEPE and store them in a separate folder for each event to simplify further processing. Subsequently, CLs are calculated per event by first uploading the data into Matlab and storing all relevant variables. Then the differential proton fluxes during a SEPE, J_{SEPE}, are interpolated for the desired differential energies using the equation from Cayton et al. (2010)

$$J_{SEPE} = \frac{AN_0}{\exp\frac{43.33}{R_0}} \left(\frac{E}{p}\right) \exp\left(-\frac{p}{R_0}\right), \tag{3.1}$$

where N_0 is the number density fit, R_0 the proton momentum fit, p the proton momentum [MeV c^{-1}], E the total proton energy [MeV], A a normalization factor such that the flux is 1000 protons $cm^{-2}s^{-1}sr^{-1}MeV^{-1}$, resulting in $A = 0.046132$ and 43.33 represents the momentum of a proton with kinetic energy = 1 MeV. It can be re-written to

$$J_{SEPE} = \frac{AN_0}{\exp\frac{43.33}{R_0}} \left(\frac{E + 938.27}{\sqrt{E(E + 1876.54)}}\right) \exp\left(-\frac{\sqrt{E(E + 1876.54)}}{R_0}\right). \tag{3.2}$$

It should be noted that J_{SEPE} does not include the background flux.

Subsequently, two different normalization methods are performed on J_{SEPE} to compensate for changing geomagnetic conditions. The main normalization approach of this thesis involves data from the westward-looking EPS and EPEAD detectors on board the GOES satellites. For this, the GOES SEPEM data is imported into Matlab, after which each GPS data point is linked to the GOES data point closest in time. Then the differential proton fluxes are normalized for all energies by dividing the GPS proton flux by the GOES proton flux. The second normalization method determines the median value in the open field line region ($L > 10$) from the CXD instruments and uses this as normalization value. As this method requires a GPS satellite to be present in the open field line region during all times, it is only possible when a sufficient number of GPS satellites has been equipped with a CXD detector. Please note that the second method is the normalization method performed by Chen et al. (2020) and Carver et al. (2020). In this thesis, the second method is only performed to be able to compare the outcome of both normalization methods in Subsection 4.2.2 and is thus not used for the CL-database.

After both normalization methods are performed, the CLs are determined by separating the data set of each satellite during one SEPE into time periods in which that satellite moves to higher L-shells (outbound) or to lower L-shells (inbound), separating it in time intervals of approximately 2.5 – 3 hours. In Figure 3.3 the differential proton flux for one interval plotted as a function of L-shell is shown. The red line represents the median value of the proton flux in the open field line region ($L > 10$) and the black circle marks the position of the calculated CL. Theoretically, the median is expected to be one in the open field line region as the fluxes measured by the GPS and GOES spacecraft should be equal. However, due to a slight discrepancy between the CXD and EPS detectors (Carver et al., 2018) and potentially partly shielded fluxes, it is not always equal to one.

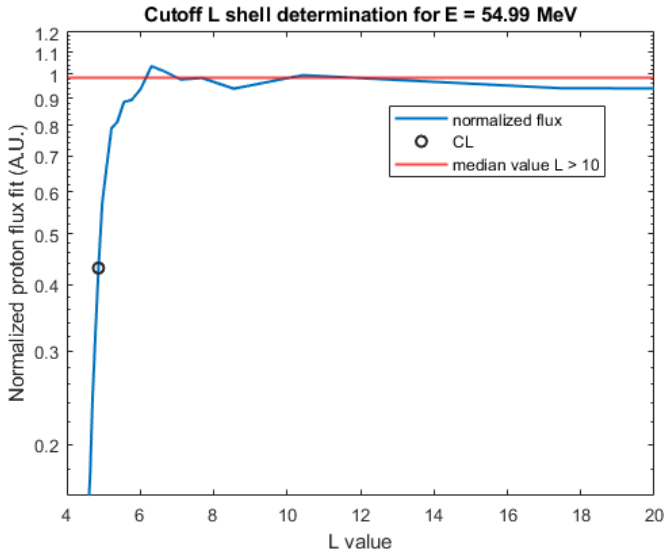

Figure 3.3: Graphical representation of determination CLs. In blue the normalized proton flux for $E = 54.99$ MeV is plotted as a function of the L value. The red line gives the median proton flux in the open field line region ($L > 10$) and the black circle represents the CL at $L = 4.863$.

To calculate CLs, the definition of Leske et al. (2001), which determines the location of a CL as the position where the count rate is half of its mean value in the open field line region is used. The open field line region has been defined as $L > 10$ as reported previously by Chen et al. (2020) and Carver et al. (2020) when processing the CXD proton data. Furthermore, to avoid measurement errors, the median instead of the mean value in the open field line region is used. To ensure data quality, several constraints are added to this:

- There should be at least six data points in the open field line region ($L > 10$) when calculating the median.
- The median should be in between 0.5 and 1.5.
- The standard deviation in the open field line region should be smaller than $2 \times \frac{18.18[\text{MeV}]}{\text{E [MeV]}}$, where E represents the differential proton energy (so the equation becomes 2 for the differential energy 18.18 MeV). Please note that 18.18 MeV is taken because this is the lowest differential energy used in this study.
- The maximum proton flux in the interval cannot be larger than two times the median in the open field line region.
- The value of the CL is determined being the value closest to 50% of the median, while also being in between 45% and 55% of the median.
- The calculated CL should be below $L = 7.5$.
- Events are only taken into account when they contain at least one CL per satellite for either the 26.30, 38.03 or 54.99 MeV energy channel.

In Section 4.2.1 a visualization of the CL behavior for one SEPE is shown.

To finalize the database, the CLs are linked to the geomagnetic data point closest in time. The download location of the files is given in Appendix A. The Kp and Dst indices have time intervals of 3 and 1 hour respectively, while the IMF and solar wind parameters have 5 minutes time resolution. It should be noted that for some disturbed cases, there is no information available for the IMF and solar wind parameters. This will slightly limit the amount of data available for the statistical study.

3.4 Statistical study

To identify driving characteristics and get information about behavior of CLs during SEPEs, a statistical approach is needed. For this, the CL-database, consisting of thousands of CLs, provides the input data. To understand the statistical study, some statistical terminology covering r, R^2_{adj}, P-values, significance and multivariate linear regression (MLR) among others is explained in Appendix D.

To first get a general impression of relevant geomagnetic and solar wind parameters, the Matlab function *"corrplot"* is used. In this way, linear correlation coefficients, r, and their P-values (indicating significance) between all the different independent variables and the dependent variable are determined. Additionally, histograms showing the distributions of different parameters have been made.

Since many different factors are influencing CL behavior, multiple variables should be combined in one relationship. Thus MLR is used. For this the Matlab function *"fitlm"* is used which creates a linear regression model, calculating important parameters such as R^2_{adj}, P-values, regression coefficients and error terms. A higher R^2_{adj}, the adjusted coefficient of determination, means that the model accounts for a larger proportion of the total variability of the outcome and represents the data better.

To obtain an optimal parameterization, the process of backward selection has been used. During this process, first a parameterization including as many independent variables as possible is used, after which the variable with the highest P-value is excluded in the next round. This enables the identification of important predictors as well as finding an optimized R^2_{adj}.

4 Results

The results will be presented in this chapter beginning with the CL-database in Section 4.1. Subsequently, the normalization method is validated in Section 4.2 after which the behavior of CLs is studied in Section 4.3 resulting in optimal cutoff parameterizations. Lastly, a comparison with previous literature is established in Section 4.4.

4.1 Establishing cutoff latitude database

The database of CLs has been created using the constraints described in Section 3.3. This leads to a database containing 5976 CLs from 30 March 2001 until 24 June 2015. In Table 3 the number of CLs per differential energy is given. For higher energies, fewer CLs are found, because the background subtracted version of the GOES proton fluxes goes to zero during less energetic moments of the SEPEs. This results in a non-physical, infinite normalized flux. Therefore, the normalized flux is set to zero for these cases and no CLs can be determined during these periods.

Table 3: Number of CLs 2001 – 2015 determined using proton fluxes from CXD detectors on board GPS spacecraft normalized with EPS proton fluxes measured by the GOES mission.

Energy [MeV]	Number of CLs
18.18	1013
26.30	1456
38.03	1491
54.99	1077
79.53	623
115.0	316

In Figure 4.1, a polar plot with MLAT on the radial axis and MLT in the theta direction shows all CLs with a differential energy of $E = 38.03$ MeV. The color indicates the number of CLs in a square-shaped bin with sides of 1° geomagnetic latitude. It can be seen that all MLT bins are covered in the CL-database. Furthermore, since the GPS satellite network only covers $L > 4$ ($\lambda_c > 60°$, where λ_c is the CL in degrees) and the calculated CLs should be below $L = 7.5$ ($\lambda_c \approx 68.6°$), all CLs in Figure 4.1 are found in this range. In addition, no clear asymmetries in MLT sectors are visible.

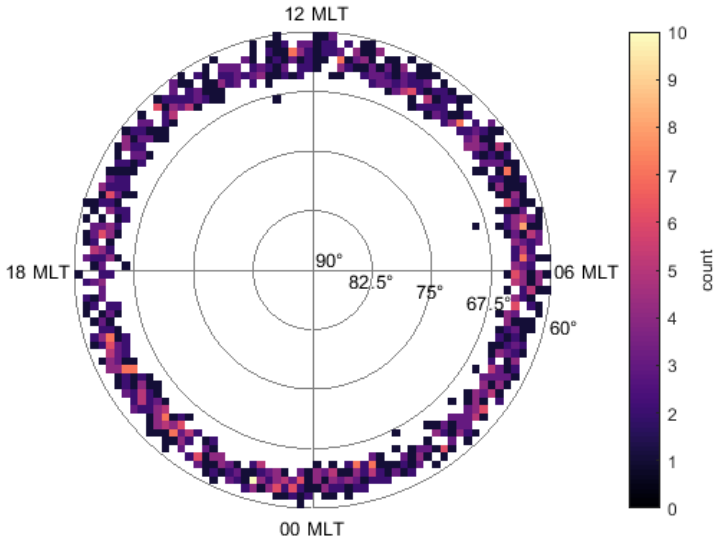

Figure 4.1: Distribution of all CLs with an energy of 38.03 MeV in the CL-database created in this thesis (1491 CLs). The magnetic latitude is shown on the radial axis and MLT in the theta direction. Bins are square-shaped with sides of 1° geomagnetic latitude and the color represents the number of CLs in one bin.

4.2 Validation normalization method

In previous literature, GPS proton data have been used to determine CLs by Chen et al. (2020) and Carver et al. (2020). In both studies, normalization is performed using proton fluxes from GPS satellites in the open field line region ($L > 10$ for these papers). To be able to use this method, there should be at least one satellite at $L > 10$ during all times. It is therefore not possible to determine CLs when only a few GPS satellites carry a CXD detector. This was the case during solar cycle 23 which had its last SEPE in December 2006.

To extend the use of the GPS data to the entire period of CXD coverage, including 63 events of solar cycle 23, a different normalization method will be used involving proton fluxes from the GOES missions. To my knowledge, GOES data has never been used to normalize GPS proton fluxes. Therefore, this novel method will be validated by performing both a visual and a quantitative comparison with the normalization method used by Chen et al. (2020) and Carver et al. (2020).

4.2.1 Visual validation

For the visual validation, the SEPE of January 2014 is used as a benchmark event. Figure 4.2 shows the graphs plotted by Carver et al. (2020) with the normalized (bottom) and non-normalized (top) version of the integral proton flux > 10 MeV as a function of time and L value. The white color in the bottom graph, with a normalized proton flux between 0.4 and 0.6, represents the location of the CL. Furthermore, the value of the *Dst* index has been plotted on top of the bottom graph (yellow line) to show the correlation with the geomagnetic shielding.

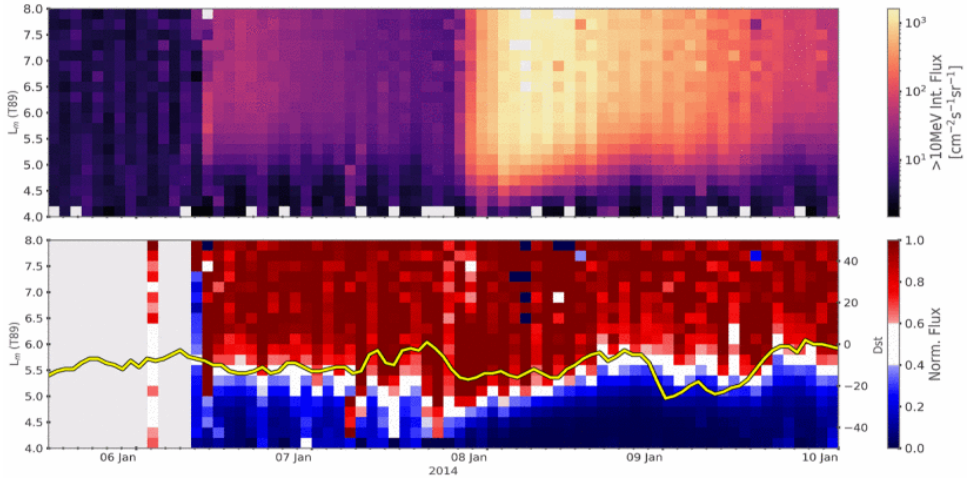

Figure 4.2: Non-normalized (top) and normalized (bottom) version of the integral proton flux > 10 MeV as a function of L shell value versus time. In the bottom figure, the color-scale shows the normalized flux value, where white is the approximate location of the CL. *The Dst index has been plotted on top in yellow. Figure retrieved from Carver et al. (2020).*

When applying the same visualization method (L-shell bins of $\Delta L = 0.2$ and time bins of 1.5 hour), first the non-normalized plot has been re-created to demonstrate proper data handling. As can be seen in the top panel of Figure 4.3, the time axis match and the integral flux shows the same behavior as in Figure 4.2. This is expected, since the input data should be the same. White spots represent data bins without input.

To check the normalization method, the proton fluxes of six differential energies from the CXD detector have been normalized with EPS differential proton fluxes from the GOES mission. For the differential energy 38.03 MeV, the result is shown in the bottom panel of Figure 4.3. On top, the calculated CLs are plotted in black. The light grey areas represent data bins that are equal to zero. This is the case at the start of the event, because here the differential proton fluxes from the GOES mission used for normalization are equal to zero, hence resulting in a non-physical normalization value going to infinity. All these values have been set to zero. It should be noted that Carver et al. (2020) normalized the integrated

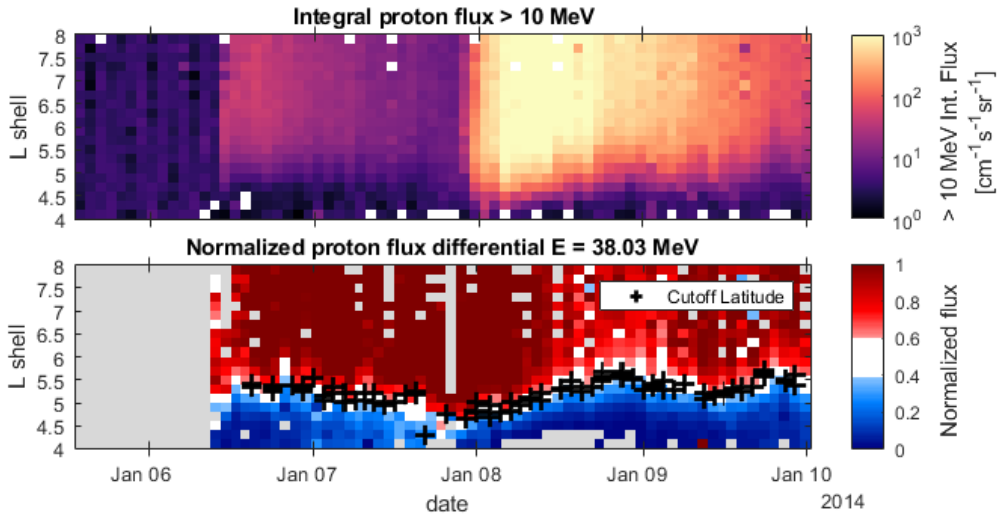

Figure 4.3: (Top) Non-normalized version of the integral proton flux > 10 MeV as a function of time and L during the SEPE *of January 2014. (Bottom) The* CXD *proton flux of E = 38.03 MeV of the* GPS *satellites normalized with the* EPS *proton fluxes of the* GOES *mission. For resemblance with Figure 4.2, the time has been binned in 90 minutes intervals and L-shell values in intervals of 0.2 for both graphs.*

flux > 10 MeV, while for this thesis only differential fluxes have been normalized. Since a CL depends on the energy of the particle, a slightly different L-shell location of the CL compared to Figure 4.2 is expected. Furthermore, due to small discrepancies between the proton fluxes measured by the EPS and CXD detectors, the normalized flux sometimes exceeds 1. This is shown in the bottom panel of Figure 4.3 as bins with the dark red color equal to or exceeding 1.

In general, both normalization method visually result in comparable CL behavior for the January 2014 event. In Subsection 4.2.2, a more quantitative comparison is performed between CLs calculated using the different normalization methods.

4.2.2 Quantitative validation

In addition to the visual comparison shown in Subsection 4.2.1 a quantitative approach has been used to study the differences between the normalization method applied by Carver et al. (2020) and Chen et al. (2020) and the one applied in this thesis in more detail. For this, CLs have been calculated using the same Matlab script. In the first case, the normalized differential proton fluxes have been calculated using the GOES mission as a normalization method (normalization method 1 from now on), while for the second case, the CXD detectors in the open field line region have been used for normalization (normalization method 2 from now on). Subsequently, the CLs determined with both normalization methods have been linked to one another. For this, CLs should be found within 60 minutes of each other, to ensure that they take place in the same orbit segment of the satellite. Additionally, CLs have to be recorded by the same satellite.

Table 4: Mean difference percentage in L value between the two normalization methods.

Energy [MeV]	**Mean difference**	**Difference percentage [%]**	**Number of linked CLs**
18.18	-0.0087	2.9	491
26.30	0.0093	2.5	796
38.03	-0.0066	1.9	903
54.99	-0.0057	1.5	656
79.53	0.0080	1.4	398
115.0	0.0119	1.7	188

The difference in L value was calculated by subtracting the L value of linked CLs. For each energy, the mean difference and a difference percentage are shown in Table 4. Additionally, the number of linked CLs per energy is listed in Table 4 as well. The mean difference has been calculated by subtracting the L value calculated using normalization method 2 from the one calculated with normalization method 1. This value is negative for as many energies as it is positive, indicating no clear difference between the two normalization methods. To further study the distribution of the difference in L value, histograms of the difference are made for each energy. For $E = 38.03$ MeV, this distribution is shown in Figure 4.4 with a Gaussian distribution fitted on top.

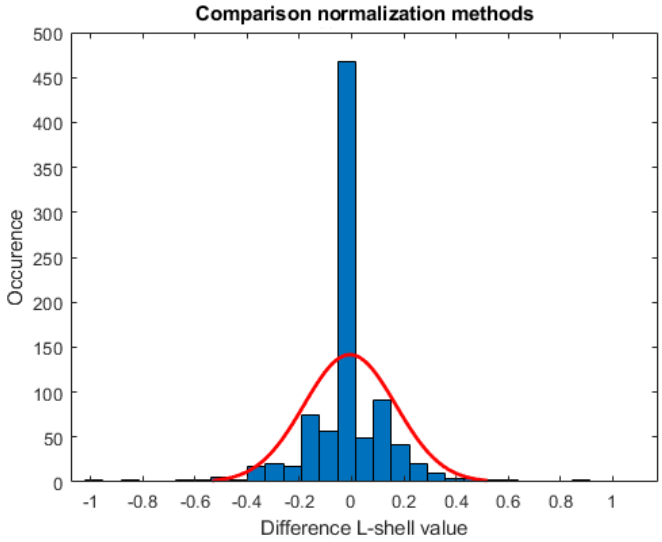

Figure 4.4: Difference in L value between 903 linked CLs for $E = 38.03$ MeV with a Gaussian distribution fitted on top in red ($\mu = 0.012$ and $\sigma = 0.23$). The difference between the two normalization methods is 1.9%.

Since the differences in L value between the two normalization methods are relatively small and lack any clear trend, it is concluded that normalization method 1, involving the GOES mission provides reliable results and can thus be used as main normalization method in the rest of this thesis.

4.3 Behavior of cutoff latitudes

To get a better understanding of the behavior of CLs, first the effect of single parameters will be investigated in Subsection 4.3.1, after which a backward selection is used to obtain an optimal parameterization for each energy in Subsection 4.3.2. Subsequently, the energy and MLT dependence are studied in more detail in Subsections 4.3.3 and 4.3.4.

4.3.1 Driving characteristics

To identify driving characteristics of CLs, first linear regression between the L-value and single geomagnetic and solar wind parameters is performed. The following explanatory variables were chosen for the univariate linear regression: geomagnetic Kp and Dst indices, the components of the IMF and the dynamic solar wind pressure.

Dst and Kp indices

The ring current index, Dst, and the geomagnetic activity index, Kp, are used as geomagnetic activity indicators, since both of them are available in near real time. Additionally, the correlation between cutoff behavior and either of the indices has been investigated in previous literature such as papers from Leske et al. (2001); Nesse Tyssøy and Stadsnes (2015); Dmitriev et al. (2010); Birch et al. (2005) and Neal et al. (2013).

Neal et al. (2013) discovered that the Kp index has a predictive value, forecasting the CL behavior approximately 3-hours in the future. This parameter is called Kp_{shift}. In addition, Neal et al. (2013)

found a better correlation when combining the linear and squared version of Kp_{shift}. Therefore, the variable Kp_{shift} as well as the squared version are also investigated in this section. The results for $E = 38.03$ MeV are shown in Figure 4.5 with the linear regression between the cutoff L shell values and Kp (left), Kp_{shift} (middle) and Dst (right) in the top row. The bottom row shows the regression for Kp^2 (left), Kp^2_{shift} (middle) and a combination of Kp_{shift} and Kp^2_{shift} (right). The R^2_{adj}-value is displayed above each graph. Additionally, the red lines indicate the regression formula, with the 95% confidence bounds shown as dashed red lines.

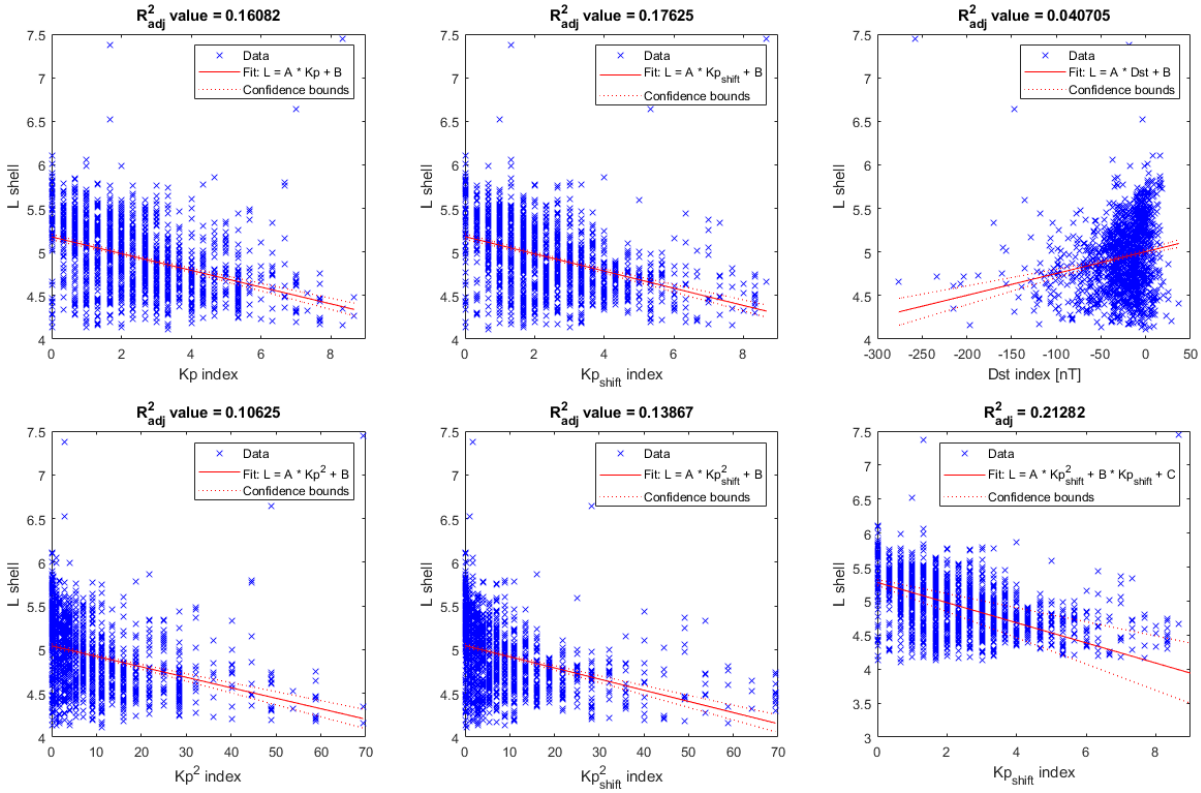

Figure 4.5: Linear regression applied on cutoff L-shell values for $E = 38.03$ MeV. L shell is represented as a function of: (top) Kp (left), Kpshift (middle) and Dst (right); bottom: Kp^2 (left), $Kpshift^2$ (middle) and Kp_{shift} and Kp^2_{shift} (right). The R^2_{adj}-value is shown at the top of each graph and all graphs have P-values $\ll 0.05$. The data points are given in blue, the fit is shown in red and the the red dashed lines represent the 95% confidence bounds.

A positive correlation between the cutoff L-shell and the Dst index indicates that a more negative Dst value, meaning stronger geomagnetic activity, leads to a smaller cutoff L-shell. Since the L-shell value is inversely proportional with the CL according to Equation 2.7, energetic protons can travel further equatorward during enhanced geomagnetic activity. This is in agreement with previous literature, although in some cases, this correlation with the Dst index can only be found during strong magnetic storms (Dst index ≤ -100 nT) (Chu and Qin, 2016). This could partly explain the large amount of scatter and the low R^2_{adj}-value.

Both the Kp and the shifted Kp index display a negative correlation with the the cutoff L shell, indicating that more geomagnetic activity allows solar protons to access lower CLs. As reported by Neal et al. (2013), the Kp_{shift} shows a higher correlation as displayed by a higher R^2_{adj}-value. The same is seen when comparing the R^2_{adj}-value of Kp^2 and Kp^2_{shift}. Additionally, it can be seen that combining Kp_{shift} and Kp^2_{shift} results in a better correlation. Therefore, both Kp_{shift} and Kp^2_{shift} are used for the backward selection in Section 4.3.2 rather than Kp and Kp^2.

Interplanetary Magnetic Field components

Applying linear regression to the B_x, B_y and B_z components of the IMF, results in the graphs shown in

Figure 4.6. The linear regression between the L cutoff value and the B_x component (left), B_y component (middle) and B_z component (right) of the IMF are depicted with the R^2_{adj}-value above each plot. Here, it can be seen that it is possible to draw a straight line in between the 95% confidence bounds (red dashed lines), indicating insignificant results. This is supported by the high P-values and the very low R^2_{adj}, indicating no correlation.

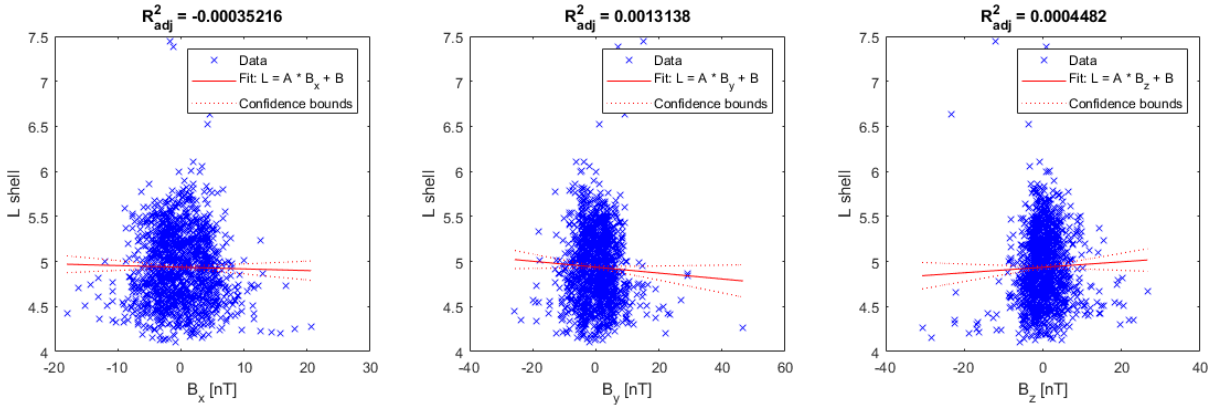

Figure 4.6: Linear regression applied on cutoff L-shell values for $E = 38.03$ MeV as a function of B_x (left), B_y (middle) and B_z (right), which have P-value 0.48, 0.09 and 0.20 respectively. The corresponding R^2_{adj}-value is shown above each graph. The fit is shown in red and the the red dashed lines represent the 95% confidence bounds.

It should be noted that only the results for $E = 38.03$ MeV are shown in this example. For other energies, P-values are below 0.05 for some of the variables. The significant IMF variables are: B_x (at 18.18, 26.30 and 115 MeV), B_y (at 115 MeV) and B_z (at 18.18, 26.30, 54.99 and 79.53 MeV). In the backward regression (Subsection 4.3.2), the IMF components are only included if they are significant for a energy.

Dynamic solar wind pressure

Since the location of the magnetopause is determined by the pressure balance of the dynamic solar wind pressure, P_{dyn}, and the pressure inside the magnetopause, an enhancement in solar wind, pushes the magnetopause further towards the Earth. The location of the magnetopause is inversely proportional to P_{dyn} to the power 1/6 (Ganushkina et al., 2018). Additionally, Nesse Tyssøy and Stadsnes (2015) find an optimal correlation for P_{dyn} to the power 1/3.

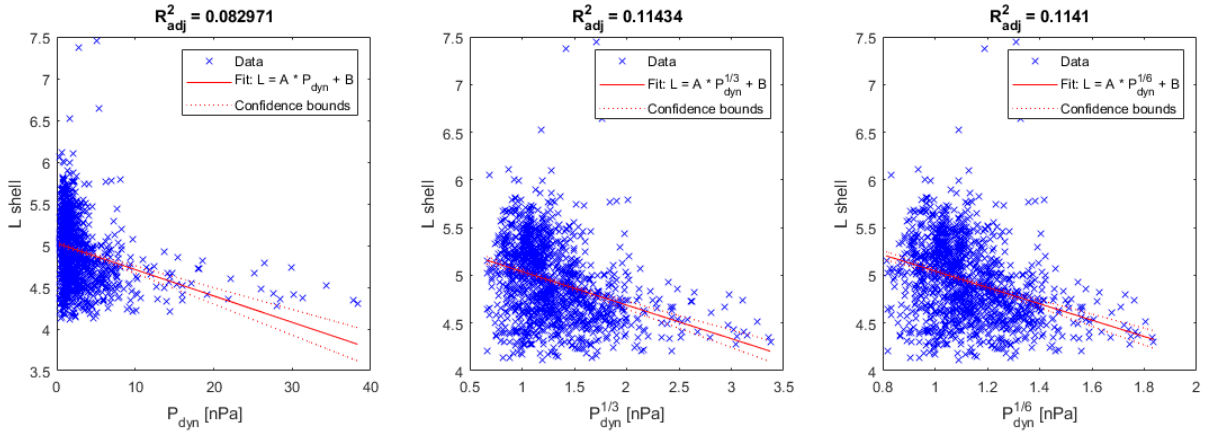

Figure 4.7: Linear regression applied on cutoff L-shell values for $E = 38.03$ MeV as a function of P_{dyn} (left), $P^{1/3}_{dyn}$ (middle) and $P^{1/6}_{dyn}$ (right), which have P-values $\ll 0.05$. The corresponding R^2_{adj}-value is shown at the top of each graph. The fit is shown in red and the the red dashed lines represent the 95% confidence bounds.

In Figure 4.7 the linear regression for different powers of P_{dyn} is shown with the R^2_{adj} value on top of each graph. It can be seen that the R^2_{adj}-value is equally high for P_{dyn} to the power 1/3 and 1/6 with a slight

preference for 1/3. Therefore, $P_{dyn}^{1/3}$ will be used as predictor in the backward regression as performed in Section 4.3.2.

Magnetic Local Time

MLT ranges from 0 – 24 hr or 0 – 360° resulting in a discontinuity at midnight. Therefore, MLT cannot be used as a variable in the multivariate linear regression. However, the CLs will be split into dawn (03 – 09 MLT), day (09 – 15 MLT), dusk (15 – 21 MLT) and night (21 – 03 MLT) sectors to study the differences in CL behavior at different MLTs.

4.3.2 Backward selection multivariate linear regression

During the backward regression, MLR is performed in which all interesting variables are included at the start. The variable with the highest P-value is left out in the next iteration. In the end, the parameterization with the highest R^2_{adj} value for which all P-values are below 0.05 is chosen to be the optimal relation. Since the CLs for different energies vary, the starting equation varies per energy and the end result might vary as well.

The starting point for the backward regression is the relation

$$L = ADst + BP_{dyn}^{1/3} + CKp_{\text{shift}} + DKp_{\text{shift}}^2 + EB_x + FB_y + GB_z + H, \tag{4.1}$$

in which A, B, C, D, E, F, G and H are regression coefficients. Please note that B_x, B_y and B_z are only included if they showed significance in the univariate regression as performed in Subsection 4.3.1.

Table 5: The optimal parameterization for the cutoff L shell based on backwards regression for each energy.

Energy [MeV]	**Optimal parameterization cutoff L shell =**	$\boldsymbol{R_{adj}^2}$	**Number of CLs**
18.18	$ADst + BP_{dyn}^{1/3} + CKp_{\text{shift}} + DKp_{\text{shift}}^2 + EB_x$	0.1584	1013
26.30	$BP_{dyn}^{1/3} + CKp_{\text{shift}} + DKp_{\text{shift}}^2 + EB_x$	0.1821	1456
38.03	$BP_{dyn}^{1/3} + CKp_{\text{shift}} + DKp_{\text{shift}}^2$	0.2154	1491
54.99	$ADst + BP_{dyn}^{1/3} + CKp_{\text{shift}} + DKp_{\text{shift}}^2 + GB_z$	0.3078	1077
79.53	$ADst + BP_{dyn}^{1/3} + CKp_{\text{shift}} + DKp_{\text{shift}}^2 + GB_z$	0.3257	623
115	$ADst + BP_{dyn}^{1/3} + CKp_{\text{shift}} + DKp_{\text{shift}}^2 + FB_y$	0.1896	316

The optimal parameterizations with their R^2_{adj} values are given in Table 5 for each energy. The regression coefficients are given in Table 6. Coefficient H implies that higher energies generally penetrate further into

Table 6: Values of the regression coefficients for the optimal parameterization as given in Table 5.

Energy [MeV]	$\boldsymbol{A}$	$\boldsymbol{B}$	$\boldsymbol{C}$	$\boldsymbol{D}$	$\boldsymbol{E}$	$\boldsymbol{F}$	$\boldsymbol{G}$	$\boldsymbol{H}$
18.18	0.0031 ± 0.0008	−0.31 ± 0.05	−0.12 ± 0.03	0.015 ± 0.005	−0.008± 0.004			5.71 ± 0.07
26.30		−0.24 ± 0.04	−0.17 ± 0.02	0.015 ± 0.003	−0.006± 0.002			5.59 ± 0.04
38.03		−0.19 ± 0.03	−0.19 ± 0.02	0.018 ± 0.003				5.48 ± 0.04
54.99	0.0010 ± 0.0004	−0.22 ± 0.03	−0.21 ± 0.02	0.025 ± 0.003			0.006 ± 0.002	5.50 ± 0.04
79.53	0.0030 ± 0.0006	−0.26 ± 0.04	−0.14 ± 0.02	0.019 ± 0.004			0.006 ± 0.002	5.43 ± 0.05
115	0.002 ± 0.001	−0.19 ± 0.06	−0.11 ± 0.03	0.013 ± 0.006		0.013 ± 0.004		5.14 ± 0.09

the Earth's atmosphere, because a smaller L value corresponds to a lower CL described by Equation 2.7. Coefficient A shows a positive relation with the Dst index, meaning more geomagnetic activity (larger negative Dst value) will lead to further penetration into the Earth's atmosphere. Coefficient B gives the relation with dynamic pressure to the power of 1/3. When the dynamic pressure increases, the magnetopause is pushed towards the Earth, making it easier for energetic particles to access lower geomagnetic latitudes. The negative sign for coefficient B indicates further penetration when the dynamic pressure increases. The negative sign in front of coefficient C represents the further penetration during stronger magnetic activity (larger Kp index). The positive value of coefficient D compensates for the fact that the Kp dependence is not purely linear. Lastly, it can be seen that the regression coefficients for B_x, B_y and B_z are relatively small with large standard errors, because these parameters are highly scattered as shown in the univariate regression in Subsection 4.3.1.

The parameterization found by backward regression for $E = 54.99$ MeV is shown in Figure 4.8. The relation is plotted in black on top of the normalized fluxes for this energy and the individual CLs are plotted in grey. As in Figure 4.3, white bins represent the cutoff region, dark red corresponds to bins equal to or exceeding 1 and light grey to bins with missing data. More data is missing, because of the lower number of GPS satellites equipped with CXD instruments (11 in March 2012 versus 13 in January 2014).

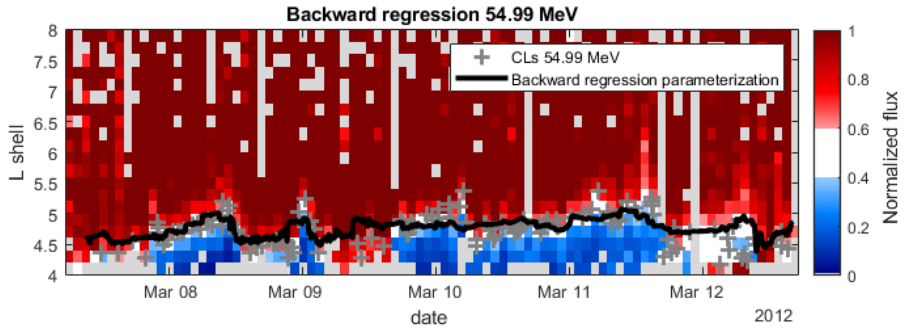

Figure 4.8: The normalized fluxes of the SEPE from 7 – 12 March 2012 plotted for $E = 54.99$ MeV. On top the individual CLs for $E = 54.99$ MeV during this event are plotted in grey as well as the optimal parameterization found with backward regression in black.

The R^2_{adj} values in Table 5 are highest for 54.99 and 79.53 MeV. Based on this observation, a hypothesis is formulated that the higher correlation is caused by the normalization method. For higher energies, the GOES differential flux sometimes goes to zero, taking only the more energetic moments into account. To validate the hypothesis, only the CLs during the intervals that the normalized 79.53 MeV flux is nonzero are taken into account for the lower energies. Applying the backward regression selection procedure again results in the optimal parameterizations shown in Table 7 and the regression coefficients listed in Table 8. As expected, the correlation represented by R^2_{adj} increases for the more energetic moments of the SEPEs. This is due to the fact that the absolute measurement errors are the same for high and low fluxes. However, the relative errors become much larger in both the GOES and GPS fluxes when they are small. Therefore, the normalized flux during quieter times will have a bigger uncertainty leading to a larger spread in cutoff values.

The higher correlation is also visible in the regression coefficients in Table 8. The A coefficient, representing the importance and effect of the Dst index, decreases from low energies to higher energies. Thus the Dst index has a stronger effect for the lower energies, which is in agreement with results presented by both Nesse Tyssøy and Stadsnes (2015) and Neal et al. (2013). Additionally, B indicates that the lower energies are more strongly affected by $P^{1/3}_{dyn}$ as reported by Nesse Tyssøy and Stadsnes (2015) as well.

Despite the fact that the R^2_{adj} values increase when only the more energetic moments of the SEPEs are taken into account, it should be noted that they are still relatively low compared to previous literature (e.g. (Nesse Tyssøy and Stadsnes, 2015; Neal et al., 2013; Birch et al., 2005). This will be discussed further in section 5.2.

Table 7: The optimal parameterization to determine the cutoff in L shell value for all energies below $E = 79.53$ MeV is shown obtained with backward regression. Only the moments when the normalized $E = 79.53$ MeV is unequal to zero are taken into account.

Energy [MeV]	**Optimal parameterization cutoff L shell =**	R_{adj}^2	**Number of CLs**
18.18	$ADst + BP_{dyn}^{1/3} + CKp_{\text{shift}} + DKp_{\text{shift}}^2 + EB_x + GB_z$	0.3253	542
26.30	$ADst + BP_{dyn}^{1/3} + CKp_{\text{shift}} + DKp_{\text{shift}}^2 + GB_z$	0.3279	810
38.03	$ADst + BP_{dyn}^{1/3} + CKp_{\text{shift}} + DKp_{\text{shift}}^2 + GB_z$	0.3076	900
54.99	$ADst + BP_{dyn}^{1/3} + CKp_{\text{shift}} + DKp_{\text{shift}}^2 + GB_z$	0.3215	806

Table 8: The regression coefficients of the optimal parameterization to determine the cutoff in L shell value for all energies below $E = 79.53$ MeV is shown obtained with backward regression. Only the moments when the normalized $E = 79.53$ MeV is unequal to zero are taken into account.

Energy [MeV]	***A***	***B***	***C***	***D***	***E***	***F***	***G***	***H***
18.18	0.0051 ± 0.0009	-0.39 ± 0.06	-0.17 ± 0.03	0.026 ± 0.006	-0.013 ± 0.004		0.009 ± 0.003	5.93 ± 0.08
26.30	0.0023 ± 0.0006	-0.32 ± 0.04	-0.15 ± 0.02	0.015 ± 0.004			0.006 ± 0.003	5.77 ± 0.05
38.03	0.0018 ± 0.0006	-0.23 ± 0.04	-0.23 ± 0.02	0.027 ± 0.003			0.006 ± 0.003	5.66 ± 0.05
54.99	0.0012 ± 0.0006	-0.22 ± 0.03	-0.21 ± 0.02	0.025 ± 0.003			0.006 ± 0.003	5.52 ± 0.05

4.3.3 Energy dependence

When comparing the different energies, regression coefficient H implies lower cutoff latitudes for higher energies. To study this effect in more detail, the regression equations obtained in Subsection 4.3.2 are plotted for the event of March 2012 and January 2014. For this the regression coefficients from Table 8 are used for energies 18.18, 26.30, 38.03 and 54.99 MeV (only taking into account the more energetic moments of SEPEs). The coefficients for 79.53 and 115 MeV can be found in Table 6. The results are shown in Figures 4.9 and 4.10 for the March 2012 and January 2014 SEPEs respectively. Since different energies are combined, no normalized flux has been plotted in the background.

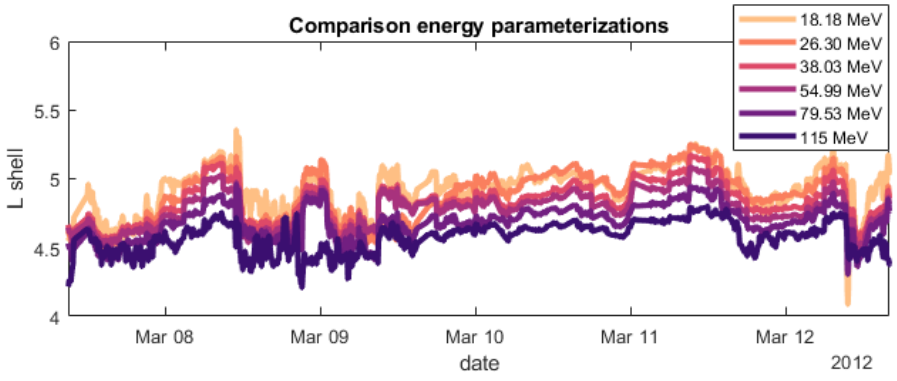

Figure 4.9: Comparison of the parameterizations obtained with backward regression for different energies shown for the SEPE of 7 – 12 March 2012.

It can be seen that higher energies generally penetrate deeper into the Earth's atmosphere. However, the difference is less pronounced for the lower differential energies, since the energy steps are smaller.

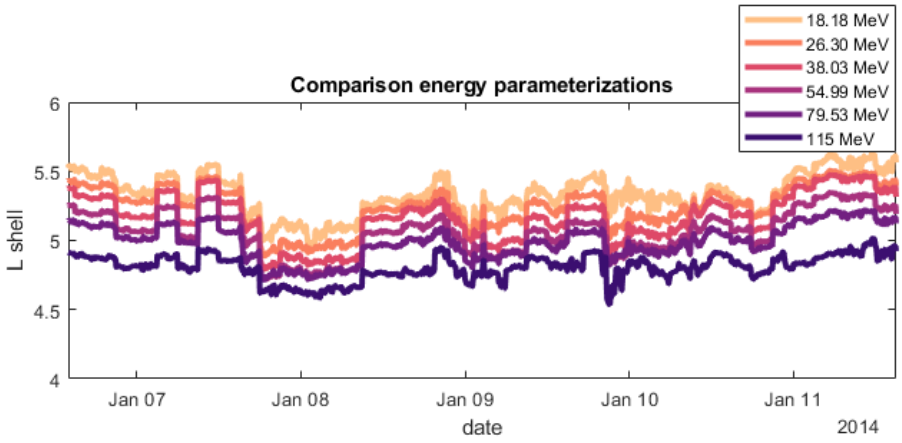

Figure 4.10: Comparison of the parameterizations obtained with backward regression for different energies shown for the SEPE *of 6 – 11 January 2014.*

Furthermore, the six different energy channels result in three different optimal parameterizations involving different parameters. This results in short time frames during which the cutoff distribution is no longer deepest for the highest energies as expected. This can for example be seen on 12 March 2012 in Figure 4.9. Due to a high B_x component, the 18.18 MeV protons are predicted to penetrate deepest, which is not realistic.

In addition, it can be observed that the energy lines are better separated during the January 2014 event (Figure 4.10) than the March 2012 event (Figure 4.9). Especially the 24 hours after the peak of the March 2012 event (around noon at 8 March) show a non-clear energy distinction. This could be caused by the difference in peak flux of the event. The March 2012 event has the highest peak flux of solar cycle 23 and is over six times more powerful than the January 2014 event ($>$ 10 MeV integral flux of 6530 pfu versus 1033 pfu), leading to CLs equatorward from $L = 4$. However, since the GPS satetllites only cover $L > 4$, the obtained parameterization is less accurate for the most intense part of the March 2012 event. This could result in larger errors and thus less clear energy distinction.

4.3.4 MLT dependence

The topic of MLT dependence of CLs has been investigated by Fanselow and Stone (1972), Dmitriev et al. (2010) and Nesse Tyssøy and Stadsnes (2015) among others. It originates from the compressed geomagnetic magnetic field on the dayside of the Earth. The day-night (dawn-dusk) asymmetry is characterized by further penetration on the night- (dusk-)side and is reported to decrease for higher energies. To investigate MLT variations, despite the discontinuity at midnight as mentioned in Subsection 4.3.1, the backward regression has been performed for different MLT sectors. Again, the IMF components are only taken into account when showing significance in the univariate regression.

Table 9: The R^2_{adj} values when applying backward regression to the different MLT *sectors only taking into account the* CLs *during which the 79.53 MeV flux is unequal to zero.*

Energy [MeV]	**Dawn (03 – 09 MLT)**	**Day (09 – 15 MLT)**	**Dusk (15 – 21 MLT)**	**Night (21 – 03 MLT)**
18.18	0.3588	0.4936	0.1389	0.2318
26.30	0.3786	0.3509	0.3060	0.2714
38.03	0.3133	0.3933	0.3741	0.2486
54.99	0.2714	0.4300	0.3856	0.3942
79.53	0.3633	0.3044	0.4035	0.3176
115	0.4308	0.2326	0.0359	0.0841

In Table 9, R^2_{adj} values for the different energies are given when only taking into account CLs when the

normalized flux of 79.53 MeV is unequal to zero (see hypothesis Subsection 4.3.2). According to literature, the lower energies should exhibit a larger MLT dependence, because of their more complicated dynamics (Dmitriev et al., 2010; Fanselow and Stone, 1972; Nesse Tyssøy et al., 2013). Because of the larger error in cross-calibration between CXD and EPS fluxes as performed by Carver et al. (2018) (see Subsection 3.1.1), $E = 26.30$ MeV will be studied in more detail rather than $E = 18.18$ MeV.

Table 10: The optimized parameterizations with their regression coefficients for different MLT *sectors determined for* $E = 26.30$ *MeV.*

MLT sector	Optimal parameterization: cutoff L shell	A	B	C	D	H	Number of CLs
Dawn	$ADst + BP_{dyn}^{1/3} + CKp_{\text{shift}} + DKp_{\text{shift}}^2 + H$	0.003 ± 0.001	-0.35 ± 0.07	-0.18 ± 0.05	0.019 ± 0.008	5.9 ± 0.1	215
Day	$CKp_{\text{shift}} + H$			-0.14 ± 0.01		5.44 ± 0.05	183
Dusk	$ADst + BP_{dyn}^{1/3} + CKp_{\text{shift}} + DKp_{\text{shift}}^2 + H$	0.004 ± 0.001	-0.39 ± 0.09	-0.22 ± 0.05	0.034 ± 0.009	5.8 ± 0.1	194
Night	$ADst + BP_{dyn}^{1/3} + CKp_{\text{shift}} + DKp_{\text{shift}}^2 + H$	0.003 ± 0.001	-0.33 ± 0.07	-0.12 ± 0.04	0.014 ± 0.006	5.7 ± 0.1	218

In Table 10 the optimal parameterizations and the corresponding regression coefficients are displayed for $E = 26.30$ MeV. To visualize these parameterizations, they have been plotted on top of the normalized flux as shown in Figure 4.11. Again, the grey bins represent bins without data input, while the white bins represent the cutoff range.

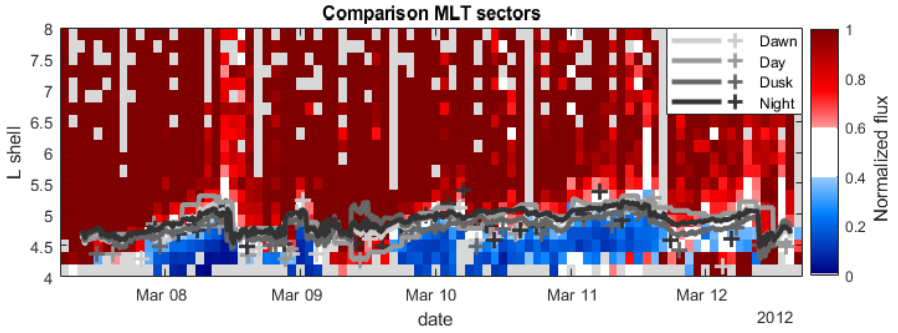

Figure 4.11: The parameterizations obtained for different MLT *sectors (dawn: 03 – 09* MLT*, day: 09 – 15* MLT*, dusk: 15 – 21* MLT *and night: 21 – 03* MLT*) shown for* $E = 26.30$ *MeV plotted on top of the normalized proton flux for the* SEPE *of 7 – 12 March 2012. Additionally, the* CLs *are plotted with a + marker in corresponding color for the different sectors.*

To zoom further in on the relations for the MLT sectors, they are displayed in Figure 4.12 without normalized flux in the background. In general it can be seen that dusk protons (pink line) penetrate furthest. An exception takes place around noon on 9 March, when the peak flux of the event is reached and the parameterization is less accurate. The different parameterization for night (purple line) and day (dark orange line), make it more difficult to compare the day - night asymmetry. It can be seen that the nightside has a lower CL except during high Kp_{shifted} values (9 March around noon).

It should be noticed that the differences in graphs in Figures 4.11 and 4.12 are small and therefore no clear asymmetries are found. This is supported by the plot of all CLs for $E = 38.03$ MeV in Figure 4.1 where no clear MLT asymmetry is visible.

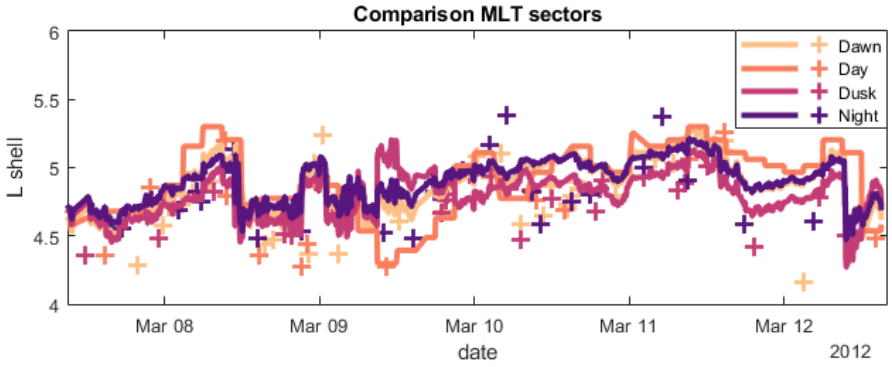

Figure 4.12: The parameterizations obtained for different MLT *sectors (dawn: 03 – 09* MLT*, day: 09 – 15* MLT*, dusk: 15 – 21* MLT *and night: 21 – 03* MLT*) shown for* $E = 26.30$ *MeV for the* SEPE *of 7 – 12 March 2012. Additionally, the* CLs *are plotted with a + marker in corresponding color for the different sectors.*

4.4 Comparison with results from previous literature

To place CL behavior, correlation values and found parameterizations into perspective, the CL-database created in this thesis has been compared to previous findings in literature. More specifically, the empirical models defined by Neal et al. (2013) and Nesse Tyssøy and Stadsnes (2015) will be used for a more thorough evaluation of the database.

4.4.1 Comparison to Neal et al. (2013)

Neal et al. (2013) use POES satellites to empirically determine the access of solar protons into the Earth's atmosphere and their geomagnetic CL. In total 15 large SEPEs between 2003 – 2012 have been included in the study, resulting in a database of 16850 cutoff estimations spread over three energy channels. The approximate center energies of those channels are 24.3, 51.5 and 101.0 MeV at the satellite locations and 37.2, 76.7 and 151 MeV at an altitude of 100 km altitude. Subsequently, these CLs are used to produce a simple predictor of the polar area in which absorption events affecting aviation can occur. For simplicity, the CL behavior has been modeled based on the Kp and Dst indices separately. In case of the Kp index, Kp, a 3-hour time shifted version, Kp_{shift} has been used, since a shift in Kp index tends to predict CL behavior 3 hours in the future. The two relationships used for modeling are therefore

$$A\ Kp_{\text{shift}}^2 + B\ Kp_{\text{shift}} + C = \text{IGRF invariant latitude of cutoff (degrees)} \tag{4.2}$$

$$B\ Dst + C = \text{IGRF invariant latitude of cutoff (degrees)}, \tag{4.3}$$

in which A, B and C are empirically fitted parameters. The CLs themselves are determined in the IGRF coordinate system, thus only taking the internal magnetic field of the Earth into account.

Furthermore, since Dst and Kp_{shift} do not properly describe the poleward CL movement during arrival of an ICME and to keep the emperical relations simple, Neal et al. (2013) removed all CLs in a time period starting 15 minutes before and ending 6 hours after ICME impact on Earth. The impulse times of the ICMEs are provided by the daily published NOAA Report of Solar Geophysical Activity (RSGA) (`ftp://ftp.swpc.noaa.gov./pub/warehouse/`). Additionally, due to errors in the CL algorithm of Neal et al. (2013) which resulted in a small number of high latitude cutoffs, CLs with a geomagnetic latitude over 66° have been removed.

In the end, Neal et al. (2013) apply the regression equations 4.2 and 4.3 to their CL-database leading to the regression coefficients and R^2 values as presented in Table 11. It can be seen that the model involving Kp_{shift} has slightly higher R^2 values than the Dst based model and thus predicts the CLs better. Additionally, higher energies show further penetration into the Earth's atmosphere.

Table 11: Regression coefficients and R^2 values as presented in the paper from Neal et al. (2013) using Equation 4.2 for the Kp index and Equation 4.3 for the Dst index.

Energy at 100 km [MeV]	**Indices**	***A***	***B***	***C***	***R²***	**Number of CLs**
37.2	Kp	-0.057912	-0.38237	63.1626	0.50154	7683
76.7	Kp	-0.08087	-0.14163	61.712	0.6216	4620
151	Kp	-0.083756	-0.06691	59.8825	0.71039	4547
37.2	Dst		0.031679	62.5344	0.46114	7791
76.7	Dst		0.029931	61.3043	0.54862	4653
151	Dst		0.028514	59.5979	0.64016	4581

To compare the CL-database produced in this thesis to the results of Neal et al. (2013), the cutoff L-shell values using the IGRF internal and Tsyganenko 1989 external magnetic field models are converted into only IGRF depended cutoff L-shell values and CLs. Furthermore, all CLs exceeding a geomagnetic latitude of 66° in the IGRF coordinate system are removed. Performing linear regression based on equations 4.2 and 4.3 results in R^2_{adj} and regression coefficients shown in Table 12. It can be seen that especially for the Dst index, the correlation is much lower than reported by Neal et al. (2013). Possible explanations for lower R^2_{adj} values will be discussed in Section 5.2.

To increase the similarities with Neal et al. (2013) further, an effort has been made to apply the other selection mechanisms from the paper on the CL-database in this thesis as well. However, when only the 15 SEPEs used by Neal et al. (2013) are taken into account and the ICME impact periods have been subtracted, the obtained results for Equation 4.2 are no longer significant for all energies except one. Due to the loss of significance, these results are not presented in this thesis despite slightly higher R^2_{adj} values.

Table 12: Regression coefficients with their standard error and R^2_{adj} values obtained by applying the linear regression of equations 4.2 and 4.3 on the CL-database calculated in this thesis.

Energy [MeV]	**Indices**	***A***	***B***	***C***	R^2_{adj}	**Number of CLs**
18.18	Kp	0.021 ± 0.009	-0.49 ± 0.06	63.96 ± 0.08	0.2257	998
26.30	Kp	0.027 ± 0.007	-0.53 ± 0.05	63.91 ± 0.07	0.2327	1448
38.03	Kp	0.036 ± 0.007	-0.59 ± 0.04	63.85 ± 0.06	0.2806	1488
54.99	Kp	0.044 ± 0.007	-0.65 ± 0.05	63.82 ± 0.06	0.3856	1075
79.53	Kp	0.034 ± 0.008	-0.55 ± 0.05	63.47 ± 0.07	0.4333	619
115	Kp	0.022 ± 0.009	-0.41 ± 0.06	62.85 ± 0.08	0.3688	314
18.18	Dst		0.011 ± 0.001	63.31 ± 0.05	0.0849	998
26.30	Dst		0.0099 ± 0.0009	63.17 ± 0.04	0.0780	1448
38.03	Dst		0.0108 ± 0.0009	63.01 ± 0.04	0.0841	1488
54.99	Dst		0.015 ± 0.001	63.04 ± 0.04	0.1658	1075
79.53	Dst		0.013 ± 0.001	62.82 ± 0.04	0.1791	619
115	Dst		0.010 ± 0.001	62.35 ± 0.05	0.1695	314

To visualize the parameterization from Neal et al. (2013) versus the obtained values of this thesis, the event starting on 7 March 2012 has been used as an example. In Figures 4.13 and 4.14 the CLs determined from GPS overpasses are plotted with blue circles and the Kp_{shift} relations from Neal et al. (2013) and this thesis on top in red and yellow, respectively. For comparison, the energy values of the POES proton channels at the satellite have been used rather than at an altitude of 100 km, because the GPS energies are also measured at the satellites. Thus proton energy 24.3 MeV (POES) is compared to 26.30 MeV (Figure 4.13) and 51.5 MeV (POES) to 54.99 MeV (Figure 4.14).

It can be seen in Figures 4.13 and 4.14 that the CLs are located further poleward in these results compared to the cutoff parameterization presented by Neal et al. (2013). This effect is stronger for the 51.5 versus

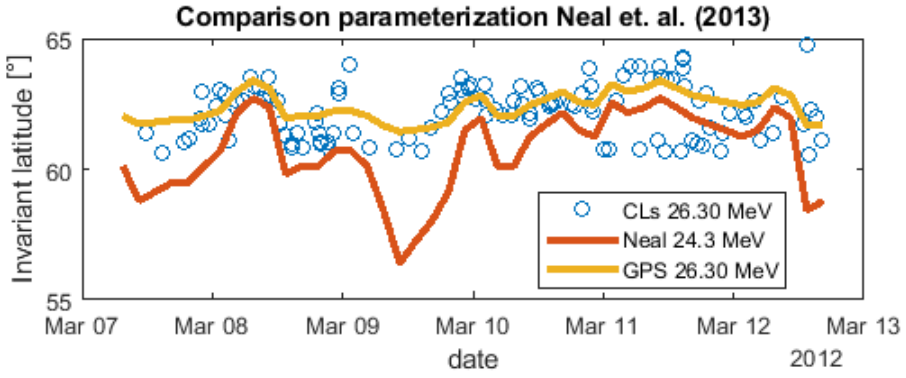

Figure 4.13: Comparison of $A\ Kp_{shift}^2 + B\ Kp_{shift} + C =$ IGRF invariant latitude of cutoff (degrees) obtained by Neal et al. (2013) (red line) and this thesis (yellow line) for energy channels 24.3 and 26.30 MeV respectively. The cutoffs from the database are plotted as blue circles.

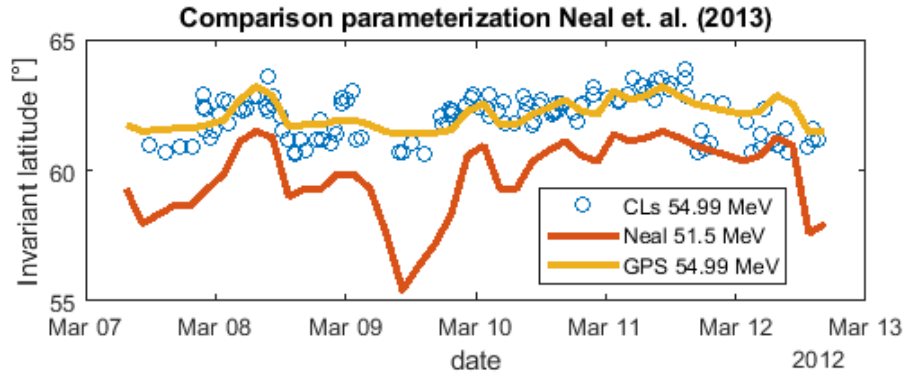

Figure 4.14: Comparison of $A\ Kp_{shift}^2 + B\ Kp_{shift} + C =$ IGRF invariant latitude of cutoff (degrees) obtained by Neal et al. (2013) (red line) and this thesis (yellow line) for energy channels 51.5 and 54.99 MeV. The cutoffs from the database are plotted as blue circles.

54.99 MeV comparison in Figure 4.14. To gain more insight in this poleward offset, a histogram plotting the difference in cutoff latitude for the 24.3 MeV (POES) (Neal et al., 2013) model versus the 26.30 MeV (GPS) fitted model for all SEPEs in this thesis is shown in Figure 4.15. Additionally, the difference in invariant latitude as function of Kp index is plotted in Figure 4.16 for the same energies. The offset seems to be quite constant for low Kp values, while it increases drastically for higher Kp values. This steep increase is probably caused by the lack of GPS data below $L = 4$. The more constant offset for lower Kp values will be discussed in more detail in Section 5.3.

Lastly, it should be noticed that the R^2_{adj} are highest for an energy of 79.53 MeV in this thesis. As explained in Section 4.3, for higher energies, the least energetic moments of SEPEs have been filtered out due to a zero differential proton flux measured by the GOES satellites. When the same moments are left out for the lower differential energies, the R^2_{adj} for Kp_{shift} increase to 0.34, 0.37, 0.40 and 0.42 for the 18.18, 26.30, 38.03 and 54.99 MeV energies respectively.

4.4.2 Comparison to Nesse Tyssøy and Stadsnes (2015)

Similar to Neal et al. (2013), Nesse Tyssøy and Stadsnes (2015) use POES satellites to empirically determine CLs. For this, only 6 SEPEs between 2003 – 2012 are taken into account which all have a maximum > 10 MeV integral flux exceeding 1000 pfu. The study focuses on the energy deposition of 1 – 32 MeV solar protons in the middle atmosphere (60 – 100 km), since protons below 20 MeV are more affected by changes in magnetic field and show stronger day-night and dawn-dusk asymmetries (Nesse Tyssøy et al., 2013; Nesse Tyssøy and Stadsnes, 2015), Nesse Tyssøy and Stadsnes (2015) investigate the day-night

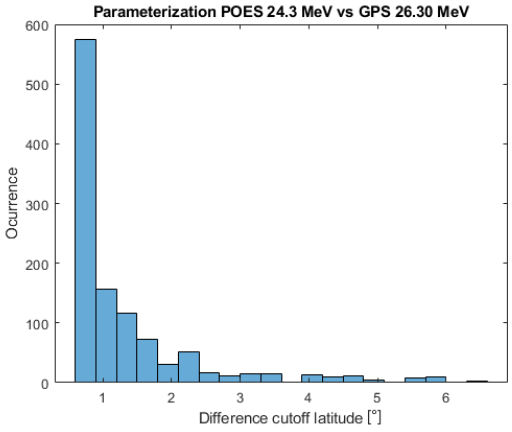

Figure 4.15: A histogram representing the difference in CL *between the* $A\ Kp_{shift}^2 + B\ Kp_{shift} + C =$ IGRF $\lambda_C[^\circ]$ *parameterization from the 24.3 MeV (*POES*) model Neal et al. (2013) and the 26.30 MeV (*GPS*) fitted model for the events between 2001 and 2015.*

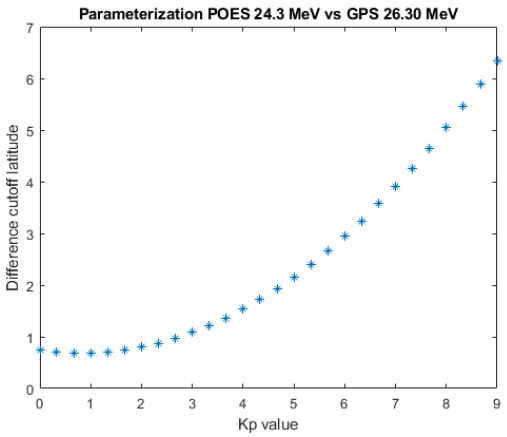

Figure 4.16: The difference in CL *between the* $A\ Kp_{shift}^2 + B\ Kp_{shift} + C =$ IGRF $\lambda_C[^\circ]$ *parameterization from the 24.3 MeV (*POES*) model Neal et al. (2013) and the 26.30 MeV (*GPS*) fitted model plotted as a function of Kp index.*

asymmetry by providing different parameterizations for both day- and nightside.

The dayside (09 – 15 MLT) cutoff variation is modeled using the regression equation

$$\lambda_C = A\ Dst + B\ B_{Z,N} + C, \tag{4.4}$$

in which λ_C represents CLs in CGM coordinates, $B_{Z,N}$ the northward orientated B_Z component of the IMF and A, B and C are regression coefficients.

For the nightside (21 – 03 MLT) cutoff modeling, the formula

$$\lambda_C = A\ Dst + B\ P_{dyn}^{1/3} + C, \tag{4.5}$$

in which $P_{dyn}^{1/3}$ represents the dynamic solar wind pressure to the power $1/3$, is used. The obtained regression models for 16 MeV protons are

$$\lambda_C = 0.070Dst + 0.14B_{Z,N} + 66.5^\circ \tag{4.6}$$

for the dayside and

$$\lambda_C = 0.035Dst - 3.0P_{dyn}^{1/3} + 67.0^\circ \tag{4.7}$$

for the nightside. The R-values are 0.73 and 0.72 respectively, leading to R^2-values just above 0.5. Additionally, for both the day- and nightside, a higher proton energy means further the penetration in the Earth's atmosphere (Nesse Tyssøy and Stadsnes, 2015).

Since the CGM coordinate system only takes the internal magnetic field into account, the cutoff L-shell values are converted to IGRF latitude system as has been done for the comparison with Neal et al. (2013). Additionally, only the 6 SEPEs used in Nesse Tyssøy and Stadsnes (2015) have been evaluated.

For the nightside, the results are shown in Table 13. The R^2_{adj} values are somewhat lower than reported by Nesse Tyssøy and Stadsnes (2015), which will be discussed in more detail in Section 5.2. When only taking into account the more energetic parts of the SEPEs as explained in Section 4.3, the R^2_{adj} values on the nightside increase to 0.57, 0.60, 0.52, 0.47 for the 18.18, 26.30, 38.03 and 54.99 MeV energies respectively. Therefore even exceeding the correlation values reported by Nesse Tyssøy and Stadsnes (2015).

Since Nesse Tyssøy and Stadsnes (2015) focus on lower energies, 16 MeV is the highest suitable energy for comparison to the parameterization obtained in this thesis. In Figure 4.17 the 16 MeV nightside

Table 13: Regression coefficients with their standard error and R^2_{adj} values obtained by applying the linear regression of Equation 4.5 on the nightside CLs from the database calculated in this thesis. NS = not significant: P-value > 0.05

Energy [MeV]	***A***	***B***	***C***	$R^2{}_{adj}$	**Number of CLs**
18.18	0.024 ± 0.006	-1.8 ± 0.4	65.9 ± 0.7	0.2754	66
26.30	0.019 ± 0.004	-1.6 ± 0.2	65.4 ± 0.4	0.4574	81
38.03	0.018 ± 0.004	-1.6 ± 0.3	65.2 ± 0.4	0.3940	91
54.99	0.013 ± 0.003	-1.6 ± 0.2	64.7 ± 0.4	0.4056	90
79.53	0.013 ± 0.004	-1.3 ± 0.3	64.2 ± 0.4	0.3319	66
115	0.006 ± 0.004	-0.5 ± 0.5	62.5 ± 0.8	0.0346 (NS)	28

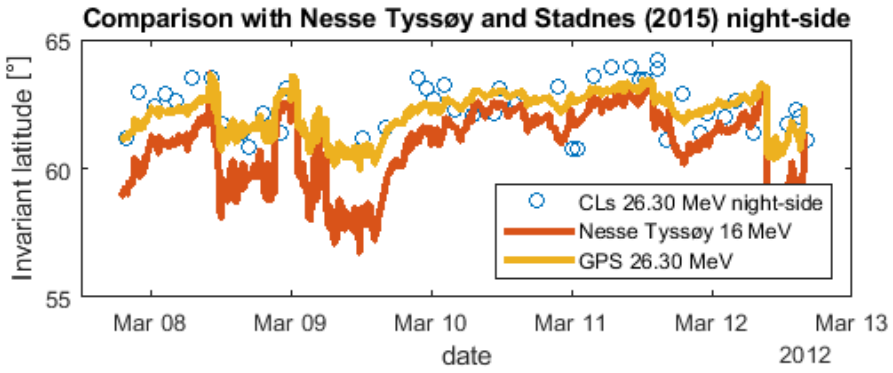

Figure 4.17: Comparison of the nightside parameterization of $\lambda_C = A\ Dst + B\ P_{dyn}^{1/3} + C$ obtained by Nesse Tyssøy and Stadsnes (2015) (red line) and this thesis (yellow line) for energy channels 16 and 26.30 MeV respectively. The nightside CLs from the database are plotted as blue circles.

parameterization of Nesse Tyssøy and Stadsnes (2015) as given by Equation 4.7 is compared to the 26.30 MeV version of this thesis. Comparable to the observations made in Subsection 4.4.1, it can be seen that the parameterization using the GPS CLs is not able to model CLs below 60° due to the inability to measure below this latitude. Furthermore, the CLs for 26.30 MeV are expected to be further equator-ward compared to the 16 MeV cutoffs. However, the opposite is observed. This poleward offset will be discussed in more detail in Section 5.3.

For the dayside, applying Equation 4.4 unfortunately does not result in significant parameterizations, because the P-values for the $B_{Z,N}$ component are > 0.2 for all energies.

5 Discussion

The results were described in Chapter 4. General trends observed in the GPS based CLs and parameterizations will be discussed in Section 5.1. Subsequently, observed caveats such as low correlation values (Section 5.2) and the offset between POES and GPS CLs (Section 5.3) will be examined. Lastly, the accuracy of the CL-database will be reviewed in Section 5.4.

5.1 General behavior of GPS based cutoff latitudes

The CL-database created from GPS energetic particle instruments manages to capture CL behavior during SEPEs. This enables CL behavior to be studied over a long time span (from 2001 onwards). In addition, from 2010, the number of GPS satellites equipped with CXD detector increased substantially resulting in higher time and spatial resolution of CLs.

The higher time resolution enables the study of CL behavior for individual SEPEs. In general, CLs show more coherence at the start and middle of a SEPE (initial and main phase in case of an accompanied geomagnetic storm) compared to the last part of a SEPE. This is for example shown in Figure 4.8. From 11 March 2012 around 18:00 onwards, CLs are more scattered. An explanation could be more coherent particle access to the magnetosphere in earlier stages of SEPEs, due to clear driving mechanisms such as a high Kp index, a low Dst index and/or an increased solar wind pressure. Near the end of an event, the proton flux decreases to levels close to 10 pfu for the > 10 MeV integral flux and the driving mechanisms show less correlation with the proton flux. In addition, some particles get trapped in radiation belts at around $L = 4$. Radiation belts could influence the GPS proton fluxes at low L shells, creating an artificially low cutoff latitude. Since the last period of a SEPE has less pronounced driving mechanisms and low differential fluxes, the flux can fluctuate more as well. Ultimately, this results in more scattered CLs. One method to exclude most of these less correlated CLs from the CL-database is to only use the more energetic moments of SEPEs, because the last part of an SEPE is usually less energetic. As shown in Subsection 4.3.2, taking only the moments into account where the GOES differential flux for 79.53 MeV is non-zero results in higher correlation values.

General trends in the CL behavior presented in this thesis include deeper penetration for higher energies. As shown in Figures 4.9 and 4.10, the energy distinction gets less clear for the most intense events, due to limitations of the GPS data source.

In addition, basic MLT asymmetries such as deepest penetration for dusk are observed. However, in previous literature (e.g. Fanselow and Stone (1972), Nesse Tyssøy et al. (2013) and Dmitriev et al. (2010)), energies below 20 MeV are used to investigate MLT asymmetries. Due to lower cross-correlation between GOES and GPS for energies below 20 MeV, it was not feasible to study MLT variations in their optimal energy range. Therefore, other satellites such as POES might be more suitable to investigate MLT dependent behavior.

5.2 Low correlation values

The R^2_{adj} values for the optimal parameterization obtained with the backward regression procedure in 4.3.2 are lower than the values obtained by using the regression equations from Neal et al. (2013) and Nesse Tyssøy and Stadsnes (2015) as described in Subsections 4.4.1 and 4.4.2. This might suggest that the optimal parameterization is not the best relation. However, this discrepancy partly originates from the coordinate system difference. To increase the resemblance when comparing to previous literature, only the internal magnetic field is taken into account in the L-shell or invariant latitude calculation. Therefore, changes in the external magnetic field as a result of geomagnetic activity are not included in the invariant latitude. This results in a seemingly stronger effect of geomagnetic conditions and thus higher R^2_{adj} values then when the L-shell calculation has already been corrected for the geomagnetic conditions as is the case for the backward regression in Section 4.3.2. Additionally, fewer CLs are taken into account when comparing to previous literature to apply the same selection criteria as used in the literature (e.g. throw out all CLs above 66° for Neal et al. (2013) and only take six strong events into account for Nesse Tyssøy and Stadsnes (2015)), resulting in a slightly better R^2_{adj}.

However, the difference in magnetic field model, cannot explain the low correlation values completely,

because the correlation is also lower when applying the same selection criteria to previous studies. An important factor could be the absence of data below $L = 4$ (60° invariant latitude). Especially during strong geomagnetic activity, such as the March 2012 event, the CL often drops below 60° as shown in Figures 4.13, 4.14 and 4.17. This results in a loss of data during maximum geomagnetic disturbance (e.g. maximum Kp index and minimum Dst index).

Additionally, the CL-database combines CLs from all sufficiently long SEPEs in the period March 2001 – 2015. Since the definition of a SEPE only considers the integral > 10 MeV flux, no distinction between the origin of the energetic protons is made. For example, SEP are accelerated close to the Sun, while ESP are accelerated closer to the Earth by shock fronts, thus having different driving mechanisms. Moreover, different event strengths and geomagnetic storm phases exhibit other characteristics. Combining all different CLs into one statistical study can lead to lower correlation values. This could also explain the very low and often insignificant correlation for the IMF components B_x, B_y and B_z.

To avoid this loss in correlation, Neal et al. (2013) removed ICME arrival periods due to poor correlation with Dst variation and no correlation with Kp change. This has not been done for the R^2_{adj} values shown in Subsection 4.4.1. This could contribute to the lower R^2_{adj} than reported by Neal et al. (2013). Additionally, it should be taken into account that the number of CLs used for the regression is almost a factor 10 lower for this study compared to the data input of Neal et al. (2013), making the CL-database of this thesis more vulnerable for deviating values and outliers.

5.3 Offset between cutoff latitudes from POES and GPS

In Subsections 4.4.1 and 4.4.2, a clear poleward offset for GPS parameterizations compared to POES parameterizations as calculated by Neal et al. (2013) and Nesse Tyssøy and Stadsnes (2015) is observed when comparing the same energy. The offset increases during strong geomagnetic activity, because the GPS satellites do not have coverage for $L < 4$. To explain the offset during lower Kp values, another explanation is needed.

A comparable offset has been observed by O'Brien et al. (2018) when comparing CLs determined from POES satellite overpasses to CLs based on data from the RPS on board of the Van Allen Probe mission. Here the discrepancy has been explained by the limited angle of incidence of the (directional) RPS instrument together with the increased precision when using the gyrocenter of protons (L_{gc}) for cutoff calculations rather than the spacecraft location (L_{sc}).

To understand the offset observed in cutoff parameterization between GPS and POES data, it is important to consider differences between the used data. Comparing the GPS to the POES spacecraft and detector it can be noted that:

- both have omnidirectional detectors: POES: four dome detectors with angle of incidence, θ, of $\pm 60°$; GPS: LEP detector ($\theta = \pm 110°$) for 6 – 50 MeV protons and HXP1 and HXP2 ($\theta = \pm 55°$) for protons > 16 MeV.
- the orientation of the detectors towards Earth is opposite: zenith (POES) versus nadir (GPS).
- POES satellites are located at an altitude of ≈ 850 km and GPS satellites at ≈ 20200 km.
- the POES energy channels are broader: $16 - 35, 35 - 70$ and $70 - 140$ MeV. For the CXD instruments only distinct differential energies are used and these should thus be narrower.
- the time resolution of POES satellites is ∼ 20 minutes for one measurement (from low to high L-shell values or the other way around) compared to ∼ 2.5 hours for GPS, resulting in much more CLs for POES data.

A part of the offset could be explained by the broader energy bands of the POES omnidirectional proton channels leading to contamination of lower energy channels by high energetic particles. To compare POES passbands to GPS differential energies, the approximate center values of the energy passbands have been used, corresponding to 24.3 MeV for the 16 – 35 MeV passband and 51.5 MeV for the 35 – 70 MeV passband. However, it would be possible for energies at the upper limit of each passband to influence the CL behavior of the entire channel. This could suggest that a passband is best represented by the upper energy limit instead of the approximate center value. This could explain the bigger offset when

comparing 51.5 (Δ18.5 MeV to upper limit passband) versus 54.99 MeV energy channels than the 24.3 (Δ10.7 MeV to upper limit passband) versus 26.30 MeV channels. To discover to which GPS differential energy the 16 – 35 MeV POES passband corresponds, the difference in cutoff latitude [°] has been plotted as a function of Kp index using the parameterizations obtained in Subsection 4.4.1. The result is shown in Figure 5.1, in which the difference in cutoff latitude [°] between the POES 24.3 MeV model versus the 26.30 (blue), 38.03 (orange), 79.53 (yellow) and 115 (purple) MeV fitted models of GPS satellites is plotted as a function of the Kp value. It can be seen that the difference in cutoff latitude decreases for higher energies. For small Kp values the difference reaches zero when comparing 24.3 MeV from POES to a differential energy between 79.53 and 115 MeV from GPS. Since an energy between 79.53 and 115 MeV is far higher than the upper limit of the POES energy channel, the broader energy bands cannot explain the offset entirely.

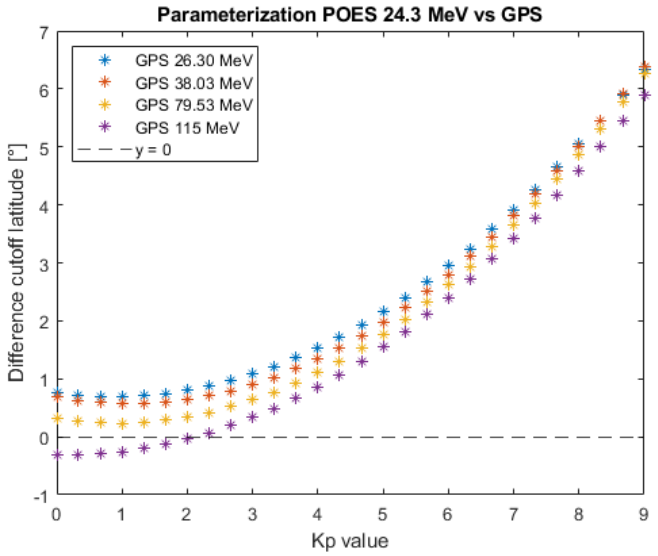

Figure 5.1: Difference in cuttof latitude between the 24.30 MeV model from POES compared to the 26.30 (blue), 38.03 (orange), 79.53 (yellow) and 115 (purple) MeV fitted models of GPS. For all cutoff calculations $A\ Kp_{shift}^2 + B\ Kp_{shift} + C =$ IGRF $\lambda_C[°]$ *is used as parameterization. The difference in degrees is plotted as a function of the* Kp *index.*

The second contribution to the offset in cutoff latitude could originate from the different satellite and detector orientation, zenith (POES) versus nadir (GPS). Rodriguez et al. (2010) explained the east-west effect for GOES satellites, where westward (eastward) looking detectors observe protons whose gyrocenter lies outside (inside) of the geostationary orbit as shown in Figure 3.2. This results in westward (eastward) looking detectors measuring protons with gyrocenters at higher (lower) L values. When this explanation is applied to the zenith - nadir orientation of POES versus GPS spacecraft, it might be the case that a zenith oriented detector observes protons whose mean gyrocenter is located at higher L values ($L_{gc} > L_s c$), while nadir looking detectors observe protons whose mean gyrocenter is located at lower L values ($L_{gc} < L_s c$). A schematic representation is shown in Figure 5.2 where the red dots represent the gyro centers of the measured protons. This implies POES CLs to be located too far equator-ward, while GPS CLs are estimated too close to the geomagnetic pole.

An important difference to the observations of GOES is the fact that GPS and POES spacecraft are moving around the Earth in inclined orbits. In the equatorial plane, where GOES is located, the L-shells have a maximum spacing of 1 R_E between them, however, closer to the geomagnetic poles, the distance between two adjacent L-shells decreases. So even though the asymmetry is less for a zenith - nadir configuration than for a east - west configuration, the difference in L_{gc} could still be significant.

The difference in altitude and orbit of the satellites could provide a third contribution to the offset. At lower altitudes, the L shells are located closer together. In addition, POES satellites move from high to low L values in $\sim$ 20 minutes compared to $\sim$ 2.5 hours for GPS satellites. Thus, the POES satellite travels faster through the different L shells enhancing the "nadir - zenith" effect mentioned above. On the other

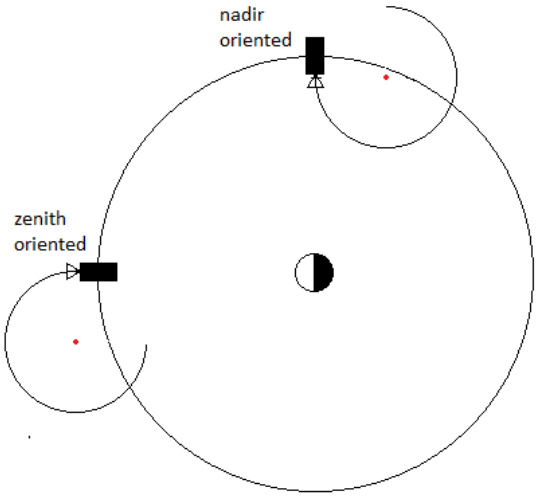

Figure 5.2: Schematic representation of the POES *(zenith) and the* GPS *(nadir) orientation seen from a top down view above the Earth. The gyrocenters are shown in red with the gyromotion of the protons around them in black. Zenith- (Nadir-)looking detectors might observe solar protons with a mean gyrocenter at higher (lower) L values.*

hand, the gyro-radii of protons are inversely proportional to the magnetic field strength (Equation 2.4), weakening the asymmetry partly.

To conclude, an offset in CL between POES and GPS parameterizations is observed when the spacecraft location, L_{sc}, is used as location for the solar energetic protons. However, for zenith oriented spacecraft such as POES, L_{gc} might be located at a larger L value than L_{sc}, while for nadir oriented spacecraft such as GPS, L_{gc} is likely to be located at smaller L value than L_{sc}. This would result in POES parameterizations estimating the CL too far equatorward, while GPS based parameterizations have a poleward shift. The real cutoff value is thus expected to be in between the POES and GPS parameterization.

5.4 Accuracy of cutoff database

In general, the behavior of the determined CLs is reliable. Comparison to results published by Chen et al. (2020) and Carver et al. (2020) indicates that the database could contribute both qualitatively and quantitatively to scientific research. The GPS satellites provide good coverage over a long period covering all MLT sectors. Furthermore, the opposite detector orientation compared to for example POES satellites results in interesting new insights.

To enable the use of this database in the future, it is important to keep possible sources of uncertainty in mind. One of these sources might be the Tsyganenko 1989 (T89) external magnetic field model used for the GPS L-shell calculation. As noted in subsection 2.2.3, the model underestimates the ring current and performs better during weak geomagnetic activity. Since SEPEs are often accompanied by strong geomagnetic activity, this might cause an extra error term in L_{sc}. For a future study it might be better to switch to a more accurate magnetic external field model during geomagnetic active times.

Another source of uncertainty might arise from the mismatch between GOES and GPS fluxes (20% for $E > 30$ MeV and 40% for $E > 10$ MeV) reported by Carver et al. (2018). This could influence the normalization of GPS fluxes which might lead to small deviations in the CLs themselves. Another source that could influence the normalization is partly shielding of the westward-looking GOES detectors during low dynamic pressure. However, it rarely happens that fluxes at $L > 7$ are shielded.

Figure 3.3 shows a "well-behaved" GPS satellite overpass in which the flux in the open-field line region is fairly constant and a steep decrease is observed towards lower (shielded) L values. This is how the cutoff determination looks for the vast majority of the CLs. However, the proton flux can be more irregular in the polar cap region despite the applied normalization as shown in Figures 5.3 and 5.4. This could lead to CLs being determined at lower cutoff latitudes (Figure 5.4) due to fluctuation flux in the cutoff

region. To avoid erroneous CLs the constraints described in Section 3.3 are applied. Nonetheless, the possibility of some erroneous CLs cannot be ruled out completely. Factors that could contribute to these erroneous cutoffs are contamination of (lower) proton channels by radiation sources such as energetic electrons and/or radiation belts or abrupt changes in proton fluxes during highly active geomagnetic moments.

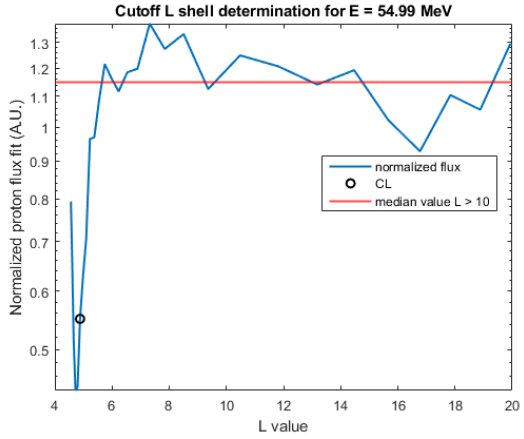

Figure 5.3: Graphical representation of CL *determination during irregularities in the polar cap. In blue the normalized proton flux for $E = 54.99$ MeV is plotted as a function of the L value. The red line gives the median proton flux in the open field line region ($L > 10$) and the black circle represents the* CL *at $L = 4.8805$. The steep increase in normalized flux towards the lowest L value could arise from a radiation belt.*

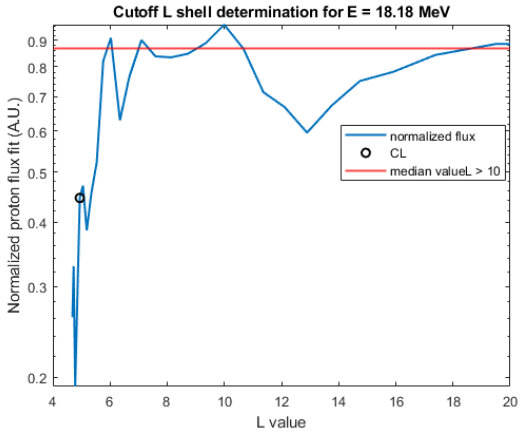

Figure 5.4: Graphical representation of CL *determination during irregularities in the polar cap. In blue the normalized proton flux for $E = 18.18$ MeV is plotted as a function of the L value. The red line gives the median proton flux in the open field line region ($L > 10$) and the black circle represents the* CL *at $L = 4.9415$.*

Lastly, a source of uncertainty is the use of the spacecraft L shell, L_{sc}, instead of the gyrocenter of the measured protons, L_{gc}. O'Brien et al. (2018) managed to decrease the spread in CLs drastically by switching to L_{gc}. The limited FOV of the RPS on board the Van Allen probe mission allowed for this conversion. It is not known whether the L_{gc} could also be determined for an omnidirectional detector such as the CXD instrument.

6 Conclusions

In this thesis, CL behavior and driving characteristics of energetic protons in the energy range 18 – 115 MeV during SEPEs have been investigated. First, a method to determine CLs from GPS energetic particle data normalized with differential GOES proton fluxes has been presented, resulting in a CL-database from 2001 – 2015. Through a statistical study, driving characteristics such as the Kp and Dst indices, dynamic pressure and IMF parameters have been studied and an optimal parameterization per energy is presented. Ultimately, a comparison between GPS versus POES based CL behavior has been performed. A summary of the key conclusions of this thesis discussed in Chapter 5 is presented here.

In summary, it has been demonstrated that GPS energetic particle data can be used to determine reliable CLs. A visual and quantitative validation has demonstrated that GOES proton channels can be used to normalize GPS proton fluxes. This extends the use of the GPS energetic particle data to solar cycle 23 as well. The good coverage over a long time period make the GPS energetic particle data an important tool to monitor and understand solar proton behavior. One important limitation of the GPS energetic particle data is the lack of data coverage for $L < 4$.

Investigation of the driving characteristics shows that a combination of Kp_{shift}, a three hour shifted version of the Kp index, Kp^2_{shift}, Dst and P_{dyn} generally gives the best CL parameterization. As expected from earlier studies, higher energies result in deeper penetration. Assessment of different MLT sectors demonstrates deepest penetration in the dusk sector. However, GPS energetic particle data does not seem to be optimal for investigating MLT asymmetries. Lastly, a very interesting offset between POES and GPS CLs caught the eye, possibly arising from a different orientation direction of the instruments.

7 Outlook

The CL determination from the GPS energetic particle data and the resultant CL-database has much more to offer than could be achieved in a single Master thesis. This thesis shows the possibilities and lays the groundwork for determination of CLs in general based on GPS energetic particle data and comparison with results from other satellite networks. Some suggestions for further work are listed below.

To increase the accuracy of the CL-database, several options could be explored. Switching from the T89 external field model to a more accurate model during geomagnetic disturbed times. An example that is already available in the GPS data files is the Tsyganenko Sitnov (TS04) model (described by Tsyganenko and Sitnov (2005)). In addition, it could be worthwhile to investigate whether it is possible to determine the gyrocenter of the measured protons, L_{gc}, for the omnidirectional detectors on board GPS satellites. If possible, this value could provide a valuable contribution to the accuracy as a replacement for the satellite location, L_{sc}. O'Brien et al. (2018) achieved much better results with L_{gc}.

In addition to the improvement of the accuracy, the CL-database could be extended. At the moment, only data concerning the northern hemisphere has been included. To expand the database and enable comparison between CL behavior in the northern and southern hemisphere, the same procedure could be followed for the southern hemisphere. Asymmetries between both hemispheres could be studied, a topic which is touched upon by Dmitriev et al. (2010) using POES data.

In this thesis, the CL behavior of the GPS CLs has been compared to characteristics of POES based models by Neal et al. (2013) and Nesse Tyssøy and Stadsnes (2015). The different goal of the satellite networks, providing a navigation network for both civilian and military applications (GPS) versus weather forecasting and monitoring (POES), results in completely different orbits and orientations. Comparing CL parameterizations between the two satellite networks could therefore become comparing apples and pears. A more suitable candidate to compare GPS CLs with, would be the Galileo satellite network. Galileo is a GNSS created by the European Union and ESA. Since the objective of Galileo and GPS are similar, both satellite networks are in MEO at comparable altitudes. Provided that the energetic particle data from Galileo would be made publicly available in the future, it would be an enormous addition to create a CL-database for Galileo as well. A qualitative comparison between both databases could be performed and, in case of a positive outcome, they could be combined to increase the coverage of both networks. Ultimately, a larger database is created which is beneficial for future statistical studies on CL behavior.

Lastly, after the above mentioned improvements and additions are applied to the CL-database, it would be worth investigating the MLT dependence in more detail to see whether asymmetries can be found. Instead of dividing the database in four MLT sectors, an elliptical fitting approach could be implemented to overcome the discontinuity at midnight. A similar approach has been followed by Dmitriev et al. (2010).

References

Adebesin, B., Ikubanni, S., Kayode, J., and Adekoya, B. (2013). Variability of solar wind dynamic pressure with solar wind parameters during intense and severe storms. *The African Review of Physics (ICTP)*, 8:119–128.

Alfvén, H. (1942). Existence of Electromagnetic-Hydrodynamic Waves. , 150(3805):405–406.

Alken, P. (2019). International geomagnetic reference field. `https://www.ngdc.noaa.gov/IAGA/vmod/igrf.html`, Accessed: 4 January 2021.

Babcock, H. W. (1961). The Topology of the Sun's Magnetic Field and the 22-YEAR Cycle. , 133:572.

Baker, K. B. and Wing, S. (1989). A new magnetic coordinate system for conjugate studies at high latitudes. *Journal of Geophysical Research: Space Physics*, 94(A7):9139–9143.

Banerjee, A., Bej, A., and Chatterjee, T. N. (2012). On the existence of a long range correlation in the geomagnetic disturbance storm time (dst) index. *Astrophysics and Space Science*, 337:23 – 32.

Bartels, J., Heck, N. H., and Johnston, H. F. (1939). The three-hour-range index measuring geomagnetic activity. *Terrestrial Magnetism and Atmospheric Electricity*, 44(4):411–454.

Baumjohann, W. and Treumann, R. A. (1996). *Basic Space Plasma Physics*. Published by Imperial College Press; Distributed by World Scientic Publishing CO.

Birch, M. J., Hargreaves, J. K., Senior, A., and Bromage, B. J. I. (2005). Variations in cutoff latitude during selected solar energetic proton events. *Journal of Geophysical Research: Space Physics*, 110(A7).

Boubrahimi, S. F., Aydin, B., Martens, P., and Angryk, R. (2017). On the prediction of >100 mev solar energetic particle events using goes satellite data. *2017 IEEE International Conference on Big Data (Big Data)*, pages 2533–2542.

Burt, J. and Smith, B. (2012). Deep space climate observatory: The dscovr mission. In *2012 IEEE Aerospace Conference*, pages 1–13.

Carver, M., Morley, S. K., and Stricklan, A. (2020). Gps constellation energetic particle measurements. In *2020 IEEE Aerospace Conference*, pages 1–10.

Carver, M. R., Sullivan, J. P., Morley, S. K., and Rodriguez, J. V. (2018). Cross calibration of the gps constellation cxd proton data with goes eps. *Space Weather*, 16(3):273–288.

Cayton, T. (2004). Monte carlo simulation of the particle channels of the combined x-ray and dosimeter (CXD). Technical Report LA-UR-04-7092, Los Alamos National Laboratory, Los Alamos. `http://permalink.lanl.gov/object/tr?what=info:lanl-repo/lareport/LA-UR-04-7092` Accessed: 5 May 2021.

Cayton, T., Chen, Y., Friedel, R., and Kippen, R. (2010). Analysis of electron and proton environment data for medium-earth orbit (2000-present). Technical Report LA-UR-10-04234, Los Alamos National Laboratory, Los Alamos. `https://permalink.lanl.gov/object/tr?what=info:lanl-repo/lareport/LA-UR-10-04234` Accessed: 29 January 2021.

Chen, Y., Morley, S. K., and Carver, M. R. (2020). Global prompt proton sensor network: Monitoring solar energetic protons based on gps satellite constellation. *Journal of Geophysical Research: Space Physics*, 125(3):e2019JA027679.

Choudhuri, A. (2011). The origin of the solar magnetic cycle. *Pramana-journal of Physics*, 77.

Chu, W. and Qin, G. (2016). The geomagnetic cutoff rigidities at high latitudes for different solar wind and geomagnetic conditions. *Annales Geophysicae*, 34(1):45–53.

Clilverd, M. A., Rodger, C. J., Moffat-Griffin, T., and Verronen, P. T. (2007). Improved dynamic geomagnetic rigidity cutoff modeling: Testing predictive accuracy. *Journal of Geophysical Research: Space Physics*, 112(A8).

Coleman, P. J., Davis, L., and Sonett, C. P. (1960). Steady component of the interplanetary magnetic field: Pioneer v. *Phys. Rev. Lett.*, 5:43–46.

Constantinescu, O. (2007). *Wave Sources and Structures in the Earth's Magnetosheath and Adjacent Regions*. PhD thesis.

Distel, J. C., Blair, S. G., Cayton, T. E., Dingler, R. D., Guyker, F., Ingraham, J. C., Noveroske, E., Reedy, R. C., Spencer, K. M., and Wehner, T. J. (1999). The combined X-ray dosimeter CXD on GPS block IIR satellites. Technical Report LA-UR-99-2280, Los Alamos National Laboratory. `https://permalink.lanl.gov/object/tr?what=info:lanl-repo/lareport/LA-UR-99-2280` Accessed: 13 December 2020.

Dmitriev, A. V., Jayachandran, P. T., and Tsai, L.-C. (2010). Elliptical model of cutoff boundaries for the solar energetic particles measured by poes satellites in december 2006. *Journal of Geophysical Research: Space Physics*, 115(A12).

Dmitriev, A. V., Suvorova, A. V., Chao, J.-K., Wang, C. B., Rastaetter, L., Panasyuk, M. I., Lazutin, L. L., Kovtyukh, A. S., Veselovsky, I. S., and Myagkova, I. N. (2014). Anomalous dynamics of the extremely compressed magnetosphere during 21 january 2005 magnetic storm. *Journal of Geophysical Research: Space Physics*, 119(2):877–896.

Fanselow, J. L. and Stone, E. C. (1972). Geomagnetic cutoffs for cosmic-ray protons for seven energy intervals between 1.2 and 39 mev. *Journal of Geophysical Research (1896-1977)*, 77(22):3999–4009.

Filwett, R. J., Jaynes, A. N., Baker, D. N., Kanekal, S. G., Kress, B., and Blake, J. B. (2020). Solar energetic proton access to the near-equatorial inner magnetosphere. *Journal of Geophysical Research: Space Physics*, 125(6):e2019JA027584. e2019JA027584 2019JA027584.

Ganushkina, N. Y., Liemohn, M. W., and Dubyagin, S. (2018). Current systems in the earth's magnetosphere. *Reviews of Geophysics*, 56(2):309–332.

Giordano, S., Ciaravella, A., Raymond, J., Ko, Y.-K., and Suleiman, R. (2013). Uvcs/soho catalog of coronal mass ejections from 1996 to 2005: Spectroscopic proprieties. *Journal of Geophysical Research: Space Physics*, 118(3):967–981.

Gjerloev, J. W. (2009). A global ground-based magnetometer initiative. *Eos, Transactions American Geophysical Union*, 90(27):230–231.

Golden, D. (2007). L shell global dipole. `https://commons.wikimedia.org/wiki/File:L_shell_global_dipole.png`, Accessed: 2 February 2021.

Gopalswamy, N., Barbieri, L., Cliver, E. W., Lu, G., Plunkett, S. P., and Skoug, R. M. (2005). Introduction to violent sun-earth connection events of october–november 2003. *Journal of Geophysical Research: Space Physics*, 110(A9).

Grabowski, B. (2016). "P
lt; 0.05" Might Not Mean What You Think: American Statistical Association Clarifies P Values. *JNCI: Journal of the National Cancer Institute*, 108(8). djw194.

Hanser, F. (2011). EPS/HEPAD calibration and data handbook. Technical Report GOESN-ENG-048, Assurance Technology Corporation, Carlisle, MA 01741. `https://ngdc.noaa.gov/stp/satellite/goes/doc/goes_nop/GOESN-ENG-048_RevD_EPS_HEPAD_13May2011.pdf` Accessed: 15 December 2020.

Hapgood, M. (2018). Chapter 1 - linking space weather science to impacts—the view from the earth. In Buzulukova, N., editor, *Extreme Events in Geospace*, pages 3 – 34. Elsevier.

Heino, E. (2019). *Spatial extent of solar proton impact in the Earth's atmosphere : observations and modeling*. PhD thesis, UiT The Arctic University of Norway, Tromsø.

Heino, E. and Partamies, N. (2020). Observational validation of cutoff models as boundaries of solar proton event impact area. *Journal of Geophysical Research: Space Physics*, 125(7):e2020JA027935. e2020JA027935 10.1029/2020JA027935.

Herlingshaw, K. (2020). *Characterising Mesoscale Fast Flow Channels in the Polar Cap Ionosphere*. PhD thesis, University of Bergen.

Jiggens, P., Chavy-Macdonald, M.-A., Santin, G., Menicucci, A., Evans, H., and Hilgers, A. (2014). The magnitude and effects of extreme solar particle events. *J. Space Weather Space Clim.*, 4:A20.

Jiggens, P., Clavie, C., Evans, H., O'Brien, T. P., Witasse, O., Mishev, A. L., Nieminen, P., Daly, E., Kalegaev, V., Vlasova, N., Borisov, S., Benck, S., Poivey, C., Cyamukungu, M., Mazur, J., Heynderickx, D., Sandberg, I., Berger, T., Usoskin, I. G., Paassilta, M., Vainio, R., Straube, U., Müller, D., Sánchez-Cano, B., Hassler, D., Praks, J., Niemelä, P., Leppinen, H., Punkkinen, A., Aminalragia-Giamini, S., and Nagatsuma, T. (2019). In situ data and effect correlation during september 2017 solar particle event. *Space Weather*, 17(1):99–117.

Kalegaev, V. V., Vlasova, N. A., Nazarkov, I. S., and Melkova, S. A. (2018). Magnetospheric access for solar protons during the january 2005 sep event. *J. Space Weather Space Clim.*, 8:A55.

Kivelson, M. and Russell, C., editors (1995). *Introduction to Space Physics*. Cambridge University Press.

Kouloumvakos, A., Nindos, A., Valtonen, E., Alissandrakis, C. E., Malandraki, O., Tsitsipis, P., Kontogeorgos, A., Moussas, X., and Hillaris, A. (2015). Properties of solar energetic particle events inferred from their associated radio emission. *A&A*, 580:A80.

Kress, B. T., Hudson, M. K., and Slocum, P. L. (2005). Impulsive solar energetic ion trapping in the magnetosphere during geomagnetic storms. *Geophysical Research Letters*, 32(6).

Kress, B. T., Mertens, C. J., and Wiltberger, M. (2010). Solar energetic particle cutoff variations during the 29–31 october 2003 geomagnetic storm. *Space Weather*, 8(5).

Lakhina, G. S., Alex, S., Mukherjee, S., and Vichare, G. (2006). On magnetic storms and substorms. In Gopalswamy, N. and Bhattacharyya, A., editors, *Proceedings of the ILWS Workshop*, page 320.

Lario, D. (2005). Advances in modeling gradual solar energetic particle events. *Advances in Space Research*, 36(12):2279–2288. Space Weather.

Laundal, K. M. and Richmond, A. D. (2017). Magnetic coordinate systems. *Space Science Reviews*, 206(1 - 4):27 – 59.

Leighton, R. B. (1969). A Magneto-Kinematic Model of the Solar Cycle. , 156:1.

Leske, R. A., Mewaldt, R. A., Stone, E. C., and von Rosenvinge, T. T. (1997). Geomagnetic Cutoff Variations During Solar Energetic Particle Events-Implications for the Space Station. In *International Cosmic Ray Conference*, volume 2 of *International Cosmic Ray Conference*, page 381.

Leske, R. A., Mewaldt, R. A., Stone, E. C., and von Rosenvinge, T. T. (2001). Observations of geomagnetic cutoff variations during solar energetic particle events and implications for the radiation environment at the space station. *Journal of Geophysical Research: Space Physics*, 106(A12):30011–30022.

Loewe, C. A. and Prölss, G. W. (1997). Classification and mean behavior of magnetic storms. *Journal of Geophysical Research: Space Physics*, 102(A7):14209–14213.

Malandraki, O. E. and Crosby, N. B. (2018). *Solar Energetic Particles and Space Weather: Science and Applications*, pages 1–26. Springer International Publishing, Cham.

McIlwain, C. E. (1961). Coordinates for mapping the distribution of magnetically trapped particles. *Journal of Geophysical Research (1896-1977)*, 66(11):3681–3691.

McIlwain, C. E. (1966). Magnetic coordinates. *Space Science Reviews*, 5(5):585–598.

Morley, S. K., Sullivan, J. P., Carver, M. R., Kippen, R. M., Friedel, R. H. W., Reeves, G. D., and Henderson, M. G. (2017). Energetic particle data from the global positioning system constellation. *Space Weather*, 15(2):283–289.

Morley, S. K., Sullivan, J. P., Henderson, M. G., Blake, J. B., and Baker, D. N. (2016). The global positioning system constellation as a space weather monitor: Comparison of electron measurements with van allen probes data. *Space Weather*, 14(2):76–92.

NASA (2008). Halloween storms of 2003 still the scariest. `https://www.nasa.gov/topics/solarsystem/features/halloween_storms.html`, Accessed: 26 January 2021.

NASA (2021). What is a solar flare. https://hesperia.gsfc.nasa.gov/sftheory/frame1.html, Accessed: 26 January 2021.

NASA, Goddard, and Kaase, A. (2017). Earth's magnetosphere. https://www.nasa.gov/mission_pages/sunearth/multimedia/magnetosphere.html, Accessed: 6 January 2021.

Neal, J. J., Rodger, C. J., and Green, J. C. (2013). Empirical determination of solar proton access to the atmosphere: Impact on polar flight paths. *Space Weather*, 11(7):420–433.

Nesse Tyssøy, H. and Stadsnes, J. (2015). Cutoff latitude variation during solar proton events: Causes and consequences. *Journal of Geophysical Research: Space Physics*, 120(1):553–563.

Nesse Tyssøy, H., Stadsnes, J., Søraas, F., and Sørbø, M. (2013). Variations in cutoff latitude during the january 2012 solar proton event and implication for the distribution of particle energy deposition. *Geophysical Research Letters*, 40(16):4149–4153.

O'Brien, B. J., Laughlin, C. D., Van Allen, J. A., and Frank, L. A. (1962). Measurements of the intensity and spectrum of electrons at 1000-kilometer altitude and high latitudes. *Journal of Geophysical Research (1896-1977)*, 67(4):1209–1225.

O'Brien, T. P., Mazur, J. E., and Looper, M. D. (2018). Solar energetic proton access to the magnetosphere during the 10–14 september 2017 particle event. *Space Weather*, 16(12):2022–2037.

Ogilvie, K. and Desch, M. (1997). The wind spacecraft and its early scientific results. *Advances in Space Research*, 20(4):559 – 568. Results of the IASTP Program.

Oh, S. Y., Yi, Y., Bieber, J. W., Evenson, P., and Kim, Y. K. (2010). Characteristics of solar proton events associated with ground level enhancements. *Journal of Geophysical Research: Space Physics*, 115(A10).

O'Hare, P., Mekhaldi, F., Adolphi, F., Raisbeck, G., Aldahan, A., Anderberg, E., Beer, J., Christl, M., Fahrni, S., Synal, H.-A., Park, J., Possnert, G., Southon, J., Bard, E., and Muscheler, R. (2019). Multiradionuclide evidence for an extreme solar proton event around 2,610 b.p. (˜660 bc). *Proceedings of the National Academy of Sciences*, 116(13):5961–5966.

Partamies, N., Juusola, L., Tanskanen, E., and Kauristie, K. (2013). Statistical properties of substorms during different storm and solar cycle phases. *Annales Geophysicae*, 31(2):349–358.

Petrosian, V. (1998). Stochastic acceleration by turbulence. *Space Science Reviews*, 173(1):535 – 556.

Plunkett, S. (2005). The extreme solar storms of october to november 2003. Technical report, Naval Research Lab Washington DC Space Science Division.

Reames, D. (2013). The two sources of solar energetic particles. *Space Science Reviews*, 175.

Richard, R. L., El-Alaoui, M., Ashour-Abdalla, M., and Walker, R. J. (2002). Interplanetary magnetic field control of the entry of solar energetic particles into the magnetosphere. *Journal of Geophysical Research: Space Physics*, 107(A8):SSH 7–1–SSH 7–20.

Richard, R. L., El-Alaoui, M., Ashour-Abdalla, M., and Walker, R. J. (2009). Modeling the entry and trapping of solar energetic particles in the magnetosphere during the november 24–25, 2001 storm. *Journal of Geophysical Research: Space Physics*, 114(A4).

Rodger, C. J., Clilverd, M. A., Verronen, P. T., Ulich, T., Jarvis, M. J., and Turunen, E. (2006). Dynamic geomagnetic rigidity cutoff variations during a solar proton event. *Journal of Geophysical Research: Space Physics*, 111(A4).

Rodriguez, J. V., Krosschell, J. C., and Green, J. C. (2014). Intercalibration of goes 8–15 solar proton detectors. *Space Weather*, 12(1):92–109.

Rodriguez, J. V., Onsager, T. G., and Mazur, J. E. (2010). The east-west effect in solar proton flux measurements in geostationary orbit: A new goes capability. *Geophysical Research Letters*, 37(7).

Sanchez, S., Fournier, A., Pinheiro, K. J., and Aubert, J. (2014). A mean-field babcock-leighton solar dynamo model with long-term variability. *Anais da Academia Brasileira de CiÃ*, 86:11 – 26.

Sandberg, I., Jiggens, P., Heynderickx, D., and Daglis, I. A. (2014). Cross calibration of noaa goes solar proton detectors using corrected nasa imp-8/gme data. *Geophysical Research Letters*, 41(13):4435–4441.

Scholer, M. (1975). Transport of energetic solar particles on closed magnetospheric field lines. *Space Science Reviews*, 17(1):3–44.

Shea, M. A. and Smart, D. F. (2001). Vertical cutoff rigidities for cosmic ray stations since 1955. In *International Cosmic Ray Conference*, volume 10 of *International Cosmic Ray Conference*, page 4063.

SILSO World Data Center (1997-2020). The international sunspot number. *International Sunspot Number Monthly Bulletin and online catalogue*.

Smart, D. (1999). Changes in Calculated Vertical Cutoff Rigidities at the Altitude of the International Space Station as a function of Geomagnetic Activity. In *26th International Cosmic Ray Conference (ICRC26), Volume 7*, volume 7 of *International Cosmic Ray Conference*, page 337.

Smart, D. and Shea, M. (2001). A comparison of the tsyganenko model predicted and measured geomagnetic cutoff latitudes. *Advances in Space Research*, 28(12):1733 – 1738.

Smart, D. and Shea, M. (2003). The space-developed dynamic vertical cutoff rigidity model and its applicability to aircraft radiation dose. *Advances in Space Research*, 32(1):103 – 108.

Smart, D. and Shea, M. (2005). A review of geomagnetic cutoff rigidities for earth-orbiting spacecraft. *Advances in Space Research*, 36:2012–2020.

Smart, D., Shea, M., and Flückiger, E. (2000). Magnetospheric models and trajectory computations. *Space Science Reviews*, 93:305–333.

Smart, D. F., Shea, M. A., and Gall, R. (1969). The daily variation of trajectory-derived high-latitude cutoff rigidities in a model magnetosphere. *Journal of Geophysical Research (1896-1977)*, 74(19):4731–4738.

Soni, P. K., Kakad, B., and Kakad, A. (2020). L-shell and energy dependence of magnetic mirror point of charged particles trapped in earth's magnetosphere. *Earth, Planets and Space*, 72(1):129.

Stone, E., Frandsen, A., Mewaldt, R., Christian, E., Margolies, D., Ormes, J., and Snow, F. (1998). The advanced composition explorer. *Space Science Reviews*, 86(1):1 – 22.

Störmer, C. (1955). *The polar aurora*. Clarendon Press, Oxford.

Tsyganenko, N. (1989). A magnetospheric magnetic field model with a warped tail current sheet. *Planetary and Space Science*, 37(1):5 – 20.

Tsyganenko, N. A. (1996). Effects of the solar wind conditions in the global magnetospheric configurations as deduced from data-based field models (Invited). In Rolfe, E. J. and Kaldeich, B., editors, *International Conference on Substorms*, volume 389 of *ESA Special Publication*, page 181.

Tsyganenko, N. A. and Sitnov, M. I. (2005). Modeling the dynamics of the inner magnetosphere during strong geomagnetic storms. *Journal of Geophysical Research: Space Physics*, 110(A3).

Tuszewski, M., Cayton, T. E., Ingraham, J. C., and Kippen, R. M. (2004). Bremsstrahlung effects in energetic particle detectors. *Space Weather*, 2(10).

Vittinghoff, E., Glidden, D. V., Shiboski, S. C., and McCulloch, C. E. (2012a). *Basic Statistical Methods*, pages 27–67. Springer US, Boston, MA.

Vittinghoff, E., Glidden, D. V., Shiboski, S. C., and McCulloch, C. E. (2012b). *Linear Regression*, pages 69–138. Springer US, Boston, MA.

Vittinghoff, E., Glidden, D. V., Shiboski, S. C., and McCulloch, C. E. (2012c). *Predictor Selection*, pages 395–429. Springer US, Boston, MA.

Zhang, Q.-H., Dunlop, M. W., Holme, R., and Woodfield, E. E. (2010). Comparison of eight years magnetic field data from cluster with tsyganenko models in the inner magnetosphere. *Annales Geophysicae*, 28.

Appendices

A File overview

The CXD data from the GPS satellites used for this thesis is available at `https://ngdc.noaa.gov/stp/space-weather/satellite-data/satellite-systems/gps/`. The data files have been processed to convert the number of counts per channel into a proton (or electron) flux. Additionally, the cross-calibration results obtained by Carver et al. (2018) has been applied to it as well. More information about the parameters in the datafiles can be found in the readme file: `https://www.ngdc.noaa.gov/stp/space-weather/satellite-data/satellite-systems/gps/readme_v1.08.pdf`.

The GOES SEPEM interpolated differential fluxes with which the GPS fluxes have been normalized can be downloaded at `http://sepem.eu/help/SEPEM_RDS_v2-01.zip`. To create the lists of SEPEs, GOES data containing the integrated fluxes have been obtained from the NOAA website (`https://www.ngdc.noaa.gov/stp/satellite/goes/`).

The Kp index is retrieved from `http://wdc.kugi.kyoto-u.ac.jp/wdc/Sec3.html`, while the other geomagnetic and solar wind parameters are downloaded from Omniweb (`https://omniweb.gsfc.nasa.gov/form/omni_min.html`).

B Specifications GOES

B.1 Design telescope and domes GOES

The EPEAD and EPS telescopes for GOES 8 – 13 are identical and a schematic representation can be seen in Figure B.1. The telescope consists of two solid state detectors (SSDs). The front one is a 50 micron, 100 mm^2 SSD and the rear one a 500 micron, 200 mm^2 SSD. The FOV is determined by collimators and extends to $\approx 35^\circ$. The detectors are surrounded by Tungsten shielding and moving magnets shield the detectors from electrons below 100 keV. Additionally aluminum foil is used to keep light out. (Hanser, 2011)

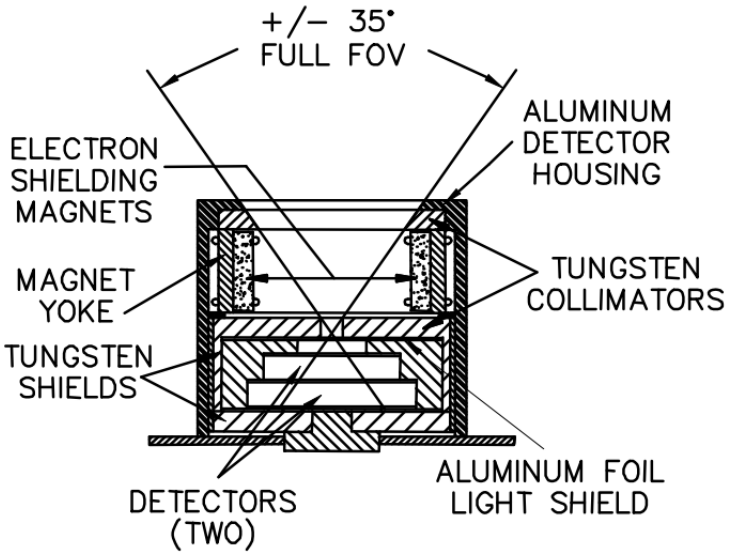

Figure B.1: Schematic representation of the EPEAD telescope configuration. Image retrieved from Hanser (2011).

The domes are shown in Figure B.2. It consists of three sets of two 1500 micron, 25 mm^2 detectors. Each set of two detectors is connected in parallel, thus acting as one single detector. The three sets each have an independent FOV defined by Tungsten collimators which also shield the detectors from particles outside

their FOV. To create the correct energy threshold for each dome, absorbers of different thickness cover the FOVs. Again, aluminum foil is applied to exclude light in the detectors. The FOVs are respectively +/- 30 °x 55°(D3) and +/- 30 °x 65°(D4 and D5). D3 is placed in the middle with its FOV focused on the EPS or EPEAD view direction. D4 and D5 are located on the sides with a FOV centered at +20°and -20°compared to D3 respectively. (Hanser, 2011)

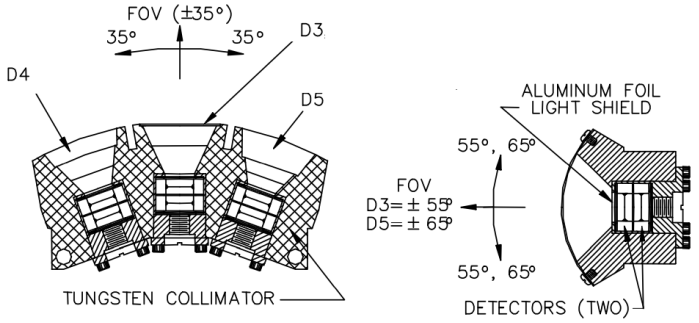

Figure B.2: Schematic representation of the EPEAD dome configuration. Image retrieved from Hanser (2011).

Dome D3 has been redesigned for GOES 8 – 12 to limit the damage from electron fluxes by reducing the aperture and the number of electron channels has been increased from one to two. Other than that, the basic detector design remains unaltered since GOES 4 (Rodriguez et al., 2014).

B.2 Energy channels GOES

In Table 14 the theoretic energy bins of the H channels are given, while in Table 15 the effective mean energies are shown. All values in both tables are given in the readme file of the SEPEM dataset (http://sepem.eu/help/SEPEM_RDS_v2-01.zip).

Table 14: The original energy channels for the H channels of the different GOES spacecrafts.

Spacecraft	**P2 [MeV]**	**P3 [MeV]**	**P4 [MeV]**	**P5 [MeV]**	**P6 [MeV]**	**P7 [MeV]**
GOES 08 – 12	4.0 – 9.0	9.0 – 15.0	15.0 – 40.0	40.0 – 80.0	80.0 – 165.0	165.0 – 500.0
GOES 13	4.2 – 8.7	8.7 – 14.5	15.0 – 40.0	38.0 – 82.0	84.0 – 200.0	110.0 – 900.0

Table 15: Effective energies of the H channels as obtained by the method of Sandberg et al. (2014). Please note there are small differences between these updates values and the values derived by Sandberg et al. (2014).

Spacecraft	**P2 [MeV]**	**P3 [MeV]**	**P4 [MeV]**	**P5 [MeV]**	**P6 [MeV]**	**P7 [MeV]**
GOES 08	6.214	10.74	18.65	47.82	105.6	152.9
GOES 11 – 13	6.643	12.61	20.55	46.62	103.7	154.6

C SEPE list

In Table 16, all SEPEs between March 2001 and December 2018 are listed. The start of a SEPE is defined when at least consecutive 12 data points, corresponding to 60 minutes, of the > 10 MeV integral GOES proton flux are at or above 10 pfu. The ending point of a SEPE occurs when at least 4 consecutive data points, corresponding to 20 minutes, are below the 10 pfu threshold.

Table 16: List of all SEPE between March 2001 and December 2018.

Event number	Start time	End time	Maximum time	Maximum flux
1	29.03.2001 16:35	31.03.2001 06:35	30.03.2001 06:10	35,4
2	02.04.2001 23:40	06.04.2001 13:00	03.04.2001 07:45	1110,0
3	10.04.2001 08:50	13.04.2001 10:00	11.04.2001 20:55	355,0
4	15.04.2001 14:10	17.04.2001 15:55	15.04.2001 19:20	951,0
5	18.04.2001 03:15	20.04.2001 07:20	18.04.2001 10:45	321,0
6	07.05.2001 19:40	08.05.2001 15:20	08.05.2001 07:55	30,0
7	15.06.2001 17:50	16.06.2001 11:25	16.06.2001 00:05	26,8
8	10.08.2001 10:20	10.08.2001 13:45	10.08.2001 11:55	17,0
9	16.08.2001 01:35	18.08.2001 05:40	16.08.2001 03:55	493,0
10	18.08.2001 07:05	18.08.2001 13:05	18.08.2001 09:10	13,8
11	24.09.2001 12:15	30.09.2001 08:20	25.09.2001 22:35	12900,0
12	01.10.2001 04:40	01.10.2001 06:00	01.10.2001 04:45	12,4
13	01.10.2001 10:45	05.10.2001 01:55	02.10.2001 08:10	2360,0
14	22.10.2001 20:10	23.10.2001 01:10	22.10.2001 21:30	24,2
15	04.11.2001 17:05	09.11.2001 15:05	06.11.2001 02:15	31700,0
16	19.11.2001 17:00	20.11.2001 10:15	20.11.2001 00:10	34,5
17	20.11.2001 10:50	20.11.2001 11:45	20.11.2001 11:30	12,0
18	22.11.2001 23:20	26.11.2001 22:15	24.11.2001 05:55	18900,0
19	26.11.2001 22:55	27.11.2001 12:10	27.11.2001 00:00	17,0
20	26.12.2001 06:05	28.12.2001 05:15	26.12.2001 11:15	780,0
21	29.12.2001 05:10	29.12.2001 21:15	29.12.2001 08:15	76,2
22	30.12.2001 03:35	30.12.2001 05:40	30.12.2001 05:10	14,4
23	30.12.2001 07:30	30.12.2001 09:25	30.12.2001 08:05	13,5
24	30.12.2001 21:20	04.01.2002 19:20	31.12.2001 16:20	108,0
25	10.01.2002 20:45	13.01.2002 13:05	11.01.2002 05:30	91,8
26	15.01.2002 15:00	15.01.2002 22:45	15.01.2002 20:00	15,4
27	16.01.2002 01:20	16.01.2002 06:35	16.01.2002 03:50	14,6
28	17.03.2002 08:20	17.03.2002 09:15	17.03.2002 08:50	13,4
29	18.03.2002 13:20	19.03.2002 20:25	19.03.2002 06:50	53,1
30	20.03.2002 16:00	20.03.2002 17:50	20.03.2002 17:25	14,3
31	22.03.2002 23:45	23.03.2002 01:00	23.03.2002 00:20	13,0
32	23.03.2002 12:55	23.03.2002 14:25	23.03.2002 13:20	16,2
33	23.03.2002 18:45	23.03.2002 20:25	23.03.2002 18:55	15,8
34	17.04.2002 15:30	17.04.2002 23:00	17.04.2002 15:40	24,1
35	21.04.2002 02:25	25.04.2002 18:30	21.04.2002 23:20	2520,0
36	25.04.2002 20:55	25.04.2002 22:00	25.04.2002 22:00	11,6
37	26.04.2002 00:25	26.04.2002 01:35	26.04.2002 01:15	12,1
38	22.05.2002 17:55	24.05.2002 13:15	23.05.2002 10:55	820,0
39	07.07.2002 18:30	08.07.2002 02:20	07.07.2002 19:55	22,6
40	16.07.2002 17:50	18.07.2002 12:40	17.07.2002 16:00	234,0
41	22.07.2002 06:55	26.07.2002 01:15	23.07.2002 10:25	28,5
42	26.07.2002 04:15	26.07.2002 06:00	26.07.2002 04:15	13,3
43	14.08.2002 12:10	14.08.2002 13:15	14.08.2002 13:10	17,0
44	14.08.2002 15:45	14.08.2002 17:10	14.08.2002 16:20	26,4
45	22.08.2002 04:40	22.08.2002 23:15	22.08.2002 09:40	36,4

Table 16: List of all SEPE *between March 2001 and December 2018.*

Event number	Start time	End time	Maximum time	Maximum flux
46	24.08.2002 01:40	26.08.2002 12:10	24.08.2002 08:35	317,0
47	07.09.2002 06:55	08.09.2002 01:40	07.09.2002 16:50	208,0
48	09.11.2002 19:20	11.11.2002 05:10	10.11.2002 05:40	404,0
49	29.05.2003 02:05	29.05.2003 03:50	29.05.2003 03:30	13,2
50	29.05.2003 04:40	30.05.2003 01:05	29.05.2003 15:30	121,0
51	31.05.2003 04:40	31.05.2003 14:15	31.05.2003 06:45	27,0
52	26.10.2003 18:25	27.10.2003 18:30	26.10.2003 22:35	466,0
53	28.10.2003 12:15	01.11.2003 04:00	29.10.2003 06:15	29500,0
54	01.11.2003 05:05	01.11.2003 06:55	01.11.2003 06:30	12,8
55	02.11.2003 11:05	04.11.2003 19:40	03.11.2003 08:15	1570,0
56	04.11.2003 22:25	07.11.2003 03:05	05.11.2003 06:00	353,0
57	22.11.2003 01:20	22.11.2003 03:00	22.11.2003 02:30	13,9
58	02.12.2003 15:05	03.12.2003 16:50	02.12.2003 18:20	88,9
59	03.12.2003 17:50	03.12.2003 19:00	03.12.2003 18:35	15,9
60	11.04.2004 11:35	12.04.2004 02:10	11.04.2004 18:45	35,5
61	25.07.2004 19:20	27.07.2004 12:50	26.07.2004 22:50	2090,0
62	13.09.2004 21:05	15.09.2004 04:30	14.09.2004 00:05	273,0
63	19.09.2004 19:25	20.09.2004 09:30	20.09.2004 01:00	57,3
64	01.11.2004 06:55	01.11.2004 17:10	01.11.2004 08:05	63,1
65	07.11.2004 19:10	13.11.2004 01:50	08.11.2004 01:15	495,0
66	13.11.2004 03:10	13.11.2004 06:15	13.11.2004 05:00	17,7
67	13.11.2004 07:45	13.11.2004 11:25	13.11.2004 09:20	16,4
68	16.01.2005 02:10	22.01.2005 16:15	17.01.2005 17:50	5040,0
69	14.05.2005 05:50	15.05.2005 06:35	15.05.2005 02:40	3140,0
70	15.05.2005 10:00	15.05.2005 11:20	15.05.2005 10:20	38,5
71	16.06.2005 22:00	17.06.2005 17:00	17.06.2005 05:00	43,8
72	14.07.2005 14:00	16.07.2005 22:00	15.07.2005 03:45	134,0
73	17.07.2005 17:35	17.07.2005 18:40	17.07.2005 17:55	16,0
74	17.07.2005 20:40	18.07.2005 07:10	17.07.2005 22:40	22,1
75	27.07.2005 23:00	01.08.2005 09:45	29.07.2005 17:15	41,1
76	22.08.2005 20:40	25.08.2005 00:15	23.08.2005 10:45	337,0
77	08.09.2005 02:25	12.09.2005 21:30	11.09.2005 04:25	1880,0
78	14.09.2005 00:40	16.09.2005 00:25	15.09.2005 09:05	235,0
79	06.12.2006 16:15	12.12.2006 10:35	07.12.2006 18:40	1980,0
80	13.12.2006 03:10	14.12.2006 21:20	13.12.2006 09:25	698,0
81	14.12.2006 22:55	15.12.2006 15:10	15.12.2006 00:15	215,0
82	14.08.2010 12:35	14.08.2010 13:00	14.08.2010 12:45	14,9
83	08.03.2011 01:05	10.03.2011 01:00	08.03.2011 08:00	50,4
84	10.03.2011 06:50	10.03.2011 11:05	10.03.2011 07:15	17,7
85	22.03.2011 00:45	22.03.2011 02:20	22.03.2011 01:35	14,5
86	07.06.2011 08:20	08.06.2011 15:55	07.06.2011 18:20	72,9
87	04.08.2011 06:35	06.08.2011 04:25	05.08.2011 21:50	96,4
88	09.08.2011 08:45	09.08.2011 17:10	09.08.2011 12:10	26,9
89	24.09.2011 02:40	24.09.2011 12:55	24.09.2011 10:50	13,2
90	24.09.2011 18:35	26.09.2011 20:50	26.09.2011 11:15	35,7
91	26.09.2011 22:00	27.09.2011 01:05	27.09.2011 00:40	13,6
92	23.10.2011 15:00	23.10.2011 16:00	23.10.2011 15:35	13,2
93	26.11.2011 11:25	28.11.2011 00:25	27.11.2011 01:25	80,3
94	23.01.2012 05:30	27.01.2012 08:50	24.01.2012 15:30	6314,1
95	27.01.2012 19:05	31.01.2012 05:20	28.01.2012 02:05	795,6
96	07.03.2012 05:10	12.03.2012 19:10	08.03.2012 11:15	6529,8

Table 16: List of all SEPE *between March 2001 and December 2018.*

Event number	Start time	End time	Maximum time	Maximum flux
97	13.03.2012 18:10	15.03.2012 06:15	13.03.2012 20:45	468,8
98	17.05.2012 02:10	18.05.2012 13:40	17.05.2012 04:30	255,4
99	27.05.2012 09:45	27.05.2012 11:35	27.05.2012 10:45	14,8
100	16.06.2012 19:55	16.06.2012 21:20	16.06.2012 20:20	14,4
101	07.07.2012 04:00	07.07.2012 17:45	07.07.2012 07:45	25,2
102	09.07.2012 01:30	09.07.2012 14:40	09.07.2012 04:30	19,2
103	12.07.2012 18:35	14.07.2012 22:45	12.07.2012 22:25	96,1
104	15.07.2012 00:25	15.07.2012 01:55	15.07.2012 01:05	13,2
105	17.07.2012 17:15	21.07.2012 00:00	18.07.2012 06:00	135,9
106	23.07.2012 18:40	23.07.2012 19:35	23.07.2012 19:00	11,7
107	23.07.2012 20:55	23.07.2012 22:35	23.07.2012 21:45	12,8
108	01.09.2012 13:35	01.09.2012 23:45	01.09.2012 22:10	44,3
109	02.09.2012 01:50	02.09.2012 05:45	02.09.2012 02:35	47,4
110	02.09.2012 06:35	03.09.2012 06:10	02.09.2012 08:50	59,9
111	03.09.2012 07:55	03.09.2012 08:50	03.09.2012 07:55	11,9
112	03.09.2012 09:20	03.09.2012 10:40	03.09.2012 10:05	14,7
113	03.09.2012 11:05	03.09.2012 14:20	03.09.2012 13:45	14,2
114	28.09.2012 03:00	28.09.2012 10:00	28.09.2012 04:45	28,4
115	16.03.2013 20:45	17.03.2013 02:05	16.03.2013 21:40	14,9
116	11.04.2013 10:55	12.04.2013 18:45	11.04.2013 16:45	113,6
117	15.05.2013 14:20	18.05.2013 12:25	17.05.2013 17:20	41,7
118	24.06.2013 00:30	24.06.2013 08:45	24.06.2013 05:20	14,1
119	30.09.2013 05:05	02.10.2013 04:45	30.09.2013 20:05	181,8
120	28.12.2013 21:50	29.12.2013 06:40	28.12.2013 23:15	29,3
121	06.01.2014 09:15	11.01.2014 16:25	09.01.2014 03:40	1026,1
122	20.02.2014 08:50	20.02.2014 10:10	20.02.2014 09:25	22,3
123	25.02.2014 14:50	02.03.2014 22:25	28.02.2014 08:45	102,6
124	18.04.2014 15:25	20.04.2014 11:50	19.04.2014 01:05	58,5
125	11.09.2014 02:55	12.09.2014 22:35	12.09.2014 15:55	126,1
126	18.06.2015 11:35	18.06.2015 22:20	18.06.2015 14:45	16,8
127	21.06.2015 20:35	24.06.2015 04:45	22.06.2015 19:00	1066,3
128	26.06.2015 05:35	26.06.2015 07:20	26.06.2015 05:55	12,2
129	26.06.2015 07:45	27.06.2015 03:45	27.06.2015 00:30	22,4
130	29.10.2015 05:50	29.10.2015 13:25	29.10.2015 10:00	23,5

D Statistical terminology

Here you can find a brief explanation of the statistical terminology relevant for this thesis. For more information, Vittinghoff et al. (2012a,b,c) can be consulted.

- r: the correlation coefficient, is a measure of the correlation between variables. In case of a linear model, it thus gives the linear correlation between two variables.
- R^2: the coefficient of determination, which can be interpret as the proportion of the total variability of the outcome that is accounted for in the model (Vittinghoff et al., 2012a). $R^2 = 1$ thus means that the model accounts for all variability of the outcome. It can be calculated as the square of the correlation coefficient, $R^2 = r^2$.
- Adjusted R^2, R^2_{adj}: penalizes the R^2 coefficient for adding extra predictors into the model. Therefore, R^2_{adj} only increases when the increment in R^2 is larger than the increment in the penalty (Vittinghoff et al., 2012c).

- The null hypothesis, H_0: hypothesis that two samples have the same distribution. Thus, including one extra independent variable does not change the distribution and the extra variable is therefore not statistically significant if the null hypothesis is true. Therefore, the null hypothesis should be rejected in order for a variable to be significant.
- P-value: gives the probability of obtaining test results at least as extreme as the input dataset assuming that the the null hypothesis is correct. Thus a large P-value means that such an extreme outcome would be very likely and thus the result is significant irrelevant, because the null hypothesis cannot be rejected. A high P-value thus means that it is very likely that the studied groups are the same. On the other hand, a very low P-value means that it would be almost impossible to reproduce the same result and hence the null hypothesis can be rejected and the result shows significance.
- α: level of significance; When $P < \alpha$, the null hypothesis is rejected and a result is thus seen as statistically significant. Often a threshold of $\alpha = 0.05$ or 5% is used in literature (Vittinghoff et al., 2012a; Nesse Tyssøy and Stadsnes, 2015). However, note that the P-value is more complicated and that the level of significance might be more fluid (Grabowski, 2016).
- Multiple Linear Regression (MLR): MLR is a statistical technique in which multiple independent variables are used to predict a dependent variable using linear relations between the individual independent variables and the dependent variable. The given outcome y given an independent variable x represented by $E[y|\boldsymbol{x}]$ can be determined using the expression:

$$E[y|\boldsymbol{x}] = \beta_0 + \beta_1 x_1 + \beta_2 x_2 + ... + \beta_p x_p, \tag{D.1}$$

  in which $\boldsymbol{x}$ represent the collection of p independent variables, $x_1, x_2, ..., x_p$ and $\beta_1, \beta_2, ..., \beta_p$ are the regression coefficients. In case only one independent variable is used, the model is simplified to $E[y|x] = \beta_0 + \beta_1 x$ (Vittinghoff et al., 2012b).

  To model individual observations, y_i, equation D.1 becomes

$$y_i = E[y|\boldsymbol{x_i}] = \beta_0 + \beta_1 x_{1i} + \beta_2 x_{2i} + ... + \beta_p x_{pi} + \epsilon_i \tag{D.2}$$

  in which x_{ji} represents the value of independent variables x_j for observation i and ϵ_i represents the error term (or residual) for observation i, assuming ϵ is normally distributed with mean zero, every value of $\boldsymbol{x}$ has the same standard deviation σ_ϵ and its values are statistically independent (Vittinghoff et al., 2012b).

  In order to introduce non-linear relations, the desired power of the independent variable is applied and the outcome is used as a new independent variable x_{ji}.